INTEGRATED LINEAR DIFFRACTION GRATING SPECTROMETER

BY

HEATHER JOANNE HNATIUK

A Thesis
Submitted to the Faculty of Graduate Studies
In Partial Fulfillment of the Requirements
for the Degree of

DOCTOR OF PHILOSOPHY

Department of Physics and Astronomy
University of Manitoba
Winnipeg, Manitoba

THE UNIVERSITY OF MANITOBA

FACULTY OF GRADUATE STUDIES

*****

COPYRIGHT PERMISSION PAGE

Integrated Linear Diffraction Grating Spectrometer

BY

Heather Joanne Hnatiuk

A Thesis/Practicum submitted to the Faculty of Graduate Studies of The University of Manitoba in partial fulfillment of the requirements of the degree of Doctor of Philosophy

ABSTRACT

The ever-increasing required capacity of telecommunications networks is driving research into new technology that can increase the network capacity with the lowest possible cost. One of the newest and most promising technologies is wavelength division multiplexing (WDM). This technology uses the concept of simultaneously transmitting many signals at different wavelengths down a single optical fiber. Optical signal transmission at four wavelengths, for example, quadruples the capacity of the current fiber infrastructure. The system, however, cannot be realized without a device that separates the signals at the receiver; i.e. a demultiplexer.

Demultiplexers may use many different technologies (interference filter, or bulk grating for example). This thesis focuses on an integrated diffraction grating design. In this type of device, diffraction gratings are etched into slab waveguide layers. The incident light is guided through the slab and is reflected and diffracted by the grating. The diffraction process spatially separates the channels that were transmitted at different wavelengths.

The goal of this thesis is to design, characterize and numerically model a novel integrated diffraction grating spectrometer. This design is to be used as a comparison to the performance of similar grating spectrometers using a different grating configuration. The guidelines used for design parameters of the spectrometer are defined by the concerns of the telecommunications industry. The device should have low insertion loss, low

polarization dependent performance, high channel isolation, and use industry-defined channel spacings (and channel wavelengths).

The designed integrated grating spectrometer uses a linear grating, to improve grating facet uniformity. The grating facets were designed to achieve large dispersion with a small device size. A concave mirror was used to collimate and focus the light. The spectrometer was fabricated and tested. It showed good channel spacing uniformity and output intensity profile shape. The insertion loss and polarization dependent performance were not sufficient for a practical telecommunications product however these problems may be solved with slightly different fabrication techniques.

Simulations of the behaviour of the grating facets were done using finite-difference time-domain (FDTD) techniques. These results showed that the facet shape efficiently retro-reflected the incident light.

ACKNOWLEDGEMENTS

I would like to thank my advisor Dr. Ken McGreer for his contribution to this work. His dedication and expertise were invaluable assets.

Fabrication of the spectrometers was done at Alberta Microelectronic Corporation (AMC) in Edmonton, AB with the help of Dr. Jim Broughton. Jim worked closely with our research group in developing new etching techniques to ensure vertical sidewalls as well as producing low loss SiON slabs.

All research was conducted at TR*Labs* (Telecommunications Research Laboratories) and its generous funding in support of this research must be recognized. I would like to express my sincere gratitude to the "family" at TR*Labs* for the positive reinforcement I received on a daily basis. Further funding for this endeavour was provided by the National Sciences and Engineering Research Council (NSERC) and was greatly appreciated.

To my fellow graduate students, Dan Jackson, Michael Smith and Dr. Zhijian Sun, thank you for donating your time and thought in many discussions. A special thanks goes to Dan for putting up with my endless chatter and for all your help in the lab (particularly with the automation software).

To my parents, thank you for your encouragement from day one to follow my love of science and learning. Thank you for being there every time I needed a boost.

TABLE OF CONTENTS

CHAPTER ONE

CHAPTER TWO

CHAPTER THREE

CHAPTER SEVEN

LIST OF FIGURES

LIST OF TABLES

CHAPTER ONE

INTRODUCTION

1.1 TELECOMMUNICATIONS NETWORKS

In the last 20 years the telecommunications industry has exploded from being a voice-only copper wire network to a complex web of switches, lasers and optical fiber spanning the globe. The majority of phone calls that an average Canadian makes travels over this fiber optic network faster and clearer than anything that could have been achieved with copper wire technology or satellite connections. Although both of these technologies are still in use throughout the world, high traffic links are most certainly connected with fiber.

The advent of the World Wide Web and the Internet has drastically increased the demand for bandwidth on the networks. Voice and data streams both compete for space on the limited bandwidth of the fiber links. The number of users on the fiber links increases with every day, and the capacity demanded per user is increasing with users transferring more volume than ever before. The data streams consist of video, sound, pictures, and text. Network capacity is being stretched to its limits even more with the growth in interest of real time video conferencing, remote telemedicine (physicians sharing expertise through real time video exchange) and Internet telephony. The demands of the consumer must be met and therefore telecommunications companies are looking for ways to increase their capacity in the most inexpensive way possible.

The first and most obvious solution to the bandwidth shortage is to lay more optical fiber between high traffic centers. The additional fiber gives another pipe on which the data may be transferred. However, burying new fiber is a very costly undertaking that comes with land ownership problems, and all the problems associated with laying new infrastructure. In addition to these problems, the maintenance of another fiber line is labour intensive. With these difficulties in mind, telecommunications companies would much rather find an alternative to laying new fiber links for increasing fiber capacity.

A new technology that has emerged in the last three to four years is Wavelength Division Multiplexing (WDM). This technology eliminates the need to lay new fiber and can increase the capacity of an existing fiber link by factors of 4, 8, 16, 32, or higher. The benefits of not having to lay new fiber are obvious but it has further benefits in that the system can be upgraded reasonably easily from a 4 channel WDM to a 16 channel WDM,

quadrupling the capacity. Clearly telecommunications providers are looking seriously at this technology and several have already implemented the technology in the United States between high traffic links. It has become an accepted technology even though it is still somewhat immature.

1.2 WAVELENGTH DIVISION MULTIPLEXING

Wavelength division multiplexing (WDM) refers to sending multiple signals down a single optical fiber. Every data signal is transmitted using a unique modulated carrier wavelength. The signals are multiplexed at the switch and transmitted simultaneously down the fiber link to the next switch where the signals are demultiplexed and rerouted to their destinations. WDM is used at several different levels ranging from the broadband applications, using laser wavelengths at 980 nm, 1310 nm and 1550 nm, to the dense WDM (DWDM) applications where wavelengths are spaced at 0.8 nm (100 GHz) in a narrow band centered around 1550 nm. The standard for WDM channels set by the ITU (International Telecommunications Union) gives two bands over which WDM signals are to be sent. The blue band consists of frequencies between 194.1 - 196.5 THz (1545.60 nm - 1526.72 nm) and the red band consists of channels in the 191.6 - 194.0 THz (1565.76 nm -1546.39 nm) range. The current standard requires the carrier wavelengths to be separated by 100 GHz, 200 GHz or 400 GHz; however, commercial products are already being developed for systems using 50 GHz (0.4 nm) channel spacing.

There are three key elements to the WDM system; the transmitting lasers, the amplifiers along the length of the long haul fibers and the multi/demultiplexers at the transmitters and receivers.

1.2.1 TRANSMITTING LASERS

The transmitting lasers must be highly stable lasers, capable of producing laser light at a specified wavelength with a narrow wavelength spectrum. In systems where DWDM is used, the stability of the lasers is a serious concern and DWDM is pushing the development of more stable lasers with narrow wavelength distributions. Semiconductor laser diodes are generally the sources used in telecommunications applications. The biggest consideration in laser usage is how the laser is modulated. The laser may be directly modulated to contain the transmitted signal or the produced beam may be externally modulated using electro-optic methods (Mach-Zehnder modulators for example). Many ideas have been considered for creating the most stable linewidths. Lasers have been fitted with all types of wavelength filters (like fiber Bragg gratings) to produce well-defined transmitted center wavelengths. In general, the laser center wavelength must be stable such that the fluctuations are at least an order of magnitude smaller than the passband of a typical WDM channel (at 100 GHz).

The distributed feedback (DFB) laser is most commonly used in telecommunications systems but distributed Bragg-reflector (DBR) lasers are also used [1]. These lasers are capable of several milliWatts of power with linewidths as small as 5 MHz and current modulation at 20 GHz. These specifications are sufficient for

telecommunications purposes, however new technologies are being developed continuously.

1.2.2 OPTICAL FIBER

In WDM systems the type of fiber seriously limits the total amount of data that may be transmitted, the rate at which it is transmitted as well as how often the signal has to be regenerated due to losses in the fiber. There are two main types of fiber currently in use in (long haul) telecommunications networks: dispersion shifted and non-dispersion shifted single mode fiber. Silica fiber has a zero dispersion point for light at 1310 nm. The zero in the dispersion curve can be moved to 1550 nm by adjusting the index profile of the fiber. The fiber has minimum attenuation at 1550 nm; therefore zero dispersion and minimum attenuation seem attractive. Dispersion shifted fiber is more expensive to make than non-shifted fiber; therefore there is more of the non-shifted fiber currently in use. In certain situations the dispersion-shifted fiber is more crucial, as in spans of fiber where repeaters are further apart. In WDM systems, non-zero dispersion-shifted fiber is the fiber of choice [2]. In this type of fiber, the zero dispersion point is moved outside the WDM wavelength band to minimize the impact of non-linear effects in the fiber. At zero dispersion the non-linear effects in the fiber are most efficient.

1.2.3 ERBIUM DOPED FIBER AMPLIFIERS

The amplifiers in a WDM system must give uniform gain across the used WDM band, have low noise production and compensate for nonlinearities in the fiber loss across the

WDM band. The amplifiers used in WDM systems are erbium doped fiber amplifiers (EDFA). These amplifiers can accomplish all of the goals required in the WDM system by using their inherent qualities and improving their performance with gain flatteners.

An EDFA is created by doping a section of silica or fluoride fiber with erbium atoms. The doped medium is pumped with a wavelength that excites the Er^{3+} atoms which then in turn produce spontaneous and stimulated emission, as in the performance of lasers. The stimulated emission effectively creates a gain in the medium for carrier

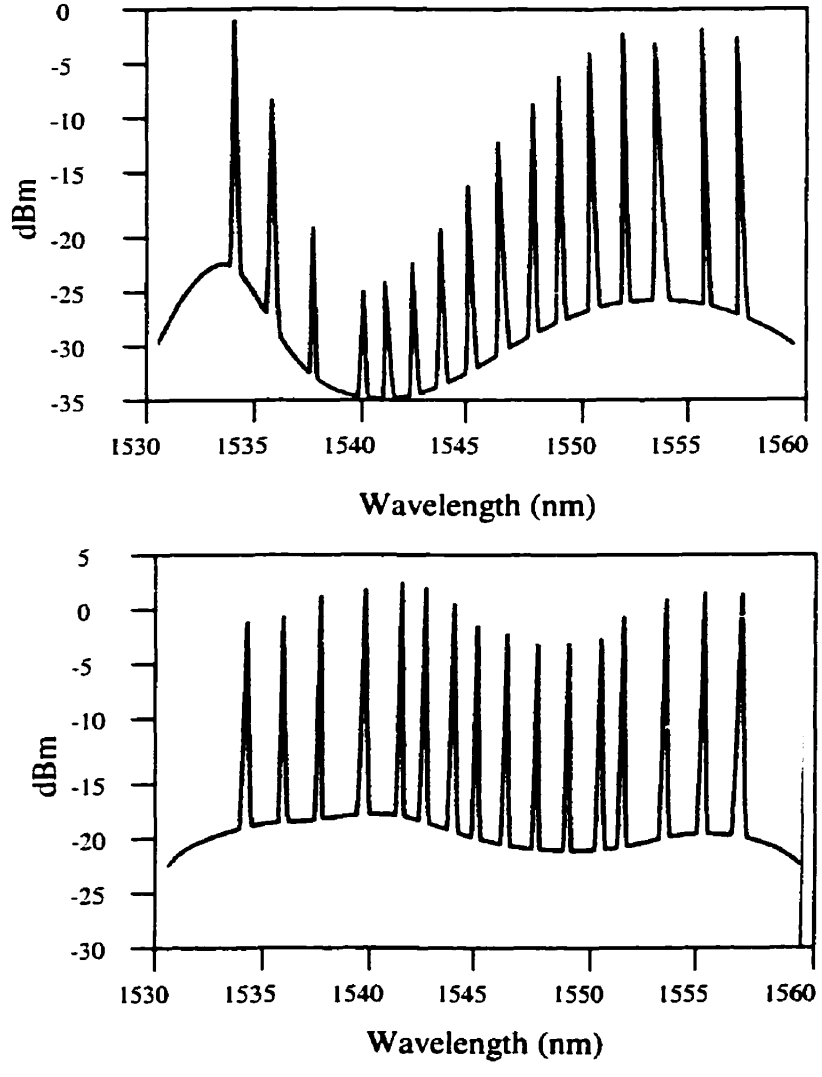

Figure 1.1 The gain profiles of silica (top) and fluoride (bottom) fiber amplifiers. Notice that the fluoride fiber profile is much flatter.

wavelengths. The gain is not however uniform over all wavelengths within its gain region of 1530 nm to 1560 nm. In particular the gain profile of a silica amplifier has a significant drop in the region of 1540 nm. This is a problem for WDM systems because non-uniform gain will be added systematically as the channel propagates through the system, the channels near 1540 nm will eventually have a signal-to-noise ratio that does not allow for reliable signal detection. The gain profile can be flattened using attenuators on the higher gain channels to reduce the power level to the lowest channel level. Adjusting the power level of one channel may affect the power level in other channels therefore the power leveling technique must be done in an iterative manner and this slows down the system. The power leveling technique may be a problem as networks move into the newest high speed technologies with data rates of 10 Gbits/sec (OC-192).

The doped fluoride fiber is a good alternative to the silica because it has a much flatter gain profile, as shown in Figure 1.1 with only a 1.5 dB variation over its 1532 - 1560 nm amplification window [3]. Some power leveling must be done over the WDM window but the adjustment is considerably smaller. In spite of its flat gain profile, fluoride fiber amplifiers have fundamental performance difficulties. The noise level due to amplified spontaneous emission is higher in fluoride fiber than in silica fiber (1 dB higher than silica at 5 dB). The main reason for the higher noise figure due to the fluoride fiber is the use of a pump of 1480 nm laser light, as opposed to the 980 nm light used in the silica fiber.

One solution to the dichotomy of the two fiber types is to use both amplifiers in a cascade [4]. The silica fiber is the first stage because it is low noise and therefore the

spontaneous emission light will not have such a great effect at the second, flat gain profile stage of the fluoride fiber.

Much research is being done to create an EDFA that complies with all the stringent requirements applied by WDM networks. The EDFA allows the WDM system (or a single wavelength system) to be more cost-effective by eliminating the need for frequent retransmission along the fiber line. In the case of WDM systems this is even more important, as electrical regeneration requires signal demultiplexing, electrical detection and amplification, and subsequent signal retransmission. These are time-consuming activities and should be eliminated as often as possible for fast, reliable network operation. In WDM systems however, the fiber may cause a great deal of loss at high data rates (due to material dispersion) and repeaters may be needed every 50 km. The use of electrical amplification at 50 km intervals quickly becomes expensive and difficult to maintain. An EDFA amplifies the signal passively at all wavelengths without the need to demultiplex the signals at each amplification stage. The introduction of EDFA's has furthered the advance of telecommunications greatly.

1.2.4 MULTI/DEMULTIPLEXERS

The multi/demultiplexers can be constructed using a great deal of technologies. Regardless of technology, the multi/demultiplexers must produce good adjacent channel isolation (low cross talk between channels), have flat output power response in each channel passband, and have uniform loss at the center of each passband. These criteria

are not easily met simultaneously and many permutations of WDM devices have appeared in the last 5 years.

1.3 WDM DEMULTIPLEXER TECHNOLOGIES

As an overview of the existing technologies, this section will briefly give descriptions of the principles involved in each technology and the advantages and disadvantages related to each. A short but relevant overview of these technologies may be found in Turley [5].

1.3.1 INTERFERENCE FILTERS

Interference filters are very common in the commercial WDM marketplace. This technology is a totally passive component that relies on interference at layer boundaries to either transmit or reflect the light. Each WDM channel is transmitted at the one interface

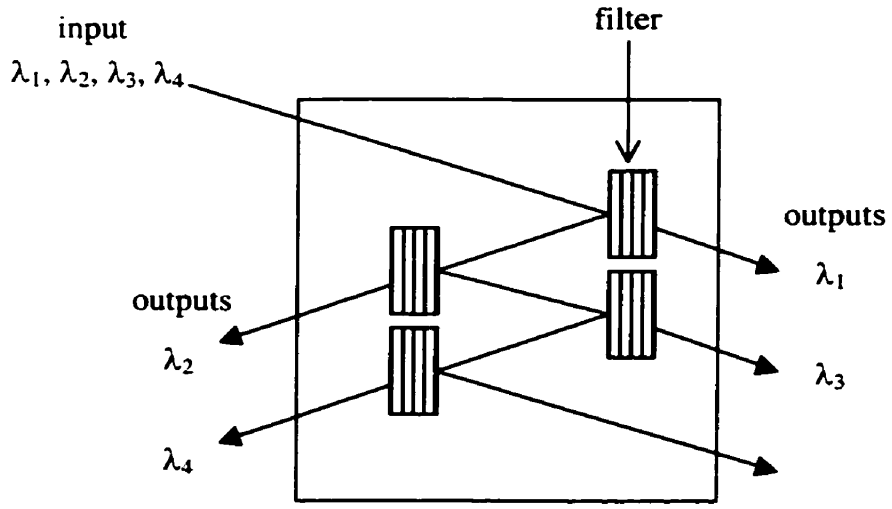

Figure 1.2 In an interference filter, multiple wavelengths enter the device and are sequentially split off at filters designed to pass only one WDM channel.

(of the many interfaces encountered within the filter) that satisfies its interference criteria. Interference filters provide high channel isolation (-25 dB), low polarization dependence low insertion loss (7 dB) and little or no temperature-dependent performance. These filters meet the objectives of WDM demultiplexers for low channel-count cases. Many of these filters may be cascaded to achieve a channel count of up to 40; however for channel counts higher than 40, the loss per channel becomes highly channel dependent. For every reflection that a channel must traverse, a loss is sustained; therefore, each channel will have different throughput loss. Interference technology is superior for low channel count systems but it is inferior in high channel count DWDM systems.

1.3.2 BULK OPTICS

The bulk optics category of demultiplexers consists of two types of devices. The first is a grating-based device where a bulk diffraction grating is used to separate the channels. This type of device is easy to manufacture because bulk grating technology is well understood. These devices achieve low insertion loss (< 6 dB), low polarization dependent loss (0.2 dB) and high resolution. The large physical size of the bulk grating demultiplexers is a detriment to the implementation of the technology. The second type of bulk optics demultiplexer uses a graded index lens to separate the wavelengths. There are a couple of problems with these types of demultiplexers. Manufacturing the demultiplexer can be difficult because the optical components must be aligned to tight tolerances. Tight tolerances cause the assembly of the bulk grating demultiplexer units to

be labour intensive as well as more unreliable than other technologies. In the case of the graded index lens components, the number of WDM channels that may be separated is limited.

1.3.3 ARRAYED WAVEGUIDES

Arrayed waveguide devices are often fabricated in silica layers on a silicon wafer [6] however other materials have also been used [7]. They consist of many ridge waveguides etched into these layers. Each of the ridge waveguides has a different path length, causing interference at the end of the ridge waveguides where the waveguide becomes only a slab waveguide. Channels are separated through this interference and collected with output waveguides. The advantages of the arrayed waveguide demultiplexer are that many of these devices may be fabricated from one pattern using standard photolithography techniques and they are very compact and rugged (compared to bulk optics devices). However, these demultiplexers tend to be polarization dependent, thermally sensitive and have poorer passbands than interference filter demultiplexers.

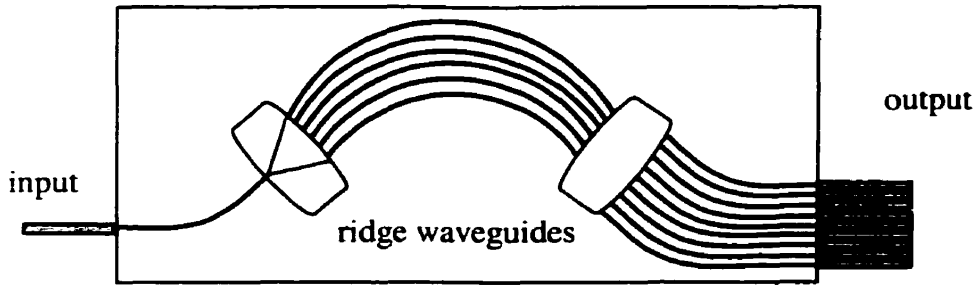

Figure 1.3 The arrayed waveguide demultiplexer. Multiple wavelengths are injected into the device on the left. The signal is split so that parts travel through all of the waveguides in the center of the device. A difference in path length creates interference and splits up the WDM channels.

These problems may be remedied by using special layer construction to reduce polarization dependence, thermal isolation units (to maintain constant temperatures) and fiber Bragg filters at the output can be used to sharpen the passband.

1.3.4 INTEGRATED WAVEGUIDE GRATING DEVICES

Integrated waveguide grating demultiplexers have many of the same characteristics as the arrayed waveguide devices. The device is etched into waveguide layers, often silica layers deposited on a silicon wafer (though InGaAsP/InP is popular as well). The main components of these devices are the diffraction grating and the output waveguides. Integrated grating demultiplexers often use input waveguides to launch the light into the slab waveguide where the light is guided toward a diffraction grating. The light is reflected (and diffracted) by the grating and the channels are reflected toward separate output waveguides. Usually each channel is collected by a different output waveguide;

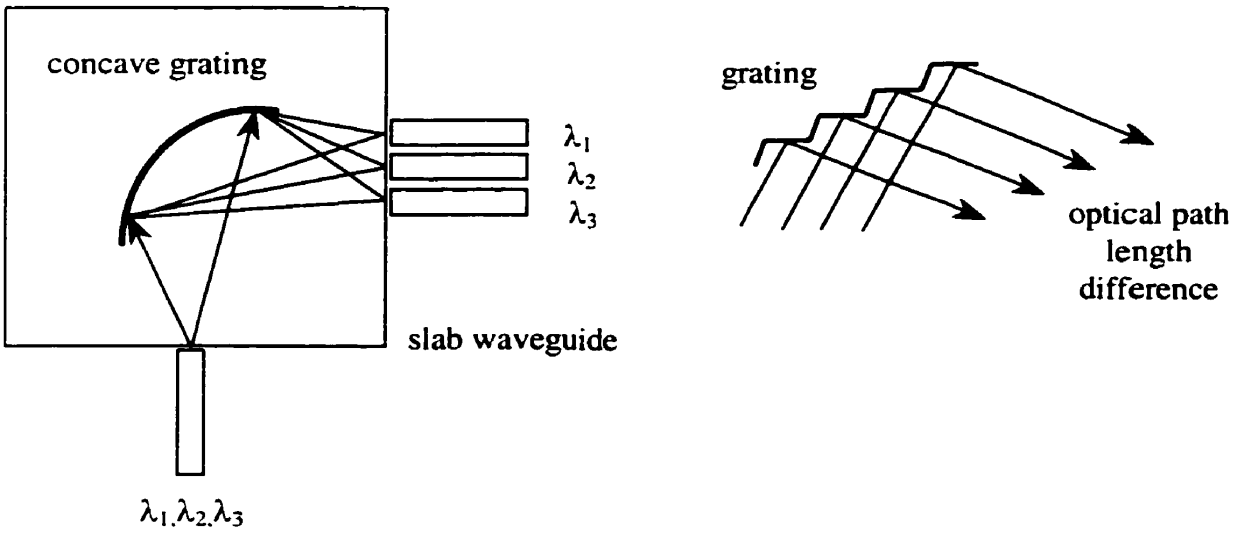

Figure 1.4 A basic concave diffraction grating demultiplexer. Multiple wavelengths are reflected, diffracted and focussed toward the output edge of the device where fibers are used to collect the separated channels.

however, grating demultiplexers have also been designed with no input or output waveguides [8,9,10]. Most use concave diffraction gratings to both diffract and focus the light. Many versions have been designed using the concave diffraction grating design [11,12,13,14].

Grating demultiplexers still tend to exhibit polarization dependence, thermal sensitivity and poorer channel isolation than other technologies; however, as stated for the arrayed waveguide devices, these problems can be rectified. The key advantage to these devices is the unlimited design flexibility in channel count. Devices have been designed and proven to show over 100 usable WDM channels in the WDM band [15]. This is a significant improvement over other demultiplexer technologies.

This work focuses on the design of an integrated diffraction grating demultiplexer based on a linear grating (grating facets lie along a linear path) rather than a concave grating. To maintain high efficiency, a concave mirror is used to focus the diffracted light toward the output waveguides.

CHAPTER TWO

WAVEGUIDE AND GRATING THEORY

2.1 LINEAR DIFFRACTION GRATINGS

Linear diffraction gratings are one of the simplest types of gratings made. Linear gratings have been traditionally common elements in optical experiments in bulk optics form. Integrated diffraction gratings are historically much newer components but they may be designed in much the same way as bulk diffraction gratings. Both integrated gratings and bulk optics gratings obey the same basic grating equations. However, the key attribute of the integrated grating is that a designer has much greater flexibility to create a grating with few aberrations. The grating facet positions may be determined by using of an iterative procedure, defining the grating facets at precise locations to achieve optimal

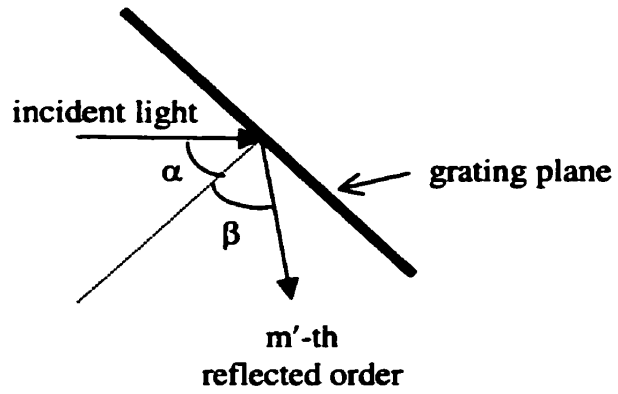

Figure 2.1 Linear grating geometry. Light is incident at α and diffracted at β with respect to the normal to the grating.

interference. In contrast to bulk optic gratings, integrated gratings with unusual periodicity or grating grooves (or slits) can be achieved without a serious increase in fabrication difficulty.

The grating equation relates the incident and diffracted angles (α and β respectively) of the light of wavelength λ with respect to the grating to the order of the grating, m' by

$$d(\sin\alpha + \sin\beta) = m'\lambda \qquad 2.1$$

where d is the distance between adjacent slits (or the grating period). In the scalar wave approximation the interference pattern from a plane wave incident on an ideal grating with infinitely long slits has an angular intensity distribution given by

$$S(\zeta) = S(0)\left(\frac{\sin\psi}{\psi}\right)^2\left(\frac{\sin(N\zeta/2)}{N\sin(\zeta/2)}\right)^2 \qquad 2.2$$

where N is the number of grating facets (or slits) and $S(0)$ is the intensity of the principle maximum [49]. The angular variables ψ and ζ as a function of the physical diffraction angle θ are given by

$$\psi = \frac{\pi}{\lambda} b \sin\theta$$
$$\zeta = \frac{\pi}{\lambda} d \sin\theta \qquad 2.3$$

and d is the slit separation, b is the slit width and λ is the wavelength of the light in the propagation medium. The grating efficiency may be improved by adjusting the slit width such that the adjacent maxima of the interference pattern (for one wavelength) are modulated out by the blaze function [16]. For maximum grating efficiency, the blaze function is designed such that the blaze function's minima coincide with the adjacent grating interference pattern maxima.

The Rayleigh criterion states that two wavelengths are just resolvable when the angular separation of their intensity maxima equals the angular halfwidth, i.e., the separation between the central maximum and the nearest minimum of the interference pattern for one wavelength. For the intensity pattern of the diffraction grating, the central maxima occur at $\zeta = 0, \pm p\pi$ (p is an integer) while the minima occur at $\zeta = \pm p\pi/N$. The central maxima of two adjacent just resolvable peaks of monochromatic light are then separated by π/N. Applying Equation 2.3 gives

$$\Delta\zeta = \frac{\pi}{N} = \frac{\pi d}{\lambda}\cos\theta\Delta\theta \qquad 2.4$$

where θ is the diffraction angle for oblique incidence. The angular half width of the central maximum is

$$\Delta\theta = \frac{\lambda}{Nd\cos\theta_m} \tag{2.5}$$

for the m'-th order . The angular dispersion of the diffraction grating $\mathcal{D}$ is defined as [49]

$$\mathcal{D} = \frac{d\theta}{d\lambda} = \frac{\Delta\theta}{\Delta\lambda} = \frac{m'}{d\cos\theta_m} \tag{2.6}$$

where $\Delta\lambda$ is the wavelength difference of the two just resolvable wavelengths. The chromatic resolving power (or resolution), $\mathcal{R}$, of the grating is defined as

$$\mathcal{R} = \frac{\lambda}{\Delta\lambda} = Nm' \tag{2.7}$$

where N is the number of grating slits that are illuminated and m' is the order of the grating. Equation 2.7 is determined by solving for $\Delta\theta$ in Equation 2.6 and combining with Equation 2.5.

An important characterizing parameter of a diffraction grating is the free spectral range. The free spectral range of the grating is defined as the range of wavelengths over which there is no overlap from diffraction patterns at different wavelengths for adjacent orders. The m'-th order diffraction peak with wavelength λ_1 will coincide with the (m'+1) order diffraction peak with wavelength λ_2 provided that

$$m'\lambda_1 = (m'+1)\lambda_2 \tag{2.8}$$

using Equation 2.1 for diffraction gratings. The free spectral range is defined as the difference between λ_1 and λ_2.

$$FSR = \frac{\lambda_1}{m'} \tag{2.9}$$

2.2 WAVEGUIDE THEORY

For any optical waveguide, the full mathematical solution of the electric field may be determined by considering the boundary value problem. Each waveguide has a unique solution that depends upon the geometry and the indices of refraction of the guiding and cladding layers. The solution of Maxwell's equations for slab waveguides gives three independent solutions for each of the three regions of interest; the two cladding layers (top and bottom) and the guiding layer. The geometry of the layer structure is shown in Figure 2.2. In this work, the cladding layers of the slab waveguide are both SiO_2 layers and therefore there is symmetry about the propagation axis (z-axis). The slab waveguide examined in this work is single mode. Similarly, the ridge waveguides examined in this work are bounded by air/core interfaces and therefore there is symmetry in this direction

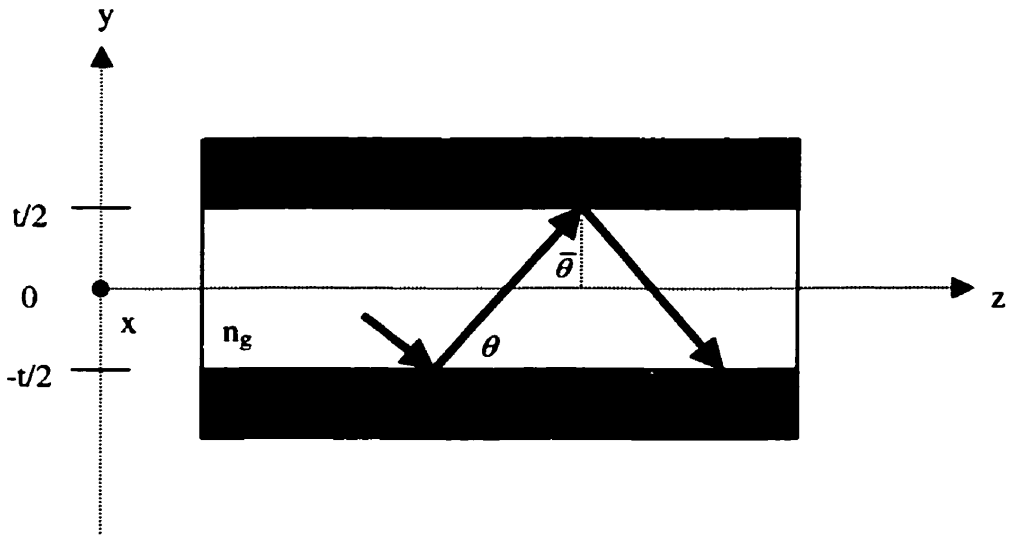

Figure 2.2 Light propagating through the slab waveguide. This shows the geometry of the slab and the defined slab thickness.

as well. These choices for system parameters have been applied in the derivations below.

2.2.1 WAVEGUIDE MODE SOLUTIONS

The electric field of the guided modes of a slab waveguide may be separated into two unique solutions, the TE (transverse electric) mode and the TM (transverse magnetic) mode. The solutions given here are derived for the TE mode only, though all steps can be followed in a completely analogous manner to determine the solutions for the TM mode. The solutions to follow are relevant for a slab waveguide where the plane of the slab is in the x-z plane (the index of refraction varies in the y-direction only).

The electric field (of the TE mode) in the cladding layers must decay exponentially for a guided wave and therefore must have the form

$$E_c = C\exp(-\gamma|y|) + D \tag{2.10}$$

for values of y such that $y > t/2$ (top cladding layer) and $y < -t/2$ (bottom cladding layer). The unknown coefficients C and D are the same for fields in both top and bottom cladding layers as the slab waveguide is symmetric about $y = 0$. The extinction coefficient γ is defined by Equation 2.15. The electric field in the guiding layer has the form

$$E_g = A\cos\left(\frac{2\pi\sin\theta_m}{\lambda}y\right) + B \tag{2.11}$$

where A and B are constants, λ is the wavelength within the waveguide [17]. The quantity θ_m is defined as the reflection angle θ of light in a mode m.

In order for a ray to be reflected from the guide-cladding interfaces and not interfere with itself upon reflection, it must obey

$$\frac{2\pi t}{\lambda}\sin\theta_m - \psi = m\pi \tag{2.12}$$

where t is the thickness of the slab and ψ is the phase introduced by reflection at the dielectric interface. The reflection phase shift ψ for a given mode m can be determined (for the TE mode) using

$$\tan(\psi/2) = \left(\frac{\sin^2\bar{\theta}_c}{\sin^2\theta_m} - 1\right)^{1/2} \tag{2.13}$$

where $\bar{\theta}_c = \cos^{-1}(n_2/n_1)$, the compliment of the critical angle. Combining Equations 2.8 and 2.9 results in a transcendental equation

$$\tan\left(\frac{\pi t}{\lambda}\sin\theta_m - \frac{m\pi}{2}\right) = \left(\frac{\sin^2\bar{\theta}_c}{\sin^2\theta_m} - 1\right)^{1/2} \tag{2.14}$$

which must be solved numerically using system parameters. Using Equations 2.10, and 2.11, and matching the solution at the boundaries ± t/2, the total solution of the electric field across the profile of the ridge waveguide may be specified. The extinction coefficient, γ,

$$\gamma = \frac{2\pi}{\lambda}\left(\frac{\cos^2\theta_m}{\cos^2\bar{\theta}_c} - 1\right)^{1/2} \tag{2.15}$$

is defined such that continuity is maintained across the boundary between the cladding and guiding layers. The full field solution can be closely approximated by a Gaussian function with tails extending into the cladding for small waveguides (waveguides with few propagating modes). A plot of the exact mode solution with a superimposed Gaussian fit is shown in Figure 2.3a for the slab waveguide parameters (2 μm width). For comparison, a similar plot is shown in Figure 2.3b for the input waveguide parameters

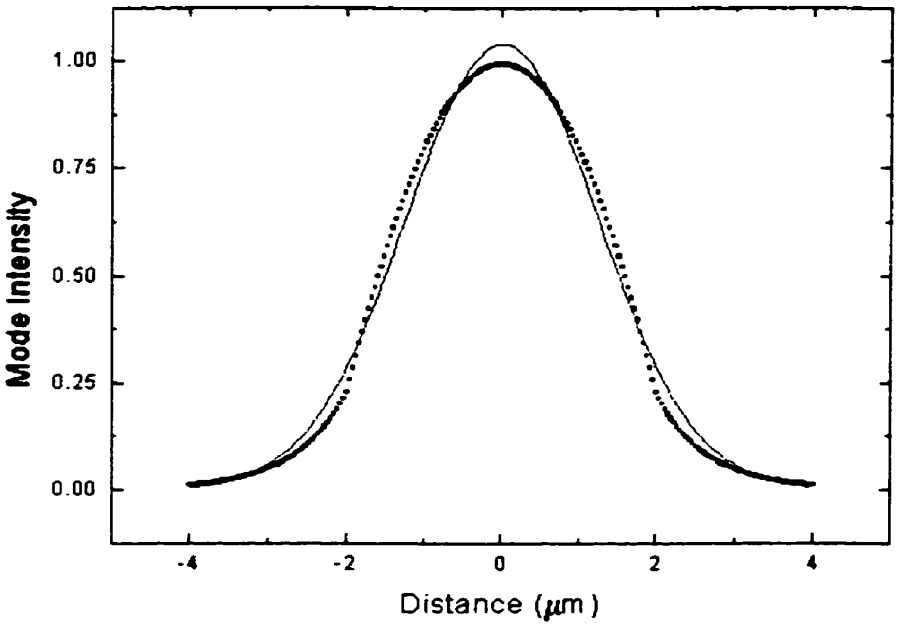

Figure 2.3a The mode intensity as a function of position in the slab waveguide where a Gaussian fit (—) is shown on the exact mode solution (■).

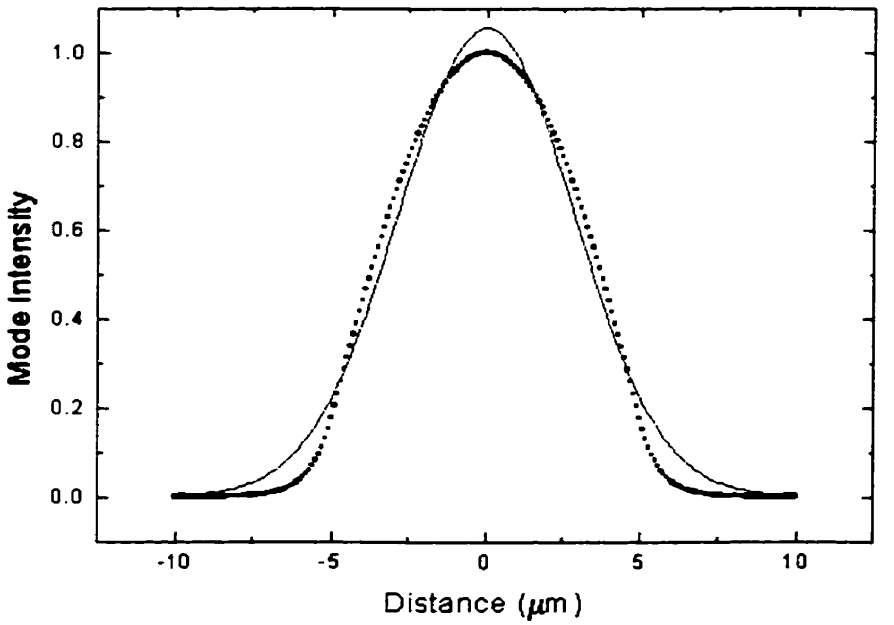

Figure 2.3b The mode intensity as a function of position in the input waveguide where a Gaussian fit (—) is shown to the exact mode solution (■).

(10 μm width). This plot shows that as the waveguide width becomes larger, the Gaussian approximation becomes less accurate. The Gaussian fit was calculated using Origin™ (a scientific graphing program) and keeping the vertical offset set to zero.

2.2.2 WAVEGUIDE DESIGN PARAMETERS

A step index waveguide is characterized by several different parameters. The effective index, N, of the waveguide is a parameter commonly used to characterize a waveguide. The effective index of the waveguide is the refractive index of a hypothetical bulk medium that would result in the same propagation constant as that seen by a particular mode in the waveguide [17]. The solution of a transcendental equation, which is arrived at by demanding continuity of the tangential electric field components (in a slightly more general fashion than that shown in Section 2.2.1), results in a value of the waveguide effective index, N.

For convenience, three new parameters are defined [19]; the normalized frequency V, the normalized guide index, b_E, and the asymmetry measure, a_E. The normalized frequency of a step index waveguide is given by

$$V = k_o t \sqrt{n_g^2 - n_s^2} \qquad 2.16$$

where k_o is the vacuum wavenumber of the light in the guide, t is the thickness of the guide layer, n_g and n_s are the refractive indices of the guide and bottom cladding layers respectively. For TE polarized light the normalized guide index is given by

$$b_E = (N^2 - n_s^2)/(n_g^2 - n_s^2) \qquad 2.17$$

and the asymmetry measure is given by

$$a_E = (n_s^2 - n_c^2)/(n_g^2 - n_s^2) \qquad 2.18$$

These new parameters are used to yield a different form of the transcendental equation given by Equation 2.14,

$$V\sqrt{1-b_E} = (m+1)\pi - \tan^{-1}\left(\sqrt{\frac{1-b_E}{b_E}}\right) - \tan^{-1}\left(\sqrt{\frac{1-b_E}{b_E + a_E}}\right) \qquad 2.19$$

The plot of Equation 2.19 in terms of b_E versus V, shown in Figure 2.4 for waveguides with m = 0,1,2 [19]. The waveguide structure defines a value for the normalized frequency V. The value of b_E defined by the curve given by Equation 2.19 (for a given m) at the structure-specified normalized frequency returns the value for the normalized frequency for the guide. A similar result can be obtained for TM polarization.

The optical spectrometer designed in this work has both single and multimode waveguides. The slab waveguide was designed to be single mode in the vertical

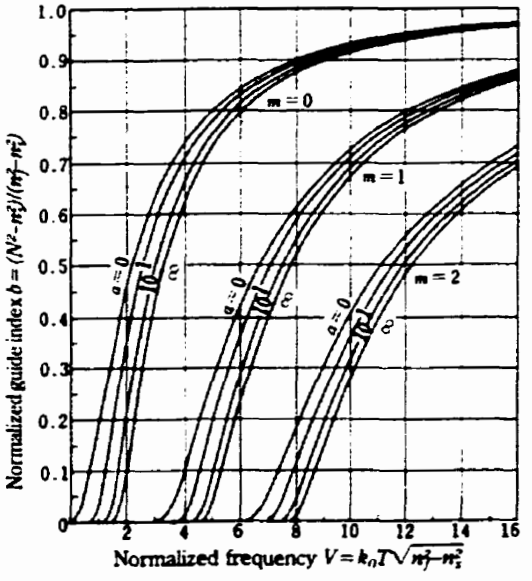

Figure 2.4 The normalized frequency of a given mode in a waveguide structure is determined by finding the intersection of the curve for the known asymmetry measure, a, for the known value of the normalized guide index, b [19].

(guiding) direction. The input and output ridge waveguides are multimode in the horizontal direction to improve coupling from the input fiber to the spectrometer (the core size of the input ridge waveguide is slightly larger than the core size of the input fiber). The requirement that must be satisfied for the waveguides to be single mode is determined by the cut-off condition for total internal reflection.

The number or modes, M, that can exist in a slab waveguide with cladding and core indices, n_c and n_g respectively is

$$M = \frac{2t}{\lambda_o} NA \tag{2.20}$$

where λ_o is the free space wavelength, t is the thickness of the guide and NA is the numerical aperture of the slab. The numerical aperture is defined as

$$NA = \sqrt{n_g^2 - n_c^2} \tag{2.21}$$

and is a measure of the range of acceptance angles of the slab. The number of modes in a waveguide is the next highest integer from the value calculated using Equation 2.20. This expression is applicable to TE modes only. For ridge waveguides, the approximate number of modes is

$$M \cong \frac{\pi ab}{\lambda_o} NA^2 \tag{2.22}$$

where a and b are the physical dimensions of the ridge waveguide cross-section. The total number of modes for a waveguide is $2M$ since there are two possible polarizations.

CHAPTER THREE

SPECTROMETER DESIGN

3.1 DESIGN OBJECTIVES

In designing a spectrometer for use in telecommunications WDM systems, there are many requirements that are imposed by industry standards and physical system requirements. These standards include such requirements as the channel center wavelength spacing, allowable insertion loss, low polarization dependent loss and dispersion, and general physical robustness. In addition to these industry-defined parameters, the linear grating spectrometer design created in this work strove to satisfy three further objectives: to keep physical size to a minimum, to have design flexibility in output channel spacing, and to allow easy access to the output channels for testing and implementation. For ease of

fabrication, the features of the grating spectrometer were kept as simple and as large as possible so as not to affect the overall performance.

3.1.1 GENERAL DESIGN OUTLINE

Minimum physical size was achieved through the use of a retro-reflecting light path. Light is launched into a slab waveguide by one of several input ridge waveguides, propagates through the slab waveguide to a concave mirror structure and is reflected toward the linear grating. The light is reflected through 180° at the grating by the retro-reflecting grating facets (to be discussed in greater detail later). After reflection, the light retraces its path back toward the input waveguide. Output collector waveguides are spaced closely (on 10 μm centers) near the input waveguides to collect the diffracted light

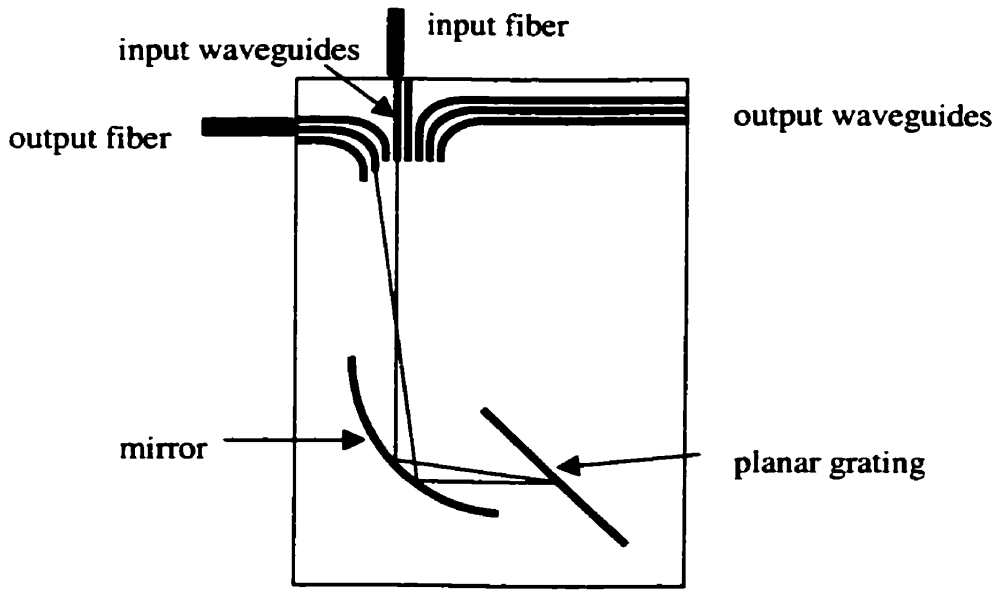

Figure 3.1 A schematic of the linear grating optical spectrometer.

focused by the mirror. The output waveguides direct the light toward the edge of the device where the signal can be detected easily with a detector array or a butt-coupled fiber. A schematic diagram of a typical linear grating spectrometer is shown in Figure 3.1.

3.1.2 LAYER STRUCTURE DESIGN

The layer structure used for the optical spectrometer waveguides consists of a SiO_2 / SiON / SiO_2 layers deposited on a Si substrate. These layers were 0.5 μm, 2 μm and 3 μm thick respectively, as shown in Figure 3.2. The slab structure was designed to be single mode for wavelengths near 1550 nm (see Section 2.2.2 for details). The indices of refraction of the layers were 1.45 for the SiO_2 layer and 1.501 for the SiON layer. These layers were grown and etched at Alberta Microelectronic Corporation by Dr. Jim Broughton. A more detailed discussion of the growth process is given in Section 4.1.1.

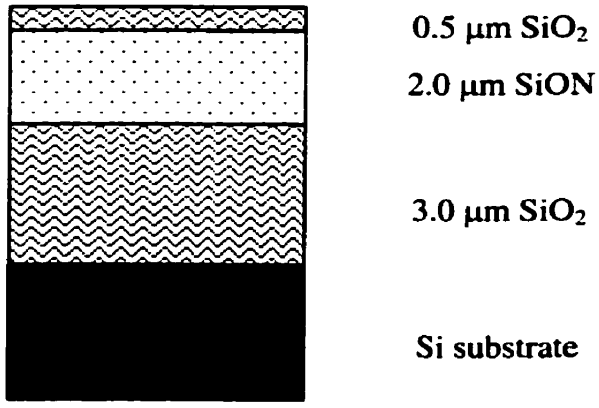

Figure 3.2 The slab waveguide of the linear spectrometer consists of SiO_2 cladding layers around a SiON guiding layer deposited on a Si substrate.

3.2 GRATING AND MIRROR DESIGN ALGORITHM

The design algorithm has two parts; an iterative procedure for defining the shape of the mirror, and the definition of the periodic grating structure. The mirror was designed to have minimal aberrations. The grating was designed to be a 16th order periodic linear reflection grating.

The grating was defined using the general equation for diffraction from a linear grating;

$$\sin\alpha + \sin\beta = \frac{m'\lambda}{d} \qquad 3.1$$

where α is the angle incidence, β is the angle of diffraction for wavelength λ, m' is the grating order and d is the grating period. The wavelength λ is the wavelength of light within the medium. This equation is derived assuming uniform field intensity across of the grating facets. The angular dispersion of a grating can be derived from the grating Equation 3.1 by taking the partial derivative with respect to β and λ. The angular dispersion of the grating is given by

$$\frac{\delta\beta}{\delta\lambda} = \frac{m'}{d\cos\beta} \qquad 3.2$$

A more meaningful parameter in the context of this work is the linear dispersion of the grating. The linear dispersion here specifically defines the linear shift of the diffracted output spot along the focal plane as a function of the wavelength. The output waveguides were positioned with knowledge of this parameter. The linear dispersion, μ, must be defined with consideration of the geometry of the device, shown schematically in Figure

3.3. Using this geometry, it is possible to relate the change of the position of the focused output spot along the assumed (locally) flat focal curve of the mirror, δu, with the change in β;

$$\delta u = \frac{f}{\cos\theta}\delta\beta \qquad 3.3$$

where f is the focal length of the mirror and θ is the angle of reflection at the mirror. The assumed local flatness, or linearity, of the focal curve allows the trigonometric definition given in Equation 3.3. The assumption of local flatness in the focal plane is an approximation; however, the focal length of the mirror was large enough that this was deemed to be a reasonable assumption for the chosen output waveguide separation δu (10 μm).

No specific knowledge of the mirror is required at this stage, other than that the mirror was assumed to be concave and followed the general properties of a concave

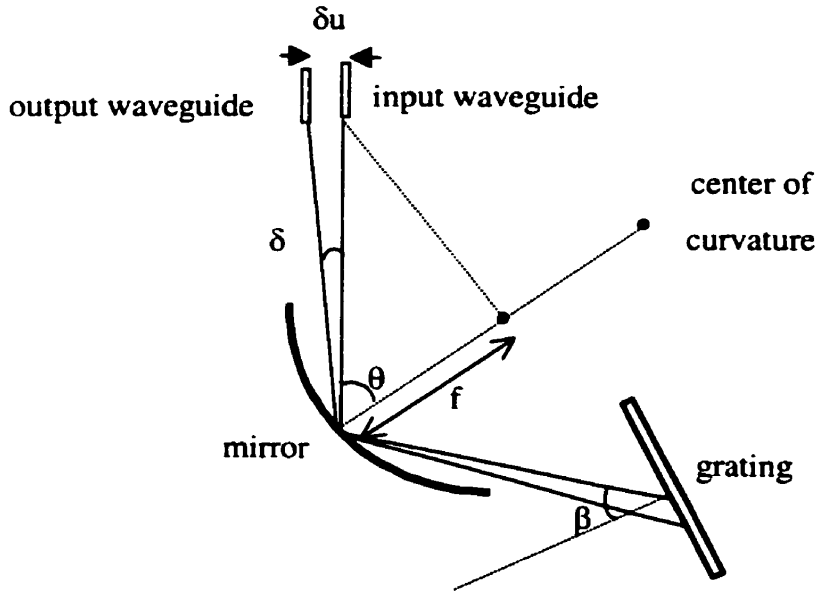

Figure 3.3 The definition of the variables used in the mirror and grating algorithms.

mirror in the paraxial approximation. Equation 3.3 is a first estimate of the position of the focal plane in this non-paraxial region. The mirror was defined recursively, therefore any choice of the starting position is valid. A value for the linear dispersion can be defined using Equations 3.2 and 3.3;

$$\mu = \frac{\delta u}{\delta \lambda} = \frac{\delta u}{\delta \beta}\frac{\delta \beta}{\delta \lambda} = \frac{m'f}{d\cos\theta\cos\beta} \qquad 3.4$$

The value of the linear dispersion was chosen with practical objectives in mind. The output channels have predetermined channel spacings (as defined by industry requirements) which set an absolute value for $\delta\lambda$. The ITU (International Telecommunications Union) standard for DWDM channel spacing is 100 GHz, or multiples thereof, and these spectrometers conform to this standard. To further constrain the value of the linear dispersion, the ITU channel wavelengths must be focused to positions along the focal plane of the mirror that have sufficient spatial separation to achieve physically realizable waveguide sizes.

The ratio of m'/d was chosen to ensure that $\alpha = \beta$, which gives the desired retro-reflecting path. This constraint is only strictly true, however, for the stigmatic wavelength. The stigmatic wavelength, the wavelength for which there are no aberrations, was chosen to be outside the WDM wavelength window. One of the designs developed in this work used a stigmatic wavelength shorter than the desired WDM transmission range (typically 1530 nm to 1570 nm) while another design used a stigmatic wavelength longer than those in the WDM window. The stigmatic wavelength was used to define the mirror facet angles as well as the ratio of m'/d. This means that there is some aberration expected in the collected light as the channel wavelength moves away

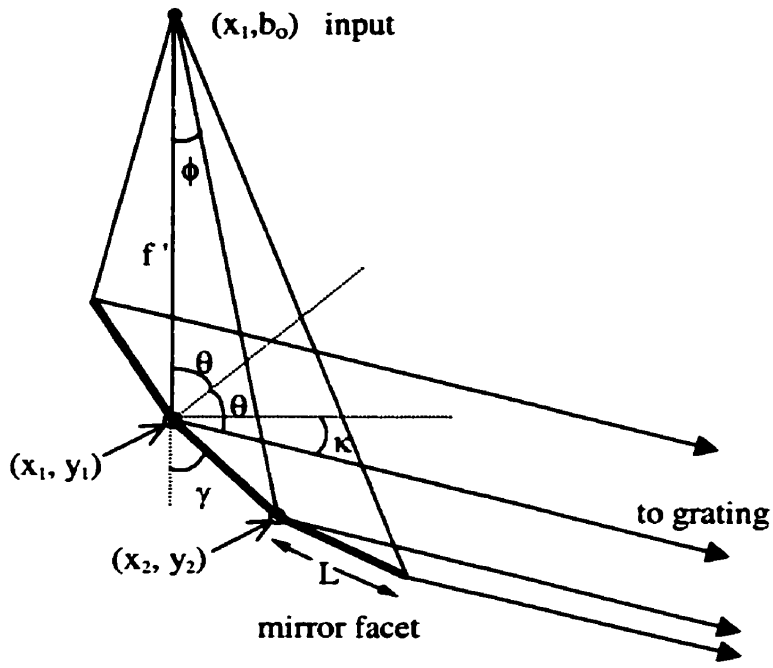

Figure 3.4 At the central mirror facet, the light reflects through an angle 2θ. All rays reflect toward the grating at an angle κ with respect to the horizontal.

from the stigmatic wavelength. With the ratio of m'/d and μ known, a value of the mirror focal length, f, was determined.

The mirror was created using a series of co-joined 1μm steps where the angle of each step was chosen to minimize aberrations along the focal plane. The end points defining the line of any one facet can be described by

$$\begin{aligned} x_2 &= x_1 + L\sin\gamma \\ y_2 &= y_1 - L\cos\gamma \end{aligned} \qquad 3.5$$

where L is the length of the mirror facet (1 μm) and (x_1,y_1) and (x_2,y_2) are the end points. The angle γ is the angle of the mirror facet with respect to the vertical (as shown in Figure 3.4). Light emanating from the input waveguide is collimated by the mirror and reflected toward the linear grating. Collimation by the mirror was ensured by the choice of the mirror facet angle γ such that all light from the input waveguide was reflected at the same

absolute angle. The mirror facet positions facilitated the calculation and mapping of the focal plane for this arrangement. The output waveguides are located along the focal plane to ensure maximum channel signal collection as well as minimizing cross-talk between channels.

With the focal length of the mirror defined by the required linear dispersion, it was possible to define the position of the individual mirror facets. The mirror was defined using the constrained reflection of a ray originating from the input waveguide (as seen in Figure 3.4). The constraint ensured two things; the definite location of the input waveguide on the focal plane of the mirror and the light incident on the grating was collimated. A consequence of the input waveguide being on the focal plane was that due to the retro-reflecting design, the output channels were also located near the focal plane of the mirror (at least for wavelengths near the stigmatic wavelength). Efficient collection of channel signal can be achieved in this orientation. The positions of the output waveguides were defined by tracing the path of light diffracted at a known angle back toward the focal plane of the mirror.

Figure 3.4 schematically shows the mirror facet geometry and the related angles. The angle ϕ defines the angular change in direction of a ray of light required such that it is reflected from the adjacent facet, i.e. the angle subtended by any given facet. The direction of the collimated light was chosen such that total internal reflection occurred at the grating for all light reflecting from the mirror. The ends of the facets were recursively defined using known angles and distances. To begin the iterative process of defining the mirror facets, $x_1 = y_1 = 0.0$, and values of θ and κ were chosen (50° and 10° respectively). Using the geometry shown in Figure 3.4, the mirror facet angle γ is given by

$$\gamma = \theta - \kappa \tag{3.6}$$

From Equation 3.5, a set of (x_2,y_2) were found to define the position of the first facet. The angle ϕ was calculated for the first facet using

$$\tan\phi = \frac{x_2}{f'} \tag{3.7}$$

where $f' = b_0 + y_2$ and b_o is the y-coordinate of the input waveguide given by

$$b_o = f(\cos\theta + \tan\theta\sin\theta) \tag{3.8}$$

For the portion of the mirror to the right of the input waveguide (the lower portion of the mirror), a new value for the reflection angle θ at the second facet is determined using

$$\theta = \frac{\pi}{4} + \frac{\phi}{2} + \frac{\kappa}{2} \tag{3.9}$$

from geometry. The set of (x_2,y_2) for the first facet becomes the set (x_1,y_1) for the adjacent mirror facet. Using Equation 3.6, a new value of γ is calculated with the new value of θ and the constant κ. The end point of the second mirror facet is calculated using Equation 3.5, and the process begins again with another calculation of f', ϕ, θ and then (x_2,y_2). This process was continued until the mirror was large enough to ensure reflection of the diverging Gaussian beam originating at the input waveguide.

A similar set of equations is applied to define the upper portion of the mirror. These equations were used to find the complete set of (x_1,y_1) and (x_2,y_2) that defines the end points of mirror facets and therefore the shape of the mirror.

The grating structure is defined by the ratio m/d and the stigmatic wavelength once the retro-reflecting condition is applied (i.e., that $\alpha=\beta$). The value of α was chosen to be 45° so that total internal reflection was achieved at the grating facet. The period of the

grating, d, was determined by choosing the grating order, m', and the stigmatic wavelength. For the conditions chosen in this work, the grating period d was 11.6 μm. The order of the grating was chosen to be 16, which is sufficiently high to produce dispersion large enough for physically realizable waveguides. The free spectral range of the grating is 96.8 nm for the center of the spectrometer's spectral range (calculated using Equation 2.4).

λ (stig.)	1526.0 nm 1576.8 nm	**α**	45°	***m'***	16	***R***	40/20 mm
β (stig.)	45°	**θ range**	45°-60°	***d***	11.6 μm	***f***	20/10 mm
θ (stig.)	50°	**κ**	10°	***L***	1.0 μm	**# grating facets**	1050
λ (stig.)	1526.0 nm 1576.8 nm	**μ**	25/12.5 μm/nm	**FSR**	96.8 nm	**n(slab)**	1.484

Table 3.1 List of mirror and grating design parameters.

3.3 RETRO-REFLECTING GRATING FACETS

The grating facets each consist of two perpendicular reflecting interfaces. The orientation of these interfaces with respect to the incident light is crucial to the proper function of the spectrometer. The facets are positioned relative to the incident direction of the light such that total internal reflection occurs at the air-guide interface. Using Snell's Law and the effective index of the guiding layer, the minimum angle of incidence required to induce total internal reflection is 42.6° (this is same for both TE and TM modes). The grating facets were oriented such that a central ray (of the impinging Gaussian beam) was

incident on the facet at 45°. The use of total internal reflection at the facets creates the highest possible reflection coefficient without the need for metallized facets. Metallization is a difficult process for which to get high yield with good reproducibility; therefore it is important to avoid it if possible. The geometry of the retro-reflecting grating facets is shown in Figure 3.5.

The retro-reflecting facets required further shape definition in addition to the angle of the perpendicular interfaces. The grating facets defined by the perpendicular interfaces required joining sections so that the grating was a solid reflecting boundary. The lengths of the two facets were chosen to minimize shadowing of the reflecting interfaces by the facet above while maintaining the grating period *d*. This was accomplished by making the longer grating interface two-thirds of the distance. The lengths of the two reflecting interfaces are s_a=7.7 μm and s_b=5.5 μm (as seen in Figure 3.5).

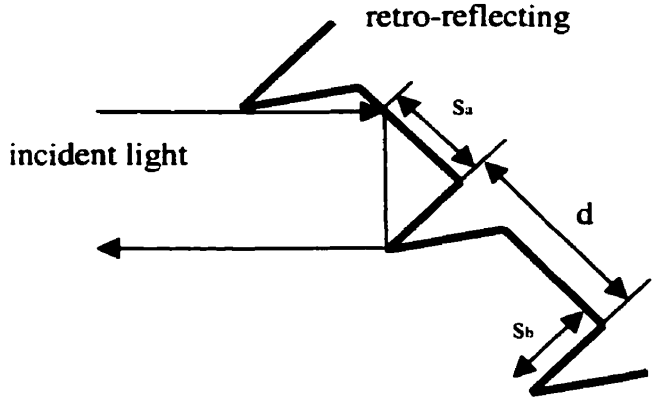

Figure 3.5 Light is reflected at the air- (on the right) waveguide (left) interfaces through 180° by the retro-reflecting grating facets. The grating has a period defined by *d*.

3.4 WAVEGUIDES

The input and output waveguides are situated along the focal curve of the concave mirror. This placement allows for maximum focusing and subsequent efficient collection of the diffracted light. The waveguide positions were calculated using the calculated diffraction angles of the WDM wavelength channels. Each WDM channel has a unique diffraction angle and is therefore focused to a different position on the mirror focal plane. These positions were calculated using two unique channel spacings; 0.4 nm, and 0.8 nm. The physical waveguide spacing along the output edge of the spectrometer was identical for both designs which made testing and possible implementation of the devices uniform.

Output (collector) waveguides are 4 μm wide and are on 10 μm centers. The guides turn through 90° toward one of the device edges (an edge adjacent to the input

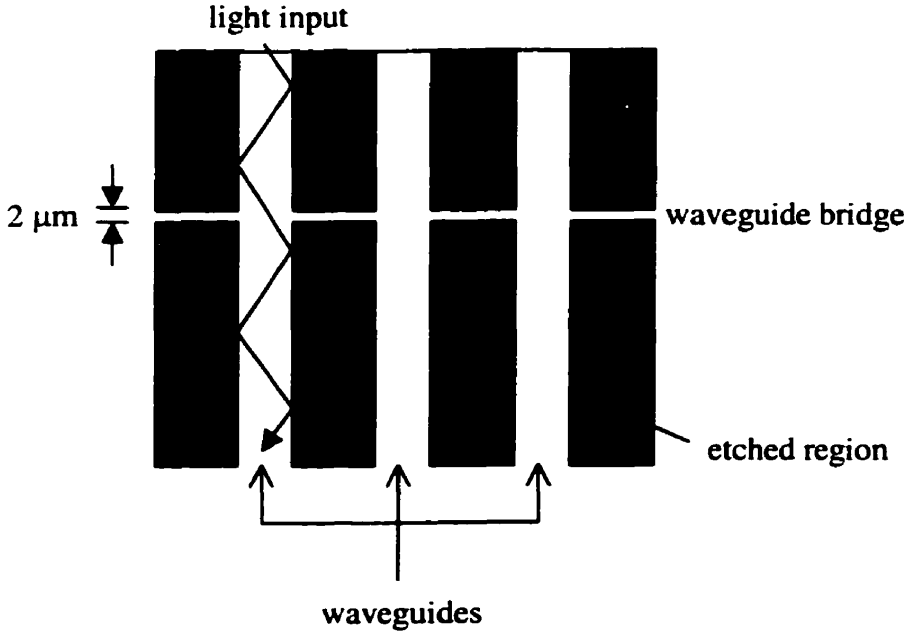

Figure 3.6 The waveguide bridges are 2 μm wide and are intended to stop the flow of index matching fluid along the length of the ridge waveguides.

waveguide edge) where signal was collected by a butt-coupled fiber. The guide spacing at the output edge of the device is 50 μm, with test channels (located at designed wavelengths 1510 nm, 1523.4 nm and 1572.5 nm) that are separated by 100 μm for easy identification. The input guides are 10 μm wide along their length and are either flared or tapered at the ends. The tapered ends provide a small beam spot image for the device while the flared waveguides were designed to allow for greater coupling of the diffracted light into the output waveguides.

The waveguides have bridges between them to help stop the flow of the index matching fluid along the full length of the waveguides. The bridges are created by masking a small part of the area between the ridge waveguides near the output edge of the device (see Figure 3.6 and 3.7) during the etching process. The masking of these areas prevents the layers from being etched and therefore a small bridge remains between the waveguides. The bridges are 2μm wide and span the distance between adjacent waveguides at the output ends. There are a total of 3 bridges along the length of the waveguides, two at the edge of the device (one at 200 μm and another 500μm from the device edge) and another near the curved sections of the waveguides. In previous designs [20] the fluid was found to wick up along the length of the waveguides by capillary action, causing a dramatic increase in loss in the ridge waveguides. The waveguide bridges were an attempt to reduce the effect of the index matching fluid on the ridge waveguides.

3.5 EXPECTED WAVEGUIDE LOSS

There are four different losses expected with the input and output waveguides. Loss is expected due to the curved nature of the output waveguides due to weak confinement of the propagating mode. Loss is expected each time there is an abrupt change from one mode field to another, therefore additional loss is expected at the input and output of the spectrometer, where optical fiber is coupled to ridge waveguides. Loss is expected due to the ridge waveguide bridges that were inserted to prevent index matching fluid from flowing along the length of the waveguides. The guided field expands in the bridge where the guide briefly becomes much wider than the ridge waveguide. The small field expansion in the bridge will cause a small loss when is it funneled back into the ridge waveguide.

The effect of the mode field mismatch, and subsequent loss, can be calculated by considering the modes in the fiber and the waveguide and applying the mode overlap integrals to get the coupling efficiency, η [17],

$$\eta = \frac{\left|\int \vec{E}_1 \cdot \vec{E}_2^{\,*} d^2x\right|^2}{\int \vec{E}_1 \cdot \vec{E}_1^{\,*} d^2x \int \vec{E}_2 \cdot \vec{E}_2^{\,*} d^2x} \qquad 3.10$$

where E_1 and E_2 are the fields in the two regions of interest. The coupling efficiency is defined as the ratio between the power coming into the junction to the power leaving the junction. As an example, the fields E_1 and E_2 could be the fields in the fiber and ridge waveguide respectively. In a similar fashion, the coupling efficiency can be calculated to

determine the loss incurred due to the ridge waveguide bridging. Results of these loss calculations are shown in Section 3.5.2.

3.5.1 WAVEGUIDE BEND LOSS

The output ridge waveguides of the optical spectrometer are curved to guide the collected light to one of the edges of the device. The waveguides are curved toward one of the adjacent edges of the devices from the input waveguides. Testing of the devices would be physically difficult if both the input and output waveguides were on the same edge of the device. The determination of the waveguide turn radius is a trade off between the physical size of the device and the amount of loss that can be tolerated in the system. As the turn radius becomes smaller, the radiated loss in the turn increases and degrades the performance of the spectrometer. If the turn radius is large, the radiated loss is reduced but the physical size of the spectrometer increases dramatically. One of the design specifications for this integrated device is to keep the physical size to a minimum therefore the turn radius must be kept as small as possible.

The derivation of the attenuation constant for curved waveguides is complicated and therefore an approximate result is shown here. For a more complete explanation of the calculation of the attenuation constant, see references Marcuse [21] and Marcatili [22]. An approximate result [19] for the attenuation constant, A, for a guide with turn radius R is

$$A \cong \frac{2\gamma_s^2 k_g^2 \exp(2\gamma_s t)}{k_o^2 \beta (N^2 - n_s^2)(2+\gamma_s t)} \exp\left(-\frac{2\gamma_s^3 R}{3\beta^2}\right) \qquad 3.11$$

if $AR<<1$ where N is the effective index of the guided mode, n_s is the index of the cladding, k_o is the vacuum wavenumber, k_g is the wavenumber in the guide, t is the guide thickness. The remaining variables are defined below;

$$\gamma_s = k_o\sqrt{N^2 - n_s^2}$$
$$\beta = k_o\sqrt{n_g^2 - 2n_s^2} \qquad 3.12$$

In the design of the waveguides used in the optical spectrometer, a bend radius of 500 μm was chosen. This radius corresponds to an attenuation loss of 0.5 dB/cm. It is important to note that these equations are derived for weakly guiding waveguides (low index contrast)

3.5.2 FIBER/RIDGE WAVEGUIDE COUPLING LOSS

To determine the loss due to fiber/waveguide coupling, it is necessary to define the electric field within the single mode (SM) fiber and the ridge waveguide. The electric

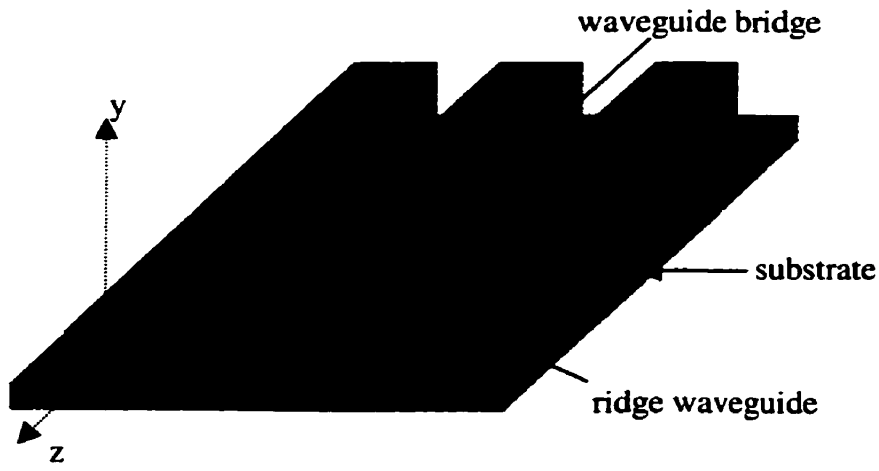

Figure 3.7 The geometry of the ridge waveguide structure is Cartesian. This shows a three-dimensional representation of the ridge waveguides and the waveguide bridges.

field can be approximated with reasonable accuracy to be a Gaussian field profile (see Section 2.2.1) across the core of the SM fiber,

$$E_1 = E_o e^{-r^2/a^2} \qquad 3.13$$

in cylindrical coordinates, where E_o is the maximum field amplitude and a is the half width of the field at $E = E_o/e$. The mode field diameter of a given fiber is a specification defined by the manufacturer. For a ridge waveguide, a more rigorous determination of the electric field may be done by solving for the field in each region (core and cladding) and matching boundary conditions (as shown in Section 2.2.1). The geometry of the ridge waveguide is Cartesian and the mode field must be defined in both the x and y directions (see Figure 3.7). The vertical axis of the ridge waveguide is defined by the slab thickness and the horizontal axis is defined by the ridge width. The full solution for the electric field within the ridge waveguide can also be closely approximated by a Gaussian function (with its peak in the center of the waveguide core) that extends into the cladding in the vertical direction and into the surrounding air in the horizontal direction. The validity of this approximation is verified in Section 2.2.1 for small waveguides. For the multimode ridge waveguides, the loss calculation assumes the existence of the first mode only and will result in an overestimate of the coupling loss.

A numerical calculation of the appropriate Gaussian function defines the width of the mode within the ridge waveguide. The knowledge of the mathematical formulae for the field in ridge and the fiber (or the ridge and the waveguide bridge) allows for easy numerical calculation of the coupling efficiency. To calculate the coupling efficiency, the field in the fiber and the field in the ridge waveguide are substituted into Equation 3.10 (as E_1 and E_2). The vertical and horizontal directions are considered independently and

the loss incurred along each axis is added to give the total coupling loss at that junction. The numerical integration was carried out by using MATLAB integration functions. The integration was done using three different algorithms so that it could be verified that the integration was algorithm-independent. The three methods were trapezoidal integration, and quadrature integration using Simpson's rule and an adaptive recursive Newton-Cotes eight panel rule [48].

The input and output ridge waveguides were designed with different widths (10 μm and 4 μm respectively). The depth of both the input and output waveguides is 2 μm (the thickness of the SiON slab guiding layer). Using the method outlined above, the mode widths of the guides are shown in Table 3.1.

	Waveguide Width (μm)	Mode Half Width (μm)
Slab thickness	2.0	1.84
Output waveguides	4.0	2.92
Input waveguides	10.0	5.97

Table 3.2 Calculated waveguide mode half widths

The effect of the waveguide bridging was determined by considering how much the guided wave changes as it propagates through the region where the guide becomes much wider than the ridge. For a given single mode waveguide (as determined above) the mode field can be approximated as a Gaussian function of known width. Using Fresnel diffraction results [17] a Gaussian beam will expand in width according to

$$w^2 = w_o^2\left(1+\left(\frac{z\lambda}{\pi w_o^2}\right)^2\right) \qquad 3.14$$

where w is the half width of the Gaussian beam at a position z away from the point where the half width was w_o. This knowledge of Gaussian beam expansion allows for estimation of the beam width after traversing the waveguide bridging. The mode sizes of the ridge waveguides are the initial sizes of the Gaussian beams (w_o) before they expand across the waveguide bridge. The amount by which w increases (from w_o) in travelling the length of the waveguide bridge, z = 2 μm, was determined using Equation 3.14. In Table 3.2, the results of the mode width expansion are shown. The Gaussian profile expands by an amount less than 0.2% of the initial width. The loss incurred from this expansion is negligible. Consequently, the waveguide bridges do not have an appreciable affect on the total on-chip loss and will therefore be ignored in further calculations.

	Expanded Field Width, w (μm)	Initial Field Width, w_o (μm)
Input waveguides	5.971	5.970
Output waveguides	2.928	2.920

Table 3.3 Calculated mode width expansion in waveguide bridges

The loss incurred due to butt-coupling the PM-SM fiber to the input and output waveguides was calculated. The mode overlap of the modes within the fiber and the ridge waveguides was an additional source of loss within the testing system. Using the

mode widths in Table 3.2, the coupling loss at the input and the output were calculated (see Table 3.2). The coupling efficiency was changed into a loss in dB using the usual formula

$$\text{loss} = 10*\log(\text{coupling efficiency}) \qquad 3.15$$

The total coupling loss must include contributions from both the vertical and horizontal directions of the ridge waveguides.

There exists a geometry mismatch between the fiber and the ridge waveguide therefore an approximation must be made. In this case it is convenient to test the mode mismatch between the fiber and the ridge waveguide by approximating the cross-section of the fiber mode to be Cartesian rather than polar. For the PM-SM fiber used in the testing, the fiber mode field was approximated by separate horizontal and vertical fields, each with a Gaussian profile with 9.0 μm full width (at $1/e^2$). This Cartesian approximation likely overestimates the true mode mismatch but is sufficient to estimate the loss expected due to fiber-guide coupling. The results of the coupling loss calculations are shown in Table 3.3. The total coupling loss was determined by adding the loss incurred due to mismatch in the vertical and horizontal directions.

	Fiber-Ridge Coupling Loss; horizontal (dB)	Fiber-Slab Coupling Loss; vertical (dB)	Total Coupling Loss (dB)
Input Waveguides	-0.17	-1.54	-1.71
Output Waveguides	-0.39	-1.54	-1.93

Table 3.4 Coupling losses at fiber/ridge waveguide interfaces

CHAPTER FOUR

SPECTROMETER FABRICATION AND CHARACTERIZATION METHODS

4.1 SPECTROMETER FABRICATION

The first step in creating an integrated spectrometer is the fabrication of the slab waveguide layers. This requires the deposition of three layers of material on a substrate, two cladding layers and one guiding layer. Once these layers have been deposited at the desired thickness and refractive index, the integrated structures of the spectrometer are patterned and etched.

In order to create the definite air-waveguide interface required for reflection from the grating facets, sections of the slab waveguide must be etched away at precisely

defined locations. Blocks of the slab waveguide were etched away to create a vertical boundary. One edge of each block defines the reflecting (refracting) surface. Many etched blocks stacked together create the full length of the grating. In a similar fashion, a mirror can be etched into the waveguide structure by defining an array of blocks to create a stepwise continuous interface. Any feature required in the waveguide structure (ridge waveguides, alignment marks, identification symbols) may be created by an amalgamation of etched blocks.

4.1.1 WAVEGUIDE LAYER DEPOSITION

The waveguide layers were deposited using plasma enhanced chemical vapor deposition (PECVD). This method introduces several gases into the deposition chamber which react with each other and are slowly deposited on the substrate. The substrate is typically held at a temperature of between 200-350°C to create part of the energy needed to induce chemical reactions in the gaseous reactants. More energy is supplied to the reactants by an RF field created between the substrate (one electrode) and another electrode. Plasma is created between the electrodes to help begin the chemical reaction processes. The substrate may be held at a lower temperature in PECVD compared to other deposition processes since part of the reaction energy is supplied by the plasma, rather than all by the heat of the substrate [17]. For the SiON layer, SiH_4 (silane), NH_3 (ammonia), N_2O (nitrous oxide), He and N were used as the reacting gases. The ammonia was used to increase the index of the core layer.

4.1.2 PHOTOMASK DESIGN PROCESS

Fabrication of etched structures begins with the design of a photomask. The photomask acts as a stencil for outlining the etching features. The relative positions of the grating facets were determined using grating theory outlined in Section 3.2. These positions (determined to within 0.001 μm) were used to define etching blocks. Mapping of the etching blocks is typically done using a CAD (computer aided design) program where features of the mask may be defined with precision. Special commercial software exists that caters to this specific type of design work, though any CAD program (AutoCad for example) may be used. Photomask design for this project was done using a CAD program called L-Edit™ (by Tanner Research, Inc). L-Edit™ is a layout editor developed specifically with IC design in mind. This software allows for easy importation of design parameters (in the form of etch block coordinates in this case) as well as exportation of the completed mask design in formats that are compatible with the mask fabrication equipment.

The etch block data are written to a file in the form of plotting commands in CIF (Caltech Intermediate Form) format. These commands describe for the layout editor the absolute position, size and orientation of each etch block. The CIF file is a list of definitions of all the polygons that will be etched into the waveguide layers. The layout editor translates the list into a visual plot of the etch blocks. The designer has the choice of defining the pieces that will be etched or the pieces that will remain after etching is completed. In many cases the simplest choice is defining the pieces that will remain. In this work, the photomask was designed to expose the etch blocks. The CIF file was

written to include the coordinates of the grating facets, the mirror facets, and the waveguide outlining structures. The full mask layout was sent to Nortel (Ottawa, Photomask Department) for Cr photomask fabrication. Once the photomask was fabricated it was sent to Alberta Microelectronic Corporation (Edmonton) where the etching process was performed by Dr. Jim Broughton in a proprietary fabrication process.

4.1.3 LAYER ETCHING PROCESS

After the layers were deposited on the substrate, the layers needed to be etched with the photomask pattern. A thin layer of photoresist was spun on to the waveguide layers. Two types of photoresist can be used in this kind of etching. One type of photoresist (negative) is hardened when exposed to UV light and remains attached to the layers after

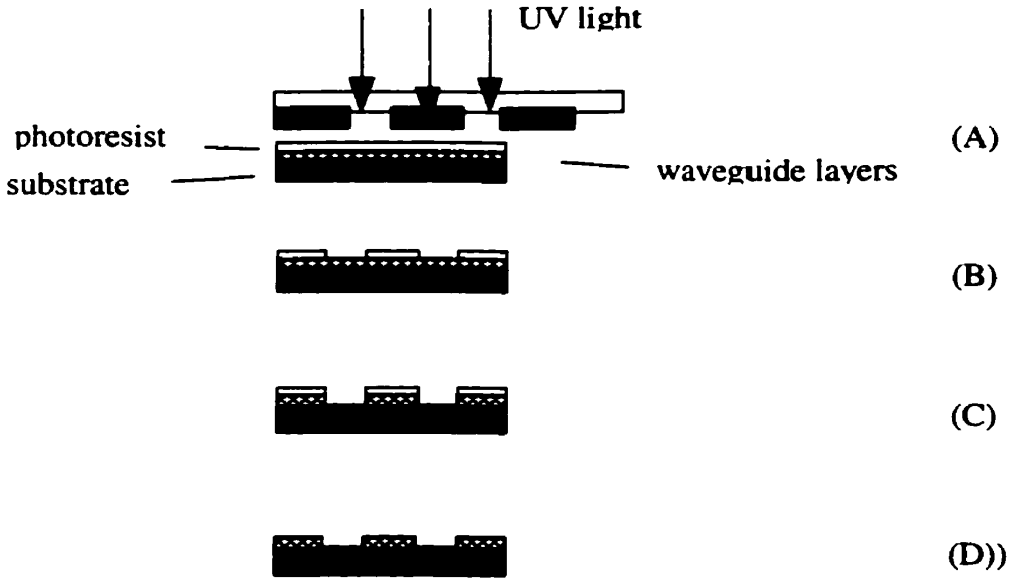

Figure 4.1 The layer etching process. The layer of photoresist is exposed to UV light (A) and the exposed regions are washed away (B). The revealed sections of the waveguide layers are etched using RIE (C) and the remaining photoresist is washed off (D) rendering the final product.

the rinsing process. The second type of photoresist (positive) will wash away after exposure to UV light. For this application positive photoresist was used so that the photomask could be used as a stencil to define the etching region. The photomask was placed over the layers coated with photoresist and exposed to UV light. After washing away the exposed photoresist, the remaining photoresist is hardened by baking to ensure good adherence to the layer surface during etching.

Reactive Ion Etching (RIE) was used to etch the layers of the waveguide into the grating and waveguide features. RIE is considered to be a dry etching technique where a molecular gas is decomposed by an RF field creating a plasma. The corrosive plasma reacts with the waveguide layers which results in etching of the layers. The etchant is chosen to be highly corrosive to the layers while leaving the mask in tact. This allows the technique to be flexible in terms of etch depth and etch verticality. The etched material is pumped away from the layers so that there is no redeposition of the etched particles. A schematic view of the etching process is shown in Figure 4.1. A special etching process for the layers used in this work was defined by Sun [20].

4.2 EXPERIMENTAL PROCEDURE

4.2.1 SPECTROMETER SPECTRA COLLECTION

In testing and characterizing the spectrometers, a tunable diode laser was used as an IR source. The light was passed through a half wave plate to ensure that the light entering the spectrometers was entirely TE mode (or TM mode). A chopper was placed in the

path of the beam to make detection of the spectrometer output signal easier (with the use of a lock-in amplifier). The laser light was focused into a polarization maintaining, single mode (PM-SM), jacketed optical fiber. The opposite end of the PM-SM fiber was butt-coupled to the edge of the device and aligned with one of the input waveguides on the spectrometer (with the help of a microscope). Refractive index matching fluid was applied to the end of the fiber to ensure efficient coupling of the light into the input ridge waveguide. At the output facet of the spectrometer, another butt-coupled PM-SM fiber was used to detect the signal collected by the output waveguides. Index matching fluid was used at the contact point between the fiber and the spectrometer output waveguide. The collected light was detected by a photodiode and passed to a lock-in amplifier.

A reference signal was measured for each data set by measuring the fiber to fiber signal. The fiber to fiber measurement was achieved by butt-coupling the input and output fibers and measuring the signal. This reference signal was considered to be the

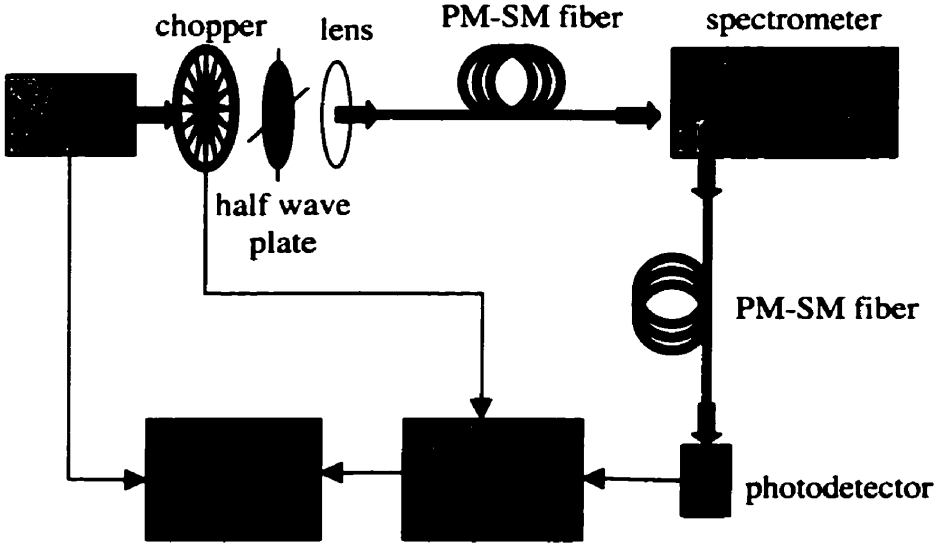

Figure 4.2 The experimental apparatus for collecting spectrometer output spectra.

total amount of light that can pass through the spectrometer. The fiber to fiber signal was used as the reference when calculating the total loss of a spectrometer. The detected signal was passed through a low noise current pre-amplifier which reduced the collected signal by a factor of 1000 so that the lock-in amplifier did not over-load.

To collect the spectrometer spectra shown in Figure 5.1 (for example), the input fiber was aligned to one of the input ridge waveguides. The fiber's vertical and horizontal positions were chosen by sight (using a stereo microscope) and then more precisely using a visible laser source. The visible laser light could be seen traversing the ridge waveguides and reflecting off of the mirror and grating if the fiber was well-aligned. The visible light could escape from the slab and ridge waveguides because the waveguides were not designed to be efficient at visible wavelengths. A similar procedure was used to align the output collection fiber with one of the output ridge waveguides. The wavelength of the tunable diode laser was scanned until the lock-in amplifier registered a maximum in signal. The fibers were then adjusted once more to ensure optimal coupling. A GPIB (general purpose interface bus, also known as IEEE-488 interface) card was used to control data collection from the laser and the lock-in amplifier. A custom data acquisition program was developed, in stages, by several students (Jeff Giesbrecht, the author and Dan Jackson, in chronological order) for this project. It was designed to perform a wavelength scan on the laser (on nanometer or Angstrom scales), to collect the wavelength and output power from the laser and to collect the spectrometer output signal from the lock-in amplifier. Each spectrometer channel was scanned individually over a 3 - 4 nm range around the peak center wavelength in order to characterize the signal for each channel. This procedure was repeated for each output channel waveguide.

The spectrometers' performance with respect to polarization sensitivity and input channel choice were also measured. Polarization sensitivity was determined by collecting spectra (in the manner described above) for both the TE and TM polarizations for selected output waveguide channels. The switch between TE and TM light was achieved by rotating the half-wave plate inserted between the laser and the input fiber. A rotation of the half-wave plate by 45° changed the polarization from TE to TM or visa versa. Polarization sensitivity spectra are shown in Section 5.3. The choice of input channel shifted the spectra collected at the output waveguides (as expected) and this was also characterized. Output spectra were collected by (signal as a function of wavelength) using one output waveguide while the input waveguide was changed. The results of these measurements may be seen in Section 5.4.

4.2.2 SLAB LOSS DETERMINATION

Loss in the slab waveguides was measured in much the same way as outlined for the spectrometer characterization. The input PM-SM fiber was butt-coupled to a section of the slab where no etched features existed. The input signal traveled through the slab and emerged on the other side where it was collected by another butt-coupled PM-SM fiber. The peak signal along the output edge of the slab was measured and recorded as a function of wavelength. The divergence of the beam in the slab was calculated using Gaussian beam theory (see Section 3.5.2). The core of the fiber is small (roughly 9 μm in diameter) therefore it is expected that not all of the light will be collected at the output edge due to the beam divergence through the slab. Using the mode overlap integral (see

Section 3.5), the slab loss was calculated due to the size mismatch of the beam spot and the fiber core. Additional loss was expected due to insertion mode mismatch in the vertical direction. The results from these measurements are discussed in Section 5.1.

CHAPTER FIVE

SPECTROMETER PERFORMANCE

5.1 PERFORMANCE OBJECTIVES

The concept of the grating spectrometer is not a new one; however, in spite of many attempts to make this technology a viable product, the performance of these devices must be improved for use in telecommunications applications. Specifically, the greatest areas of interest have been the channel cross-talk, the insertion loss (on-chip loss), channel spectral shape (including side lobes and flat-top channel intensity) and channel-to-channel loss variation. There is room for improvement in all of these areas.

The grating demultiplexers that have been designed in recent years have been based on the concave grating design [8,10-15,25]. These gratings tend to suffer due to

changes in facet size and shape along the length of the grating. In the concave grating, the changing facet positions alter the sharpness of the corners along the length. During fabrication, some of the facets may be well-formed while others are not, creating a non-uniformity along the grating. The changes in size and shape alter the output spectral shape of every channel because the size of the facet is directly related to the intensity distribution (see Section 2.1). A linear grating has identical facet shape and orientation along the length of the grating which should improve the spectral shape of the output channels (in theory). Identical facet shape and orientation may also reduce the effects of corner rounding during fabrication. The facets may be oriented in such a way that the features produced can be reliably reproduced during etching.

The impetus of this work on linear gratings is the assumption that reduction and minimization of non-uniformity along the linear grating will improve the spectral shape of the individual channels. An improved spectral shape refers to narrower spectra (in wavelength) and lower side lobes (relative to the central peak). With these improvements, one can expect lower channel cross-talk and perhaps reduced channel-to-channel loss variations.

In this chapter, the performance of the linear grating spectrometers designed in this work will be discussed. The loss profile of each design will be examined, the channel spacing and polarization dependent performance. The performance of this spectrometer will be compared with the performance of similar devices found in the literature.

5.2 SLAB WAVEGUIDE LOSS

The backbone of the integrated spectrometer is the slab into which it is etched. It is crucial to understand the characteristics of the slab before spectrometer characterization can begin. Due to the intrinsic properties of the slab waveguide medium, losses are incurred as the light propagates through the medium. This loss can be determined by measuring the light transmitted through only the slab waveguide (no interactions with any of the etched features of the spectrometer). The loss of the slab waveguide was characterized as a function of wavelength. A graph of the loss as a function of wavelength is shown in Figure 5.1a. These data were taken by transmitting light through a section of the slab waveguide that was 2.05 cm long. It is clear that the loss is

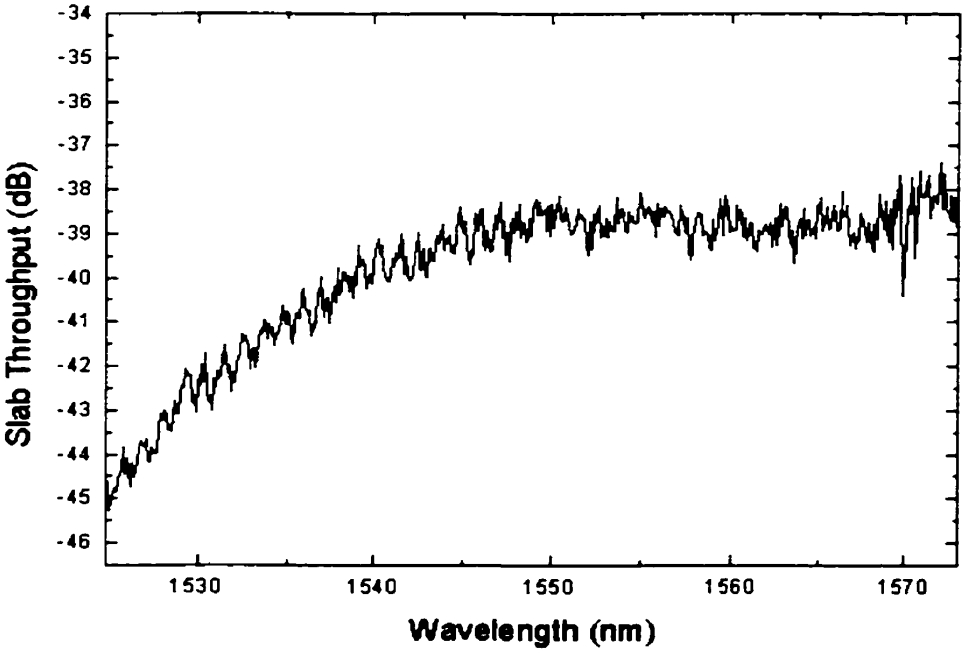

Figure 5.1a The loss profile as a function of wavelength due to propagation through 2.05 cm of the slab waveguide. There is significant absorption near 1530 nm.

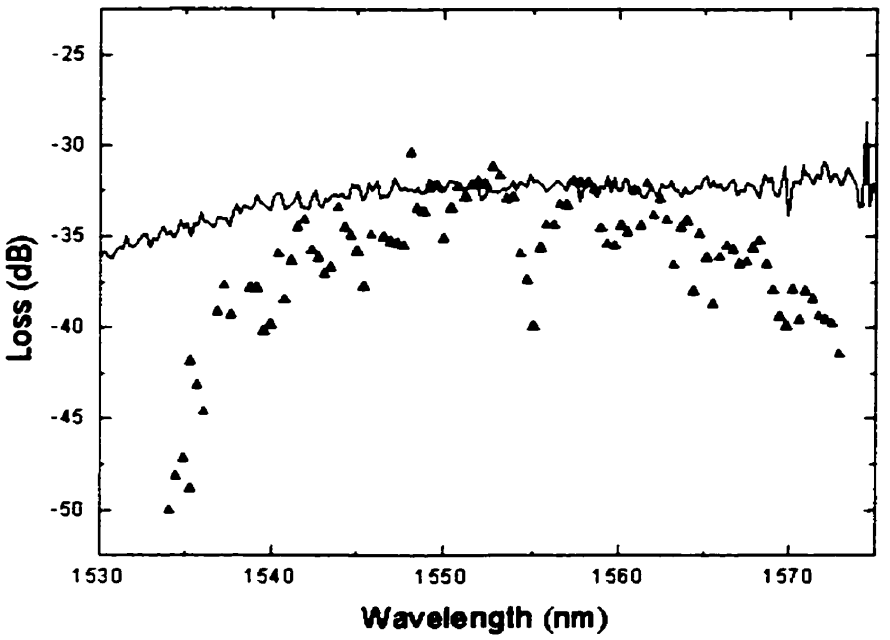

Figure 5.1b The slab loss profile (solid line) superimposed on the output channel loss (triangles) as a function of wavelength for a Design A spectrometer.

dependent on the wavelength. These data were not corrected for coupling loss, propagation loss or loss due to the Gaussian expansion of the beam through the slab (hence not all of the light was collected). The loss profile of the spectrometer output channels is shown in Figure 5.1b. The loss profile of the slab itself is superimposed on the spectrometer profile for comparison purposes. The slab loss profile was rescaled such that the maximum of the spectrometer profile coincides with the slab loss profile. It is clear that the spectrometer loss profile is affected by the slab wavelength-dependent loss.

In order to reduce the wavelength dependence of the slab waveguide loss, annealing was considered to break the O-H bonds that cause absorption near 1510 nm. The wafers were annealed before etching in an effort to level the roll-off near 1540 nm. Previous work has been done by fellow graduate student Dan Jackson [23] which shows the roll-off can in fact be reduced; however these wafers were not annealed using the

proven formula. The annealing was performed over a period of 24 hours. The exact annealing recipe is proprietary to Alberta Microelectronic Corporation. As is clear in Figure 5.1a, the annealing has not eliminated the roll-off and total slab loss was found to have been increased due to the annealing compared to other similar slab waveguides. The wavelength dependence of the slab waveguide loss must be addressed before this type of spectrometer device could be considered as a viable product. Despite this shortcoming, these changes are beyond the scope of this project. The effect that the annealing procedure had on the intended index of refraction of the slab waveguide will be discussed in Section 5.8.

The loss due to absorption in the slab waveguide was measured to be 3.3 dB/cm (at 1550.0 nm). This is a significant loss contribution and must be improved for subsequent designs. For design A, which has an on-chip optical path length of 6.5 cm, the slab contributes to 21 dB of the total on-chip loss. For designs B (path length of 4.1 cm) and C (path length of 4.7 cm), the slab contributes a loss of 14 dB and 15 dB respectively.

5.3 SPECTROMETER DESIGNS

There are three different spectrometer designs that will be examined in this work. Each design is based on the same algorithm as outlined in Section 3.2 but has slight parameter changes. Common features of the three designs include: the effective index of refraction for the TE polarization (1.484); slab and ridge waveguide dimensions; output waveguide

curve radius; output dispersion (the change in output focal point position with wavelength); planar grating orientation with respect to the incident light; and the order of the grating (m = 16). The major differences between the designs are the output channel spacing (in wavelength) and the stigmatic wavelength. The stigmatic wavelength is defined as the wavelength at which there are no aberrations. In these designs, the stigmatic wavelength corresponds to the wavelength that is retro-reflected back toward the input waveguide. Table 5.1 shows a comparison of the designs in terms of their design parameters, physical size and on-chip optical path length.

Design	Output Wavelength Separation	Stigmatic Wavelength	Physical Dimensions	On-Chip Optical Path Length	Theoretical Resolution
A	0.4 nm	1526.0 nm	2.1 x 4.1 cm	6.52 cm	0.16 nm
B	0.8 nm	1526.0 nm	2.1 x 2.4 cm	4.12 cm	0.25 nm
C	0.8 nm	1576.8 nm	2.1 x 2.4 cm	4.71 cm	0.25 nm

Table 5.1 Design parameters for the three spectrometer designs investigated in this work.

5.4 WAVELENGTH DEPENDENT LOSS

The loss incurred for each channel changes as a function of wavelength. As discussed in Section 5.2, the slab waveguide will contribute to the wavelength dependent performance of the spectrometers, however, this is not the only contribution. Additional wavelength

dependent performance is due to the characteristics of the diffraction grating. Incomplete collection of the output channels may also have been a cause of some of the wavelength dependent performance. The positions of the output collector waveguides were determined recursively from the chosen position at the stigmatic wavelength. There is a possibility that the positions of the waveguides far from the stigmatic wavelength are not positioned on the focal plane of the mirror, causing the collected light to be defocused and therefore not completely collected by each output spot. Each of the three designs exhibits a different loss profile and each of these profiles are shown and compared in this section.

5.4.1 SLAB LOSS CONTRIBUTION

As is shown in Figures 5.1a and 5.1b, the slab contributes significantly to loss at the low wavelength end of the spectra. Near 1530 nm, increased absorption in the slab waveguide will contribute a futher 4 dB of loss from that incurred at wavelengths higher than 1545 nm. In Designs A, B and C the propagation lengths in the slab only (excluding the distance traveled in the ridge waveguides) are 5.19 cm, 3.18 cm and 3.05 cm respectively. The propagation distance in the slab is important, however propagation distance in the ridge waveguides changes more significantly for different wavelengths. This effect will be discussed in Section 5.4.3.

5.4.2 OUTPUT DEFOCUSING LOSS

The positions of the output collector waveguides were chosen in a recursive manner from the choice of the position of the input waveguide. The stigmatic wavelength in these designs is retro-reflected. The linear dispersion at the output focal plane of the mirror was used to determine the positions of the diffracted output spots. Any cumulative error in determining the output waveguide positions would increase for collected output wavelengths far from the stigmatic wavelength. For Designs A and B, cumulative error would affect wavelengths near 1570 nm while for Design C the affected wavelengths would be near 1530 nm.

The algorithm that generated the focal curve of the mirror (and therefore the positions of the output waveguides) found the output focal point for a given wavelength by determining the intersection of two rays reflected by two mirror facets on either side of the center of the mirror. This method is excellent for wavelengths near the stigmatic wavelength (the mirror was shaped to ensure true retro-reflection of the stigmatic wavelength); however some aberration appears for wavelengths far from the stigmatic wavelength. The intersection of rays reflected by 3 different sets of mirror facets were calculated to determine if the intersection points changed as a function of wavelength. The change in the intersection positions is small but it increases monotonically from the stigmatic wavelength. For the Design B devices the channels near 1530 nm had intersection points shifted by ±0.2 μm in both the x- and y-directions while channels near 1570 nm had their intersection points shifted by ±0.6 μm in the x-direction and ±1.0 μm in the y-direction. This shift in the positions of the intersection points means that the

focused spot will be blurred and dispersed. The increase in spot size will cause an increase in cross-talk and loss for channels far from the stigmatic wavelength.

5.4.3 RIDGE WAVEGUIDE ABNORMALITIES

In each of the designs, the relative loss between adjacent channels varies, in a manner that is not fully accounted for by the overall trends discussed above. The change in the loss between adjacent channels is due to the quality of the output waveguides and the effect of the index matching fluid. The index matching fluid had a tendency to flow along the length of the ridge waveguides, despite the precautions taken by adding the waveguide bridges (see Section 3.4). As the fluid flowed in the region between the output waveguides, the index profile of the waveguides changed and considerable loss was realized due to leakage.

The length of the ridge waveguide changed monotonically as the passband wavelength increased. The loss within the ridge waveguides could not be measured because experimental procedure coated the ridge waveguides with index matching fluid which changed the properties of the ridge waveguides. Loss due to propagation through the ridge waveguides is expected to be higher than that due to propagation through the slab. The increased loss is due to non-uniformity in the side walls of the ridges formed during etching. This means that designs with longer output ridge waveguide lengths are expected to show higher loss. For Designs A and B, the length of the output ridge waveguides was the longest for wavelengths near 1530 nm (9.4 mm and 6.7 mm respectively). For wavelengths near 1570 nm the length of the ridge waveguides were 4.2

mm and 4.8 mm for Designs A and B respectively. In Design C, wavelengths near 1530 nm (far from the stigmatic wavelength) traveled 7.4 mm in the ridge waveguide while wavelengths near 1570 nm traveled 10.1 mm in the ridge waveguide. These figures imply that the high wavelength end of the Design A and B spectrometers as well as the low wavelength end of the Design C spectra would incur higher loss (due to propagation loss) than the opposite ends of their wavelength spectra.

Another reason for the change in output signal between channels is that the ridge waveguides very likely had varying loss relative to one another. This is a reasonable hypothesis because there were a couple of ridge waveguides on each device that were not fully formed. The breaks in the ridge waveguides could be seen through a microscope under 50 times magnification. If some of the waveguides were not fully formed, it is reasonable to assume that there were other significant flaws in the ridge waveguides (not immediately visible) that affected the waveguide throughput. The ridge waveguides should be made wider (than the 4 μm used here) to avoid these fabrication problems.

5.4.4 SPECTROMETER LOSS PROFILES

All of the figures shown in this section are plotted as a function of fiber to fiber loss. The collected signal was normalized for laser power fluctuations. The fiber to fiber loss includes the coupling loss, slab waveguide loss, ridge waveguide loss and all losses due to reflections at air/guide interfaces.

Spectrometer design A is physically the largest of the three designs. The increased physical size allows for the spatial separation of the narrowly spaced (0.4 nm or 50 GHz) spectrometer channels. From the two wafers that were fabricated for this work, three of the four spectrometers with design A were useable. The array of all output channel spectra for the three devices are shown in Figures 5.2 through 5.4. The output channels showed significant loss variation across the WDM wavelength range.

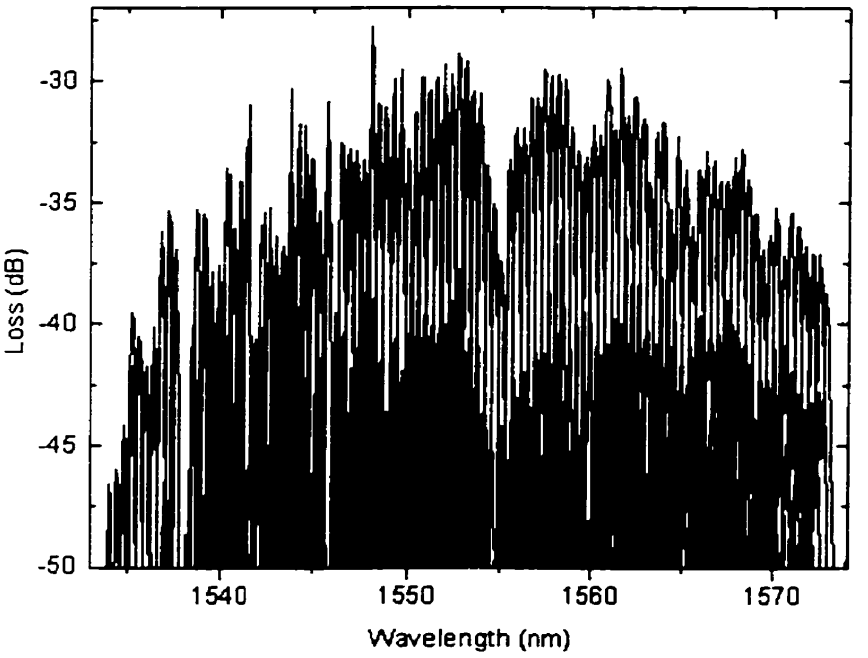

Figure 5.2 The full output spectrum of a Design A (0.4 nm spacing) device.

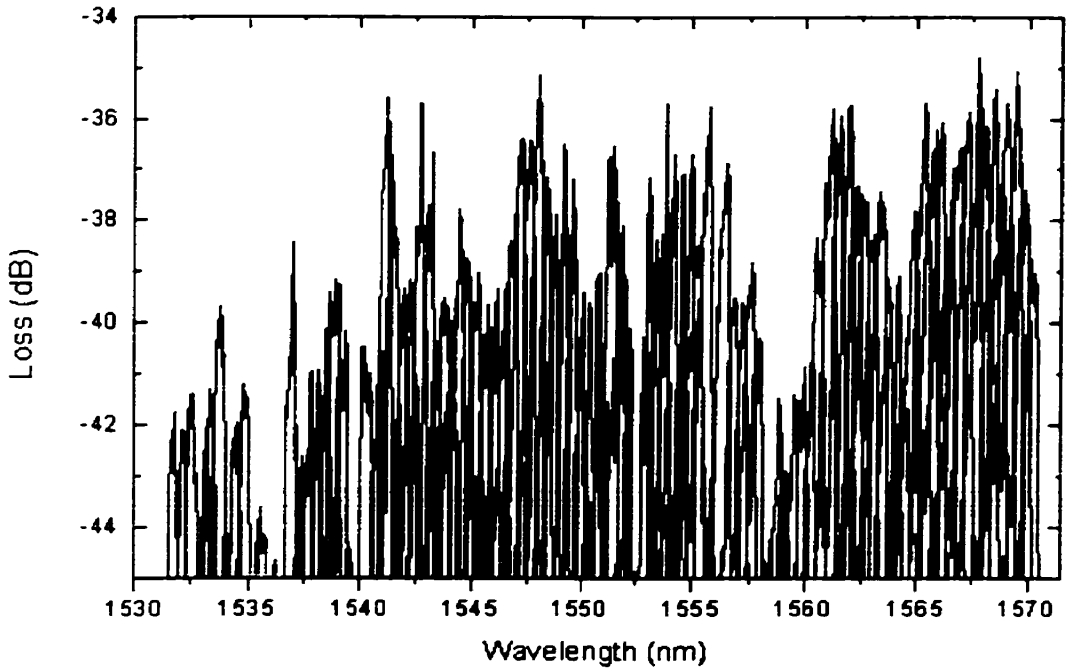

Figure 5.3 The full output channel spectrum for a second Design A spectrometer.

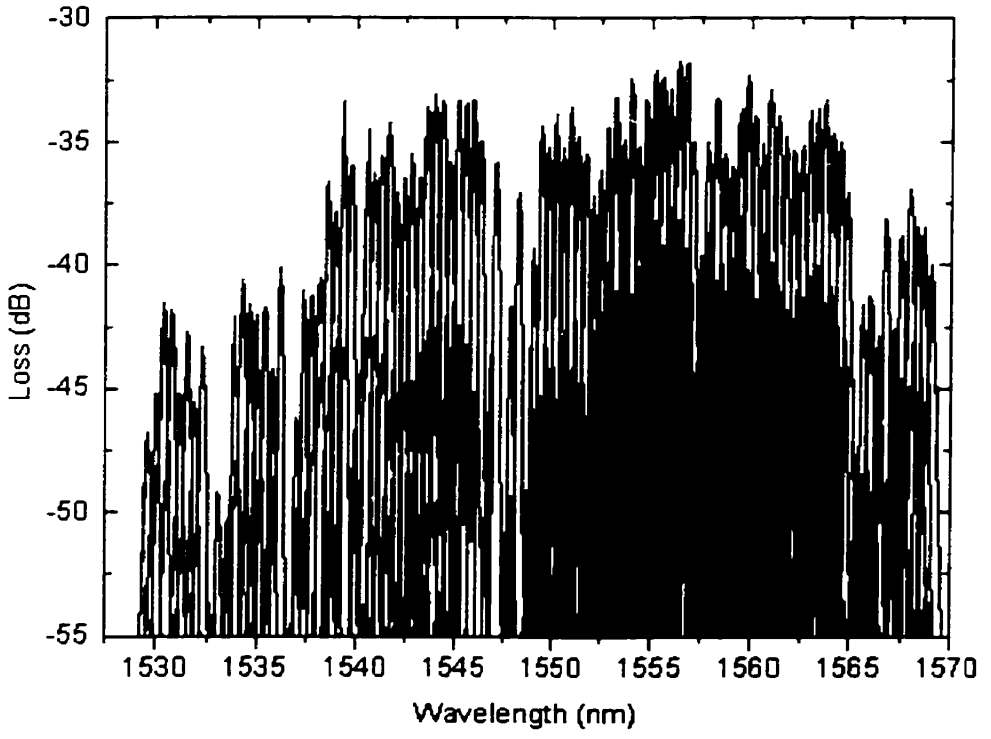

Figure 5.4 The full output channel spectrum for a third Design A spectrometer.

In spite of being the largest of the designs, the Design A spectrometers showed comparable total on-chip loss to the considerably smaller Designs B and C. The best performance in all three designs showed 30 dB loss for the most efficient channels.

In Figure 5.1b, the slab waveguide loss profile is superimposed on the spectrometer loss profile for Design A. The slab loss profile was rescaled so that the two plots overlapped. It is likely that the slab waveguide contributes significantly to the wavelength dependent loss roll-off at the low-wavelength end but there must be another effect on the loss profile of the spectrometer as the two plots in Figure 5.1b do not coincide. Design A spectrometers likely suffer from the defocusing loss described above as there is significant loss for wavelengths higher than 1562 nm. This loss ranges from 4 dB to 8 dB for the devices tested. However, there exists excess loss for the wavelengths

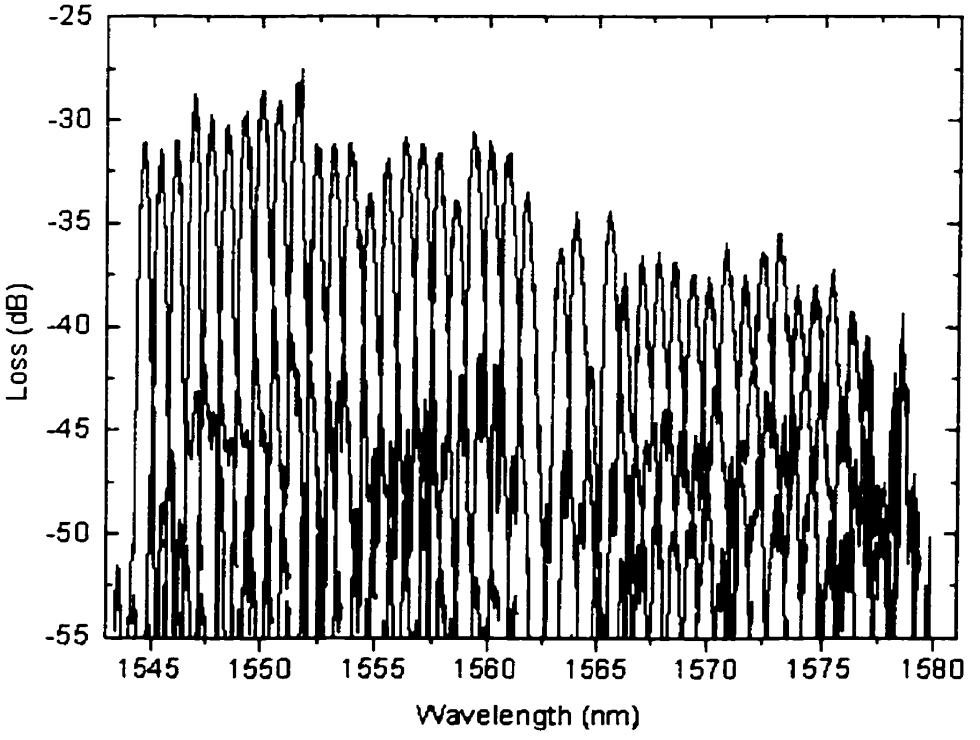

Figure 5.5 The full output channel spectrum of a Design B spectrometer.

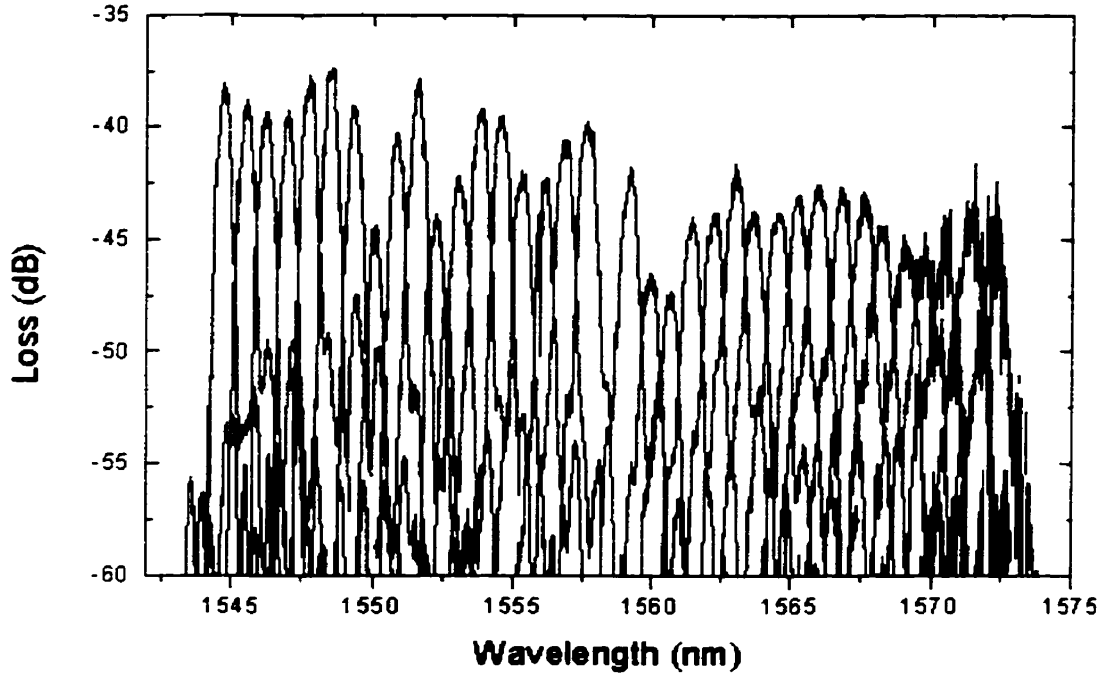

Figure 5.6 The full output spectrum of a second Design B spectrometer.

near the stigmatic wavelength as well and this must be explained by another mechanism. There is as much as a 15 dB (and as little as 6 dB) decrease in signal from the most efficient channels for wavelengths near 1530 nm. This increased loss is likely due to the increased length in the output ridge waveguides for wavelengths near 1530 nm. Design A also suffers from channel to channel variation of the collected signal. This is most likely due to ridge waveguide abnormalities and index matching liquid loss. The average peak to peak variation of the signal is 3 dB.

In Design B, the excess loss occurs at the high-wavelength end of the spectrum only, as shown in Figures 5.5 and 5.6. The high wavelength end of the spectrum is likely

affected by the defocusing loss, causing excess loss in the range of 7 dB to 10 dB from the most efficient channels. This design also shows some variation in the loss from channel to channel which averages a peak to peak change of 2 dB. In this design there is only a 1.8 mm increase in the length of the ridge waveguides from 1530 nm to 1570 nm. This design does not show any significant degradation in performance due to ridge waveguide loss.

Design C follows the same loss profile trend as Design B with excess loss of 5 dB occurring far from the stigmatic wavelength (λ_{stig} = 1576.8 nm), as shown in Figure 5.7. This design also shows greater fiber to fiber loss than the similar Design B (same channel spacing). While an additional 1.9 dB is expected due to difference in on-chip path length (slab propagation loss), Design C spectrometers showed over a 6 dB reduction in collected signal in the most efficient channels. Design C spectrometers had longer ridge waveguides (2.5 mm to 3.4 mm longer) therefore this is likely an indication of the loss

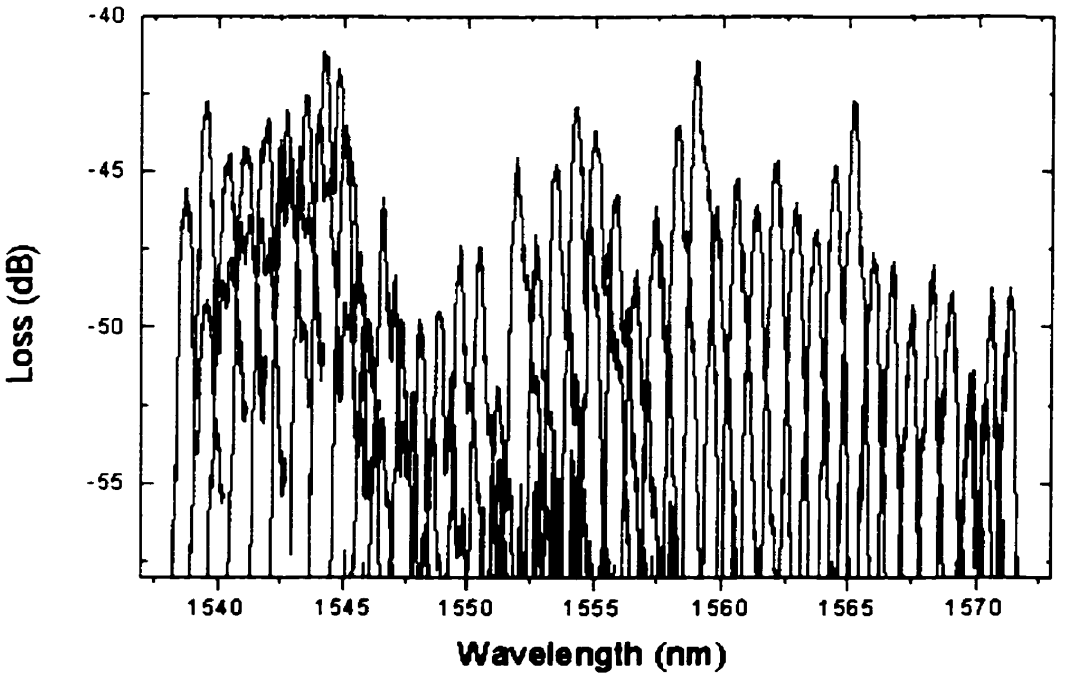

Figure 5.7 The full output spectrum of a Design C spectrometer.

incurred in the ridge waveguide propagation. For near 1545 nm (beyond the slab high absorption region) there is an increase of 7 dB loss for the Design C devices for an increase in ridge waveguide length of 2.5 mm. This shows that the ridge waveguides were probably very lossy.

Another possible contribution to the total on-chip loss is the change in the focal length of the mirror due a change in the index of refraction of the core layer. The index of the core layer cannot be controlled with absolute precision in the fabrication process therefore index variation is expected. Sun [20] found that the index of the core layer could vary by as much as 0.006 across a wafer during fabrication. The focal length of the mirror is given by

$$f = \frac{\mu\lambda_o \cos\beta\cos\theta}{(\sin\alpha + \sin\beta)} \cdot \frac{1}{n} \qquad 5.1$$

where μ is the linear dispersion along the output focal curve (user-defined), α is the incident angle at the grating, β is the diffraction angle for the wavelength λ_o, θ is a configuration parameter (see Figure 3.3) and n is the index of refraction of the core layer. This equation was arrived at by combining Equations 3.1 and 3.4. This implies that if the actual index of the core layer is larger than the design parameter, the focal length of the mirror will be shorter than the design equations predict. A change in focal length, either shorter or longer, would cause the output spot to be defocused at the collector waveguides. As discussed previously, defocusing causes incomplete collection of the output spot and therefore an increase in loss per channel. A change in the focal length of the mirror would tend to increase the loss in all spectrometer channels. The results of Sun suggest that the focal length could vary by 0.4% due to index variations.

5.5 BIREFRINGENCE AND POLARIZATION DEPENDENT LOSS

The performance of the spectrometers is not only dependent on the wavelength of the input signal, it is also dependent on the polarization of the light within the waveguide. All measurements were made with TM polarized light (with respect to the slab) previously but it is important to know the performance of the device with TE polarization as well. Even if the light initially injected into the fiber is of only one polarization, light that emerges from an optical fiber in a telecommunications system will consist of both TE and TM polarizations due to mode mixing within the fiber. If the demultiplexer's performance is polarization dependent, in terms of the loss or dispersion, the resultant channel output will be dependent on the degree of mode mixing and thus on the length of fiber between demultiplexers.

One of the polarization dependent effects in waveguide layers is birefringence. The resultant behaviour due to birefringence in the spectrometers investigated here is a shift in center wavelength of a given output channel's peak signal for the TE and TM mode. This phenomenon is also referred to as polarization dependent dispersion (PDD). The total birefringence, B, in a waveguide is caused by stress birefringence and waveguide birefringence. The total birefringence in the slab waveguide is calculated by considering the path length of the TE and TM modes upon reflection from the grating. The waveguide design wavelength and the wavelengths of the TE and TM modes (for any given channel) travel an extra distance in diffraction from the grating given by

$$\Delta L = m\frac{\lambda_o}{N_o} = m\frac{\lambda_{TE}}{N_{TE}} = m\frac{\lambda_{TM}}{N_{TM}} \qquad 5.2$$

where m is the grating order (m=16 in this work), N_o is the effective index of the core layer for the design wavelength (1.484), N_{TE} and N_{TE} are the effective indices of the TE and TM modes respectively, λ_o is the wavelength used to design the layers (1550.0 nm) and λ_i is the wavelength of the light for each of the cases listed. Using Equation 5.1, the shift in wavelength due to the total birefringence is

$$\Delta\lambda = \lambda_{TE} - \lambda_{TM} = \frac{\Delta L}{m}(N_{TE} - N_{TM}) \qquad 5.3$$

and the total birefringence, B, is defined as

$$B = \frac{N\Delta\lambda}{\lambda_o} \qquad 5.4$$

In the devices considered in this work, the shift in wavelength for the TE and TM modes (for Designs B and C) was measured for several channels in each device. The average shift was 0.9 nm in the measured devices. This corresponds to a total birefringence of $8.62\text{x}10^{-4}$.

Stress birefringence is defined by

$$B_{stress} = KE(\alpha_{substrate} - \alpha_{cladding})\Delta T \qquad 5.5$$

where N_i are the effective indices of refraction for the TE and TM modes, K is the photoelastic coefficient and E is Young's modulus of SiO_2, α_i are the thermal expansion coefficients of the substrate and the cladding and ΔT is the difference between the glass consolidation temperature and room temperature [7]. A typical value for the stress birefringence for a Si substrate and the SiO_2 cladding layer is $-2\text{x}10^{-4}$. Waveguide birefringence is caused by the difference in the index of refraction of the core and cladding layers. The total birefringence in the SiO_2/SiON layers used in this project is

dominated by waveguide birefringence in the slab waveguide ($B_{waveguide} \approx -3B_{stress}$). The polarization dependent dispersion for designs B and C are shown in Figures 5.8 and 5.9. For all devices tested, the polarization dependent shift was very similar, showing that the polarization dependent feature of the spectrometer is the slab waveguide. The birefringence of the layers can be reduced and possibly eliminated by introducing another layer to the waveguide layer structure. This high index layer changes the index profile of the slab waveguide and therefore changes the propagation constant of both TE and TM modes. This technique was developed by Aarnio et al. [24] and theoretical calculations to determine the thickness of the high index layer were made by Sun [20].

In Figures 5.8 and 5.9, it is also possible to see that there is polarization dependent loss (PDL). The largest difference in the TE and TM peak heights is usually defined to be the PDL. The spectrometers exhibit PDL because of the difference in the reflectance for the TE and TM modes while travelling within the slab waveguide as well from the air-waveguide boundary at the mirror and the grating facets (for any incident angle other than normal incidence).

The reflectance for both TE and TM polarization plane waves incident on the retro-reflecting facets was calculated by Sadov and McGreer [47]. Sadov and McGreer used the boundary integral method to determine the diffraction efficiencies of both TE and TM polarized light. The calculations are relevant to plane waves incident on a bulk grating with retro-reflecting facets. The diffraction of a guided mode will differ from that of a plane wave but it is interesting to compare these results. Sadov and McGreer found that, for a grating of 16^{th} order, the integral method predicts a PDL of 3.5 dB. In this

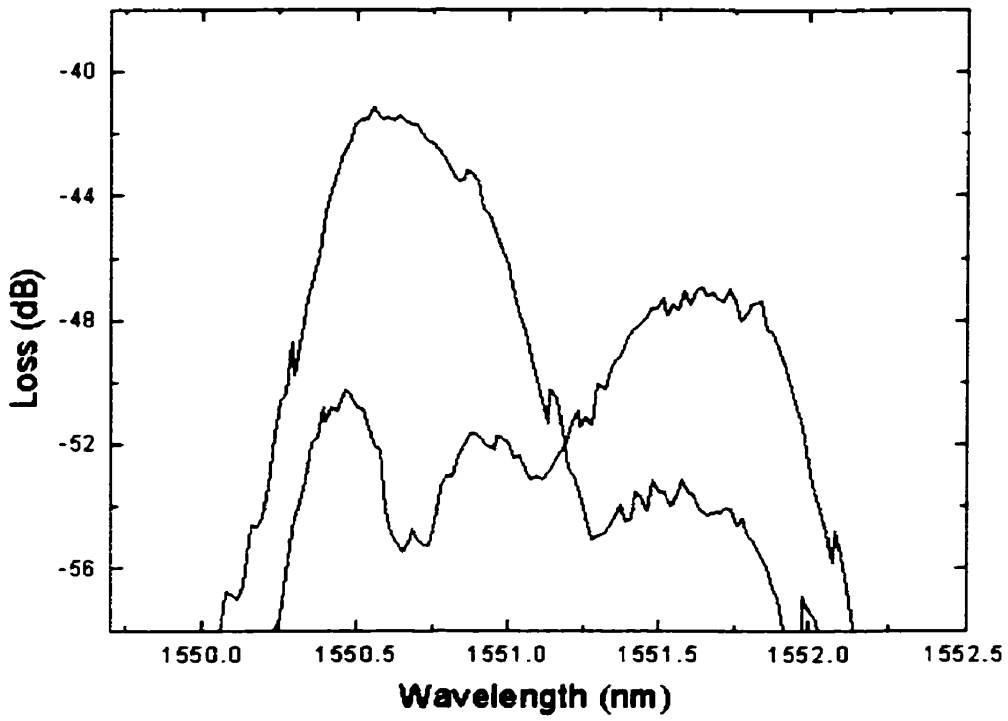

Figure 5.8 The wavelength shift between the TE (right) and TM (left) modes for one output channel on a Design B spectrometer.

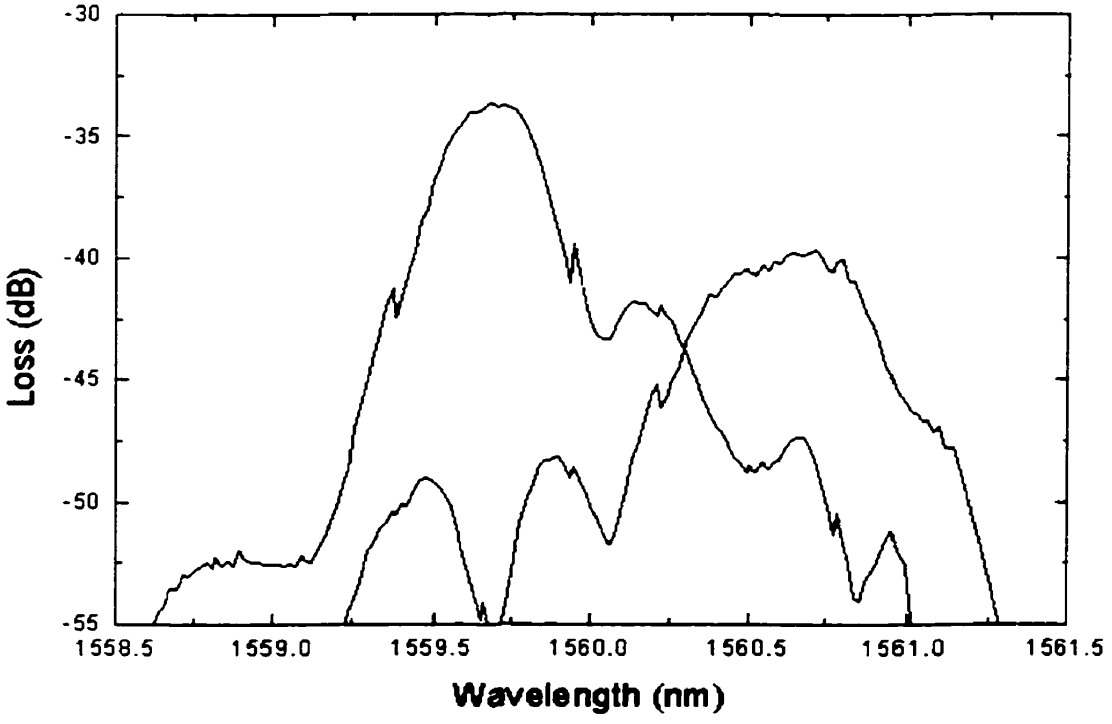

Figure 5.9 The wavelength shift between the TE (right) and TM (left) modes for one output channel on a Design C spectrometer.

work, the PDL was measured for every second output channel in Designs B and C. The average height difference between the TE and TM peaks, the PDL, is 3.2 dB and the standard deviation is 0.9 dB on one of the wafers. This value agrees well with theory. On another wafer, the PDL was measured to be 5.6 ± 0.9 dB. The device with high PDL also showed higher on-chip loss. This suggests that there may have been damage to the slab waveguide. Experimentally, the TE mode has higher loss than the TM mode. This PDL is much too high for most commercial applications; an industry acceptable level is 0.1 dB variation. Sadov and McGreer showed that using materials with higher indices of refraction reduced the PDL and increased the efficiency [47]. When the index of refraction was increased from 1.5 to 3.2, the efficiency of the TE mode was increased by 2.5 dB and PDL was reduced from 3.5 dB to 0.5 dB.

5.6 CHANNEL WAVELENGTH SHIFT DUE TO CHOICE OF INPUT WAVEGUIDE

To allow for possible errors in fabrication, several input waveguides were etched. Errors in fabrication may include a change in the index of refraction from that assumed in the design process, a damaged input waveguide or an incomplete etch of one of the input waveguides. By using a different input waveguide, the angle of incidence of the input signal changes, causing the output diffraction distribution to shift spatially. The passband for a given output channel will therefore change with the choice of input waveguide. A change in the index of refraction of the slab waveguide can then be compensated by

switching to the most appropriate waveguide so that a given output waveguide may still correspond to a chosen wavelength (or at least closer to the chosen designed wavelength).

For Design B, the shift in the passband in one output channel was characterized for a few different input waveguides. A plot of the shift in passband for one output waveguide is shown in Figure 5.10. The average shift in the collected output wavelength was 1.53 ± 0.02 nm. This corresponds to a diffraction pattern shift corresponding to approximately 2 output channels (spaced at 0.8 nm for this design). The linear dispersion along the output focal plane of the mirror was designed to be 8 mm of spatial shift per nanometer in wavelength. This corresponds to the output waveguides (for 0.8 nm channels) being separated by roughly 10 μm. If the input waveguide is changed and the input spot moves over 21 μm (the separation of the input waveguides) one would expect

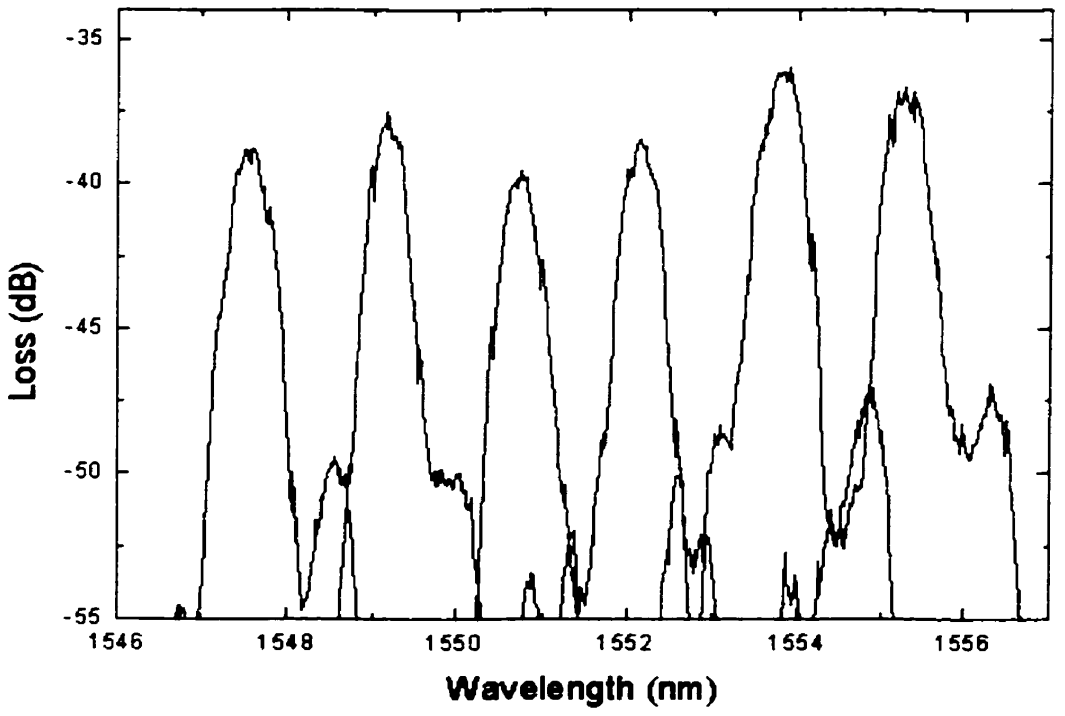

Figure 5.10 The shift in collected wavelength for one output channel as the input waveguide was changed on a Design B device. The average shift caused by changing the input waveguide was 1.53 ± 0.02 nm.

the output to shift by a proportionate amount. This assumes linearity in the response of the mirror with a change in the position of the input spot. The change in position of the input spot corresponds to a shift in wavelength of 1.6 nm. This is not within error of the value measured but it is sufficiently close that it validates the measured wavelength shift with the change in input waveguide used.

5.7 CHANNEL ISOLATION

Channel isolation is one of the key specifications for a demultiplexer in a WDM system. The isolation is generally required to be at least -30 dB between adjacent channels to allow for confident and reliable signal detection. The channel isolation of these spectrometers does not meet industry standards. Figures 5.11 through 5.13 show the typical cross-talk of adjacent channels for each of the three designs (designs A, B and C respectively).

According to diffraction theory, the intensity profile created in the far-field for a diffraction grating should have a regular periodicity with a period equal to the free spectral range (see Section 2.1). The free spectral range of the gratings with Designs A and B (given by Equation 2.9) is 95.4 nm. For Design C, the free spectral range is 98.6 nm. This means that the adjacent maxima are spaced 95.4 nm (or 98.6 nm) from the 16^{th} order (the retro-reflected order) and none of the WDM channels will be affected by cross-talk from adjacent orders. The performance of the grating spectrometer is dependent on the resolving power (and resolution) of the grating. The calculated resolution (from Equation 2.7) for the three designs are shown in Table 5.1. The theoretical resolution of

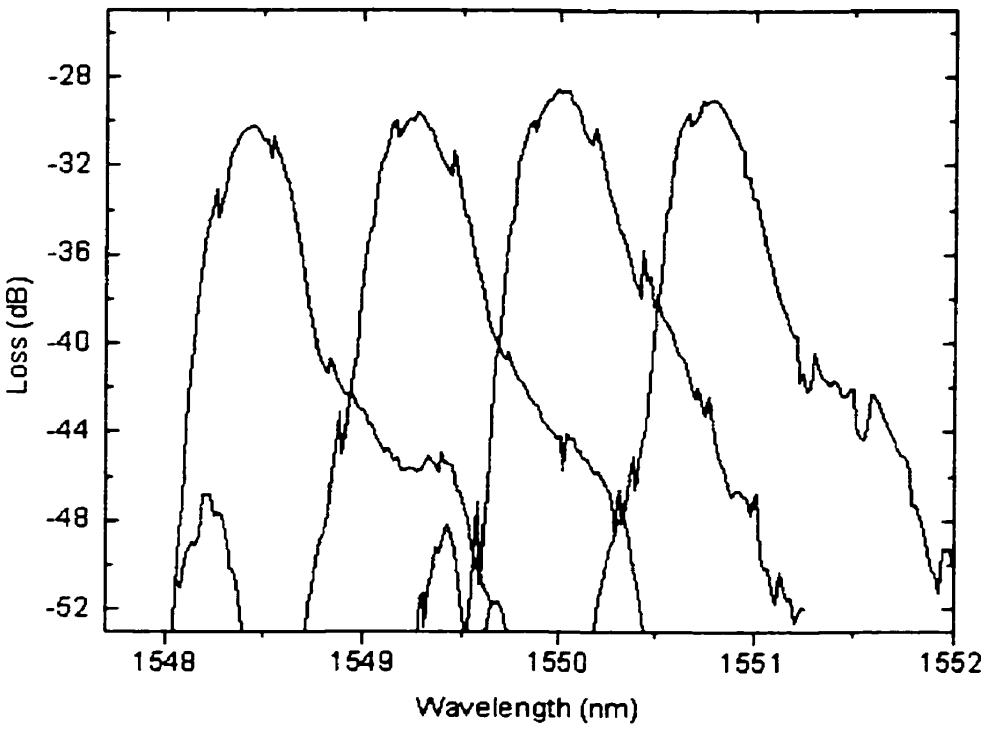

Figure 5.11 Four adjacent channels for a Design A spectrometer.

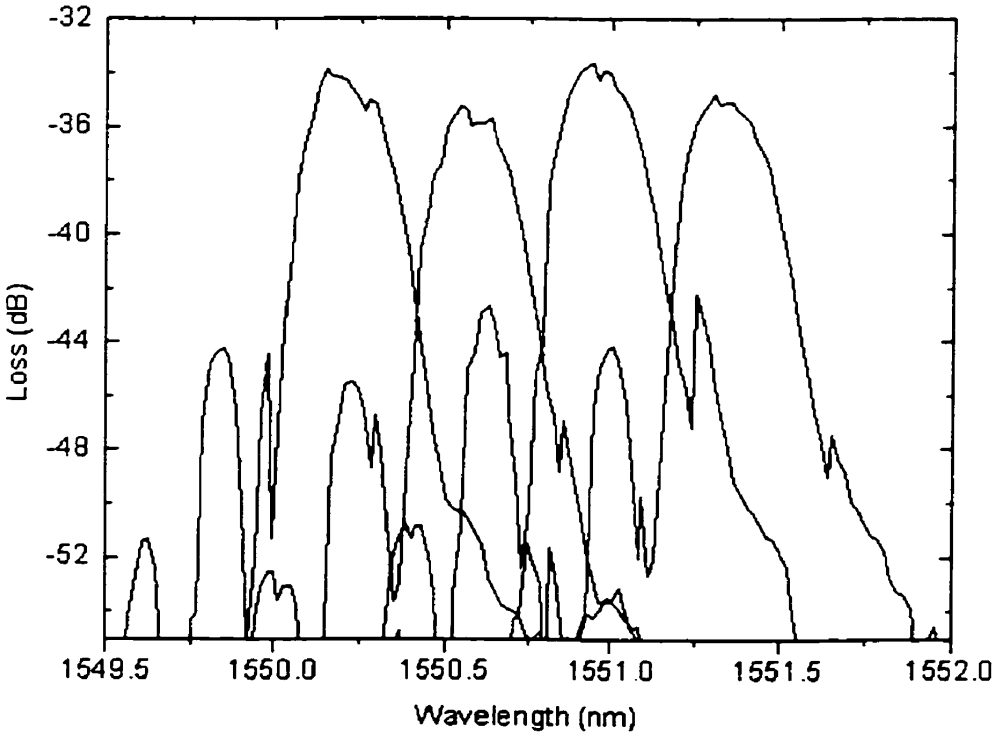

Figure 5.12 Four adjacent channels for a Design B spectrometer.

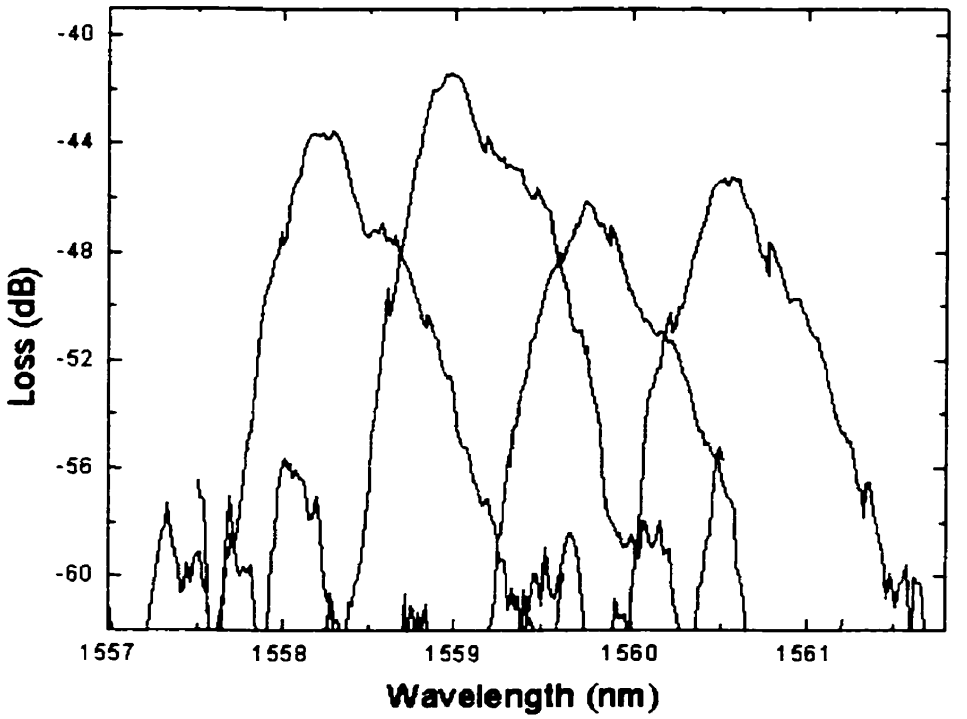

Figure 5.13 Four adjacent channels for a Design C spectrometer.

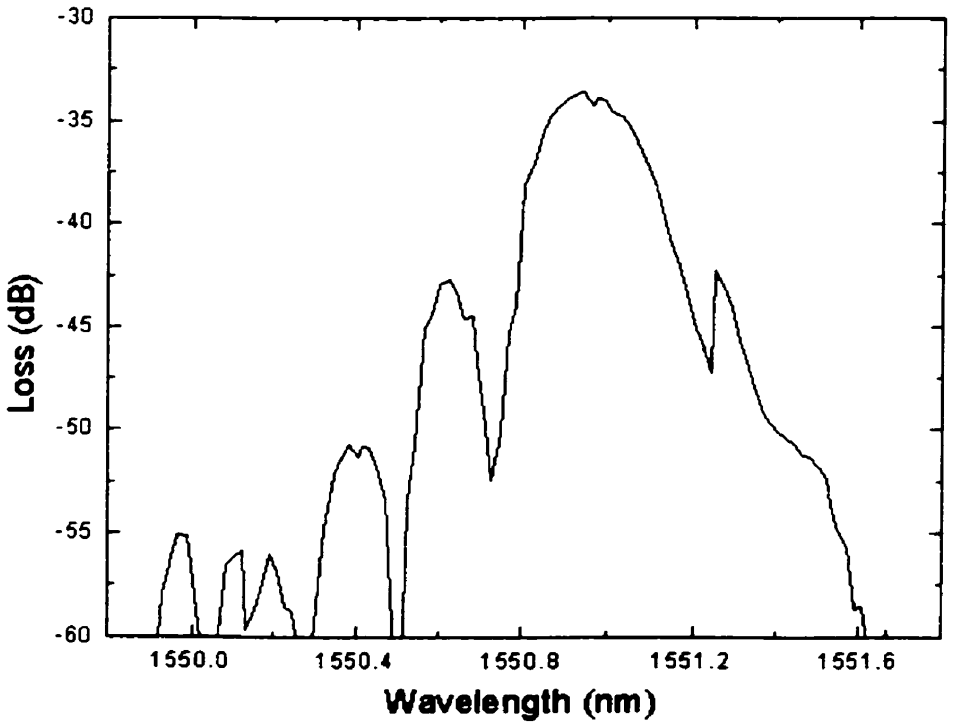

Figure 5.14 Single channel spectrum for a Design A spectrometer. The side lobes on the left are unique to this design.

design A (0.16 nm) is 2.5 times smaller than the 0.4 nm design channel spacing. It is expected that there will be minimal cross-talk due to the overlap of adjacent peaks.

For design A, interesting features have appeared in the channel spectra that occur for all channels (to varying degrees). Each channel spectrum (shown in Figure 5.14) has side lobes on the low wavelength side of the channel maximum. This asymmetric lobe structure is quite unusual and is not predicted by the diffraction theory given in Section 2.1. The first minor maximum occurs with regularity at 0.4 nm from the central maximum and the second occurs at 0.6 nm from the central maximum. It is interesting to note that neither design B nor C suffer from the asymmetric lobe cross-talk (as shown in Figures 5.15 and 5.16).

Another candidate for the source of the side lobes is radiative leaking from adjacent output channel waveguides. However, for design A radiative leaking is not a possibility on the low wavelength side of the main peak due to non-confinement along the curved section of the waveguide. Figure 5.17 shows the mechanism for radiative leaking in the curved waveguide sections. For the physical layout of designs A and B spectrometers, leaking radiation on the curved waveguide sections should come from higher wavelengths (waveguides on the inner edge of any given channel). For two devices tested with design A, one was scanned from 1530 nm to 1570 nm while the other was scanned in the opposite direction and both devices showed the same side lobe structure. This indicates that the side lobes are not likely due to systematic error or due to index matching fluid causing preferential, direction-dependent waveguide leakage. The source of the side lobes must be an aberration that is design-dependent, though it is not clear what type of aberration is causing the side lobes.

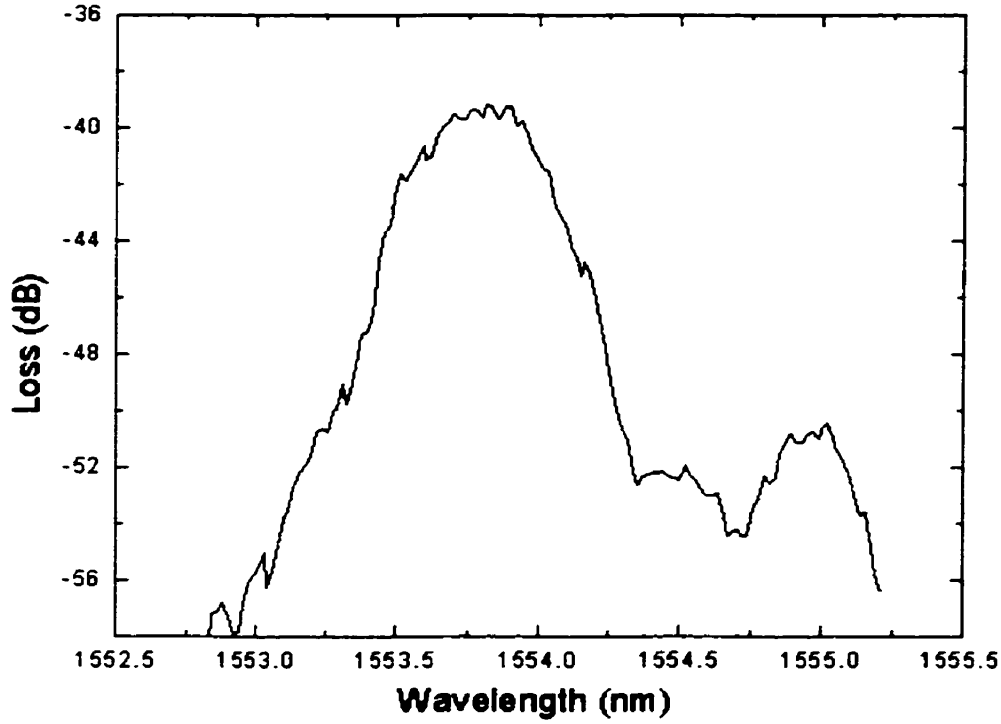

Figure 5.15 Single channel spectrum for a Design B spectrometer.

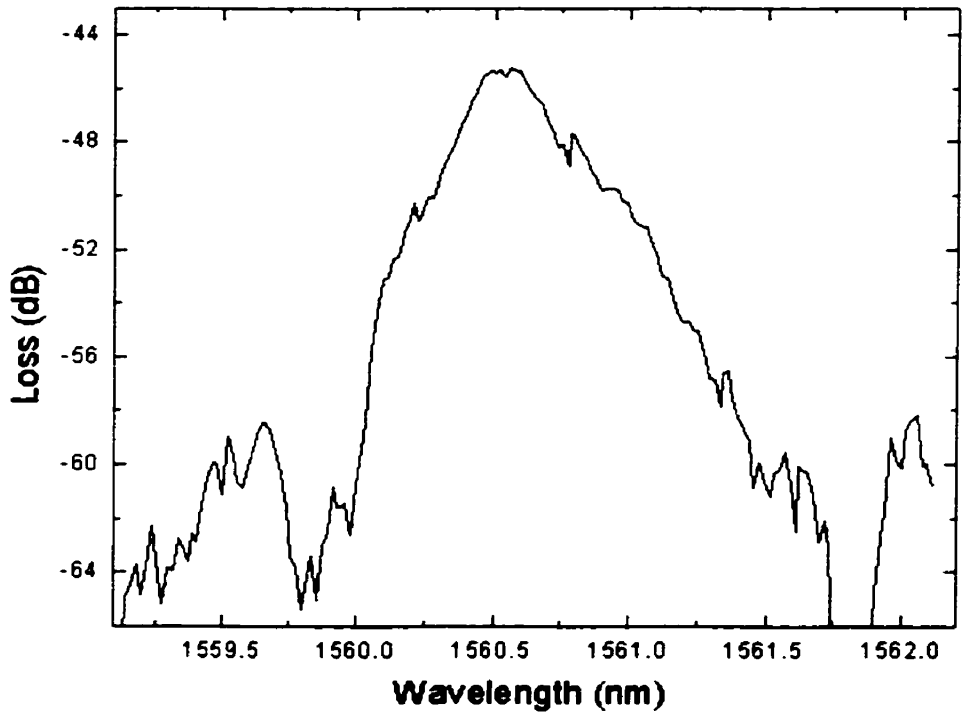

Figure 5.16 Single channel spectrum for a Design C spectrometer.

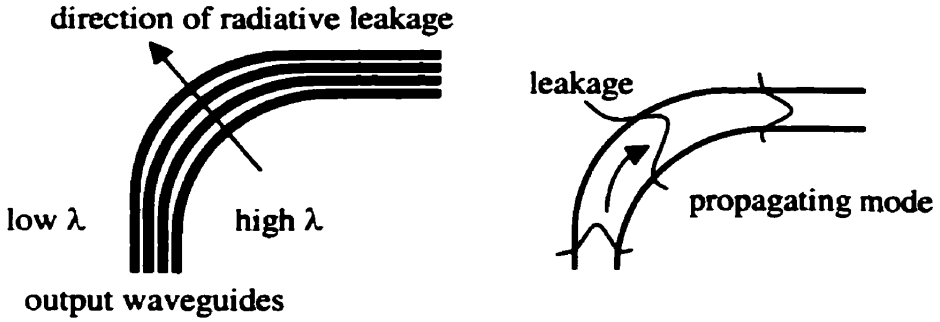

Figure 5.17 For Design A and B spectrometers, radiative leakage occurs such that some of the light from high λ output waveguides passes through to lower λ output waveguides. For Design C spectrometers, the phenomenon is reversed.

Two of the design A spectrometers, after characterization, were sent back to Alberta Microelectronic Corp. to have the input and output ridge waveguides separated from the mirrors and gratings. With the waveguides removed, the output spot of the spectrometer was larger as the light was neither injected nor collected on the focal plane any longer. The total loss in passing through the spectrometer was increased due to the defocused output spot (the output collection fiber no longer collected all of the light). The edge of the spectrometer was left visibly rough from the wafer saw cut. The roughness also contributed to the fiber to fiber loss. A representative spectrum from these tests is shown in Figure 5.18a. Figure 5.18c shows a comparison of the channel measured with the waveguides in place for comparison to Figure 5.18a. The central peak (at 1540.54 nm) with the waveguides in place (Figure 5.18c) has side lobes 0.47 and 0.48 away from the central peak (10 dB down) and has a full-width half maximum (FWHM) of 0.56 nm. With the waveguides removed, the FWHM is reduced to 0.3 nm. The cross-talk due to the adjacent channels leaking into the spectrum (at 0.4 nm on either side of the central peak) has vanished. It is clear that the closest side lobes visible in Figure 5.18c

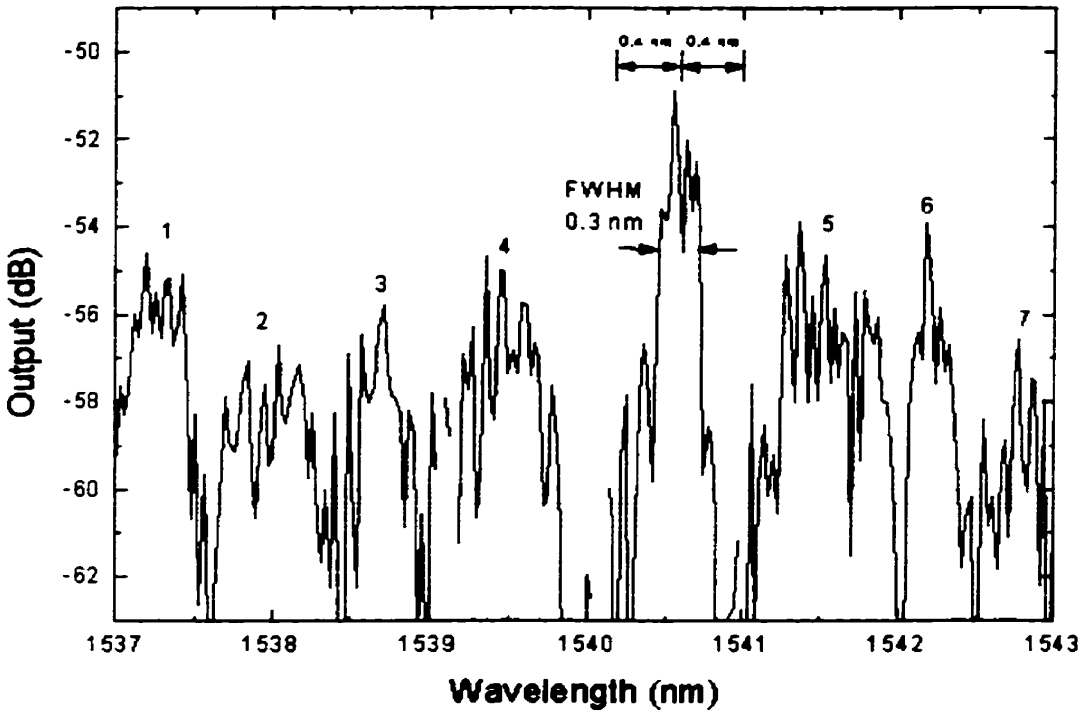

Figure 5.18a Extended spectrum for a Design A (0.4 nm spacing) spectrometer with the input and output ridge waveguides removed. The central peak, at 1540.54 nm, has a FWHM of 0.3 nm.

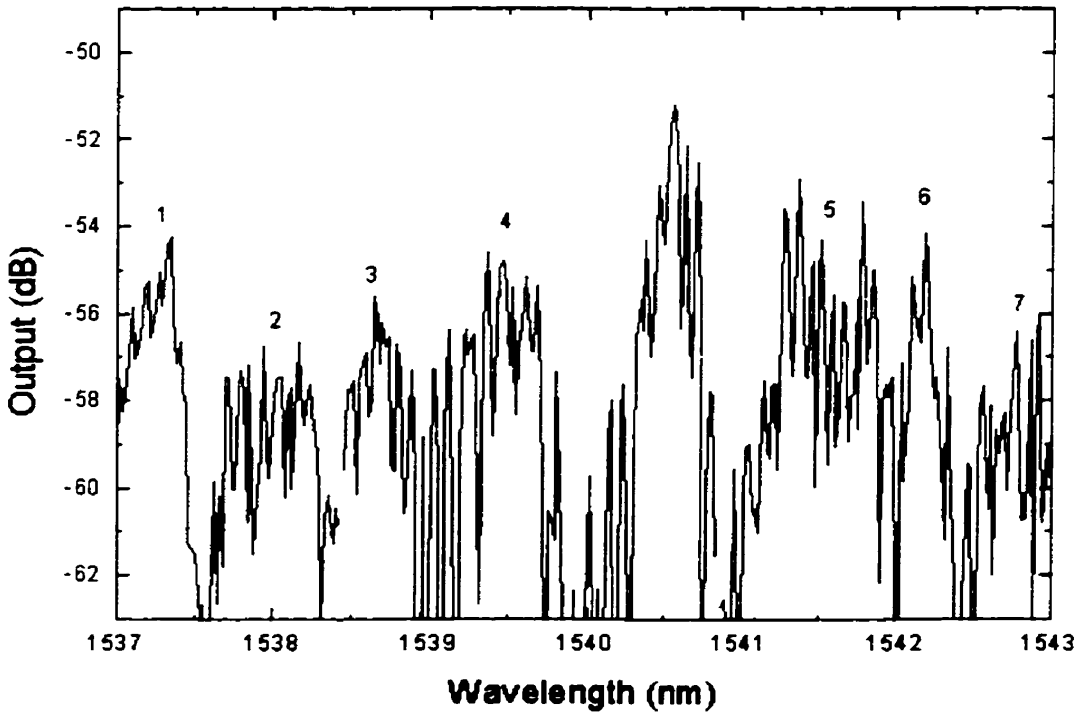

Figure 5.18b This shows the repeatability of the features seen in Figure 5.18a. Each of the features occurs at precisely the same wavelength for both scans.

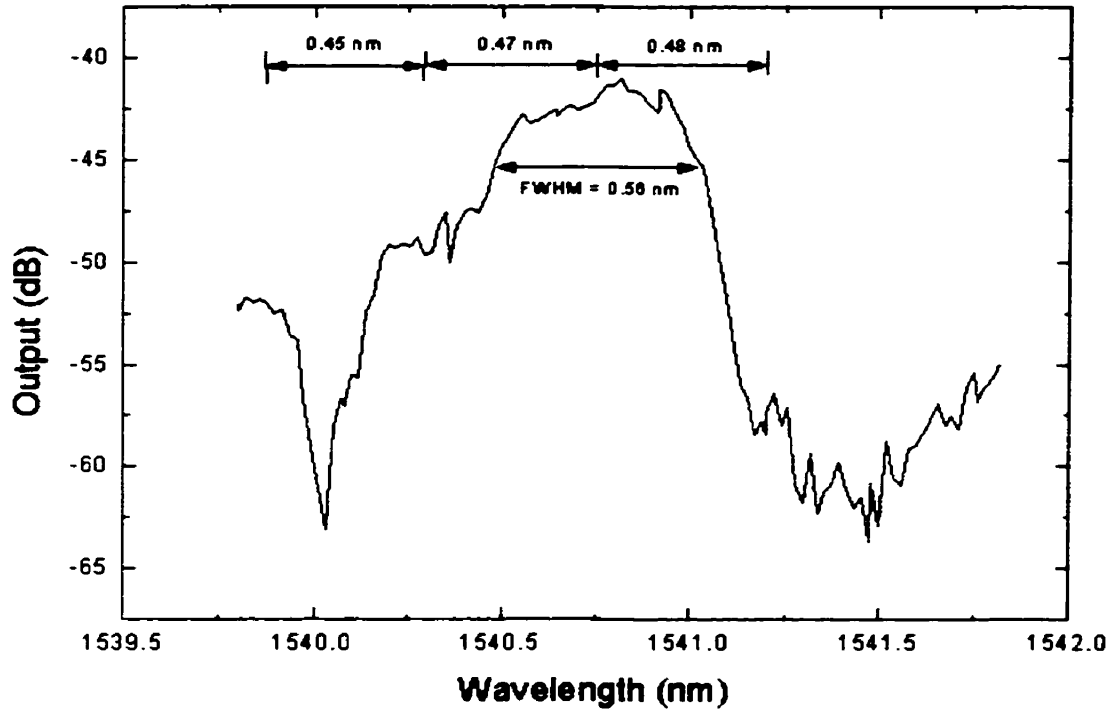

Figure 5.18c The output spectra for a channel at 1540.54nm with output waveguides in place. The FWHM is 0.56 nm, 0.26 nm wider than when the waveguides were removed. The adjacent channels coincide with side lobe positions.

are due to the waveguide leakage because these peaks do not appear in the spectrum of the spectrometer with the waveguides removed.

There are additional features visible in the background of the plot in Figure 5.18a. The numbered features in the background are repeatable and are quite likely due to photomask pixelation. In a recent paper by He et al. [25], a concave demultiplexer was designed and tested with retro-reflecting grating facets. These researchers found that there existed unusual long-range features in the spectra of their demultiplexer channels and they determined that the lobes were artifacts of the fabrication process. One of the problems identified was pixelation of the mask design due to the photomask fabrication process. The grating features could have been subjected to round-off error in the

mechanical positioning of an electron or focused ion beam used in writing the mask. These types of problems with photomask writing seem to show large scale periodicity (on the order of 4 nm repetition) in the channel spectra for their devices and their fabrication process.

In Figure 5.18b, the repeatability of the long-range features is clear when compared to Figure 5.18a. The data shown in these graphs were collected using the same input and output fiber positions. There is a similarity in the structure of the lobes between the data collected here and the data collected by He. The numbered features have an average separation of 0.67 ± 0.08 nm for peak separations in Figures 5.18a and b. According to He, the distance between the peaks is directly related to the size of the area covered by the e-beam writer during fabrication of the photomask;

$$\Delta\lambda = \frac{FSR \times d}{S} \qquad 5.6$$

where the *FSR* is the free spectral range, *d* is the grating period (10.7 μm here) and S is the length traveled by the e-beam writer before shifting to the next writing area. For the parameters in this work, Equation 5.5 gives S = 1.01 mm.

For design B, the 0.8 nm spaced channels showed an average channel isolation of 12 dB, ranging from 15 dB at the low wavelength end of the spectrum to 10 dB at the high wavelength end of the spectrum. For design C, the average channel isolation was found to be 14 dB, ranging from 13 dB at the high wavelength end of the spectrum to 15 dB at the low wavelength end of the spectrum. Figures 5.11 through 5.13 show the channel isolation as a function of output channel wavelength for each of the three designs. The data plotted are a sample of all output channels. As a trend, each design showed

reduced channel isolation as the central channel wavelength moves away from the stigmatic wavelength. The spectrometer's channel isolation is not sufficient for it to become useful as a commercial WDM demultiplexer.

As discussed in Section 5.4.2, defocusing of the output spot due to non-uniform focusing by the mirror (affects channels far from the stigmatic wavelength) is expected to increase the cross-talk measured at each channel. Figures 5.2 through 5.6, the full output spectra for all spectrometer designs show a reduction in channel isolation consistent with non-uniform mirror focusing. In Section 5.4.4 an inaccuracy in the refractive index from the design index was shown to change the focal length of the mirror. It is expected that either an increase or a decrease in the index would increase the cross-talk in all channels.

One further consideration for the channel isolation is the cross-talk caused by a shift in the focussed output spot due to total internal reflection at the mirror. At the mirror, there is a range of incident angles for the incident Gaussian beam because of the shallow angle at which the light strikes the concave mirror. The light has an incident angle that ranges from 45° to 60° across the mirror. The difference in incident angle creates a difference in the phase shift acquired along the length of the mirror for both TE and TM polarizations. The induced phase shift, ρ, due to total internal reflection is given by

$$\tan\frac{\rho_{TE}}{2} = \frac{\sqrt{\left(\sin^2\theta_i - \sin^2\theta_c\right)}}{\cos\theta_i}$$
$$\tan\frac{\rho_{TM}}{2} = \frac{\sqrt{\left(\sin^2\theta_i - \sin^2\theta_c\right)}}{\sin^2\theta_c\cos\theta_i} \qquad 5.7$$

where θ_i is the angle of incidence and θ_c is the critical angle for that interface. For the air-waveguide interface in the spectrometers, the phase shift for the TE polarization ranges from 32.3° to 94.4° (θ_i = 45° and 60° respectively). In the case of TM polarization, the phase shift ranges from 64.5° to 134.0° (θ_i = 45° and 60° respectively). The reflection-induced phase increases across the mirror. The phase front of the reflected light is skewed slightly by this additional phase therefore the phase front that strikes the grating is not incident on the grating in the original, designed direction. The effect of this additional phase shift on the performance of the spectrometer is quantified below.

The difference in phase shift due to reflection at the mirror is 62.1° for TE polarization and is 69.5° for TM polarization. This corresponds to an effective change in path length of

$$\Delta z = \frac{\Delta\rho\lambda}{2\pi n_g} \tag{5.8}$$

where $\Delta\rho$ is the phase difference between light reflected at either end of the mirror, λ is the wavelength of the light in free space and n_g is the slab effective index. For the TE mode, the path length is increased by 0.18μm and for the TM mode it is increased by 0.20 μm.

For the Design A spectrometers (0.4 nm channel spacing), the spot size at the mirror is 3.44 mm wide. The angle of the phase front is changed slightly by the added path length Δz to once end of the beam. The effective incident angle of the light on the grating as reflected from the mirror with consideration for the new added path length is

$$\tan\delta = \frac{\Delta z}{(\text{spot width})} \tag{5.9}$$

For the Design A spectrometers, the angle δ is 0.003°. If this correction to the incident angle is inserted into the grating equation, the corresponding new diffraction angle is 45.0033°; a difference of 0.0033° from the original design angle. This shift in the diffracted angle can be related to the output dispersion. The grating equation can be used once more to determine how this angular shift will affect the output spectrum. Assuming that the light is incident on the grating at the original design angle but with a new diffracted angle, the corresponding wavelength associated with the new diffracted angle is

$$\lambda_{new} = \frac{dn_g(\sin\alpha + \sin(\beta + \delta\beta))}{m'} \qquad 5.10$$

which gives a diffracted wavelength of 1.526039 μm. This differs from the stigmatic wavelength by 0.04 nm. The output linear dispersion is 25 μm/nm therefore the output spot has moved by 1.11 μm (TM) and 0.99μm (TE) in the Design A spectrometers. Similar calculations arrive at a shift of 0.899μm (TM) and 0.810 μm (TE) in the Design B spectrometers. These shifts represent a shift that is 25% of the width of the output waveguides. The adjacent waveguides will tend to collect some of the light intended for its neighbour and therefore cross-talk is increased and loss is incurred. This effect decreases the incident angle on the grating, which in turn increases the diffraction angle. This suggests that there will be higher side lobes on the high wavelength side of the main maximum and that Design A spectrometers will be affected slightly more than Design B and C spectrometers. This is effect can be seen in Figures 5.14 through 5.16, though the effect is not very strong. The total internal reflection affects the TE and the TM polarizations similarly; therefore, it is unlikely that any polarization dependent performance will be created by this effect.

The channel isolation could have been improved by increasing the linear dispersion along the output focal plane. Physically, this corresponds to placing the output waveguides on wider centers. The use of greater waveguide separation should improve the cross-talk due to decreased spectral overlap of the focused output spots. In addition, it would decrease the amount of radiation leakage in the curved sections of the output waveguides. The draw back to this approach is that the spectrometer design would increase in size. Larger waveguide separation requires a longer distance from the mirror to spatially separate the channel output spots along the output focal plane (given a known angular separation of the channel wavelengths).

One further figure of merit that can be measured in Figures 5.11 through 5.13 is the flatness of the peaks across the DWDM channel. This is designated the 0.5 dB bandwidth. The width of the peak (in wavelength) is measured where the signal is greater than 0.5 dB down from the maximum signal. For these devices, the 0.5 dB bandwidth is 0.13 nm for Design A and 0.18 nm for both Designs B and C. These are reasonable results for 0.4 nm and 0.8 nm channel spacing devices as interference filter demultiplexers (at 0.8 nm spacing) show 0.5 dB bandwidths on the order of 0.22 nm.

5.8 CHANNEL CENTER WAVELENGTH

All three spectrometer designs showed good consistency in the channel center wavelength spacing. Figures 5.19 through 5.21 show the linearity of the increase in the channel center wavelength. The average measured channel spacing for each of the three designs

are shown in Table 5.2. The measured values do not agree with the expected values within error. The average channel spacing has been skewed from the designed value because the average channel spacing was measured by finding the slope of the plots shown in Figures 5.19 through 5.21. In each of these plots there are small shifts in the data, making the data piecewise linear. To show the change in the average spacing, the average spacing was measured over each of the piecewise linear sections, resulting in different values for the average channel spacing. These values are also shown in Table 5.2. The shifts in the data are likely caused by a small change in position of the input fiber when adjustments were made to maintain maximum output signal. The frequency of the shifts is consistent with the frequency of input fiber adjustments. The shift in output wavelength with minor changes in input fiber position may have been caused by excitation of other modes (more than the fundamental mode) in the input waveguide. At the end of the waveguide, the image spot that propagates through the spectrometer will not coincide with the image of the fundamental mode but a combination of the fundamental mode with higher order modes. The position of the peak intensity would have shifted due to this effect and therefore the effective position of the input waveguide.

One major concern about the performance of the spectrometers investigated in this work was the distinct shift in the center wavelength collected by the output waveguides from their designed center wavelengths. The design parameters defined the outermost waveguides of all spectrometer designs to collect 1528.4 nm and 1571.6 nm. It is clear from Figures 5.2 through 5.7 that the collected spectrum is shifted from the design parameters. For design B devices, the shift is very significant, with the shift of 12.3 nm. While characterizing the Design C device, it was observed (through the microscope) that

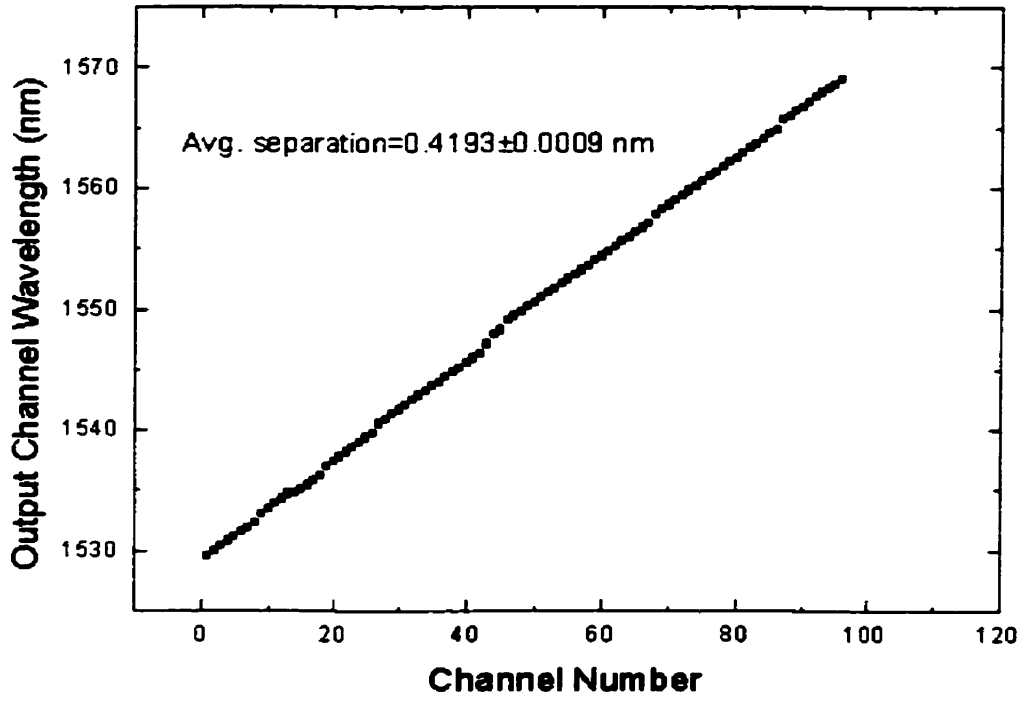

Figure 5.19 Output channel center wavelengths for a Design A spectrometer. The average channel spacing over all channels is 0.4193 ± 0.0009 nm.

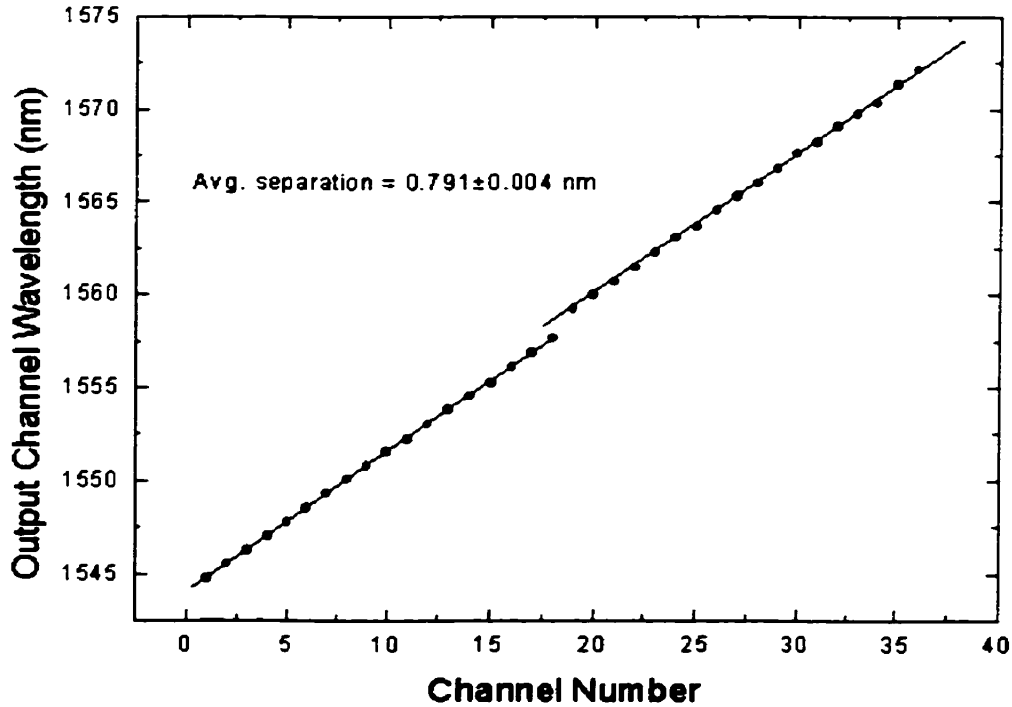

Figure 5.20 Output channel center wavelengths for a Design B spectrometer. The average channel spacing over all channels was 0.791 ± 0.004 nm.

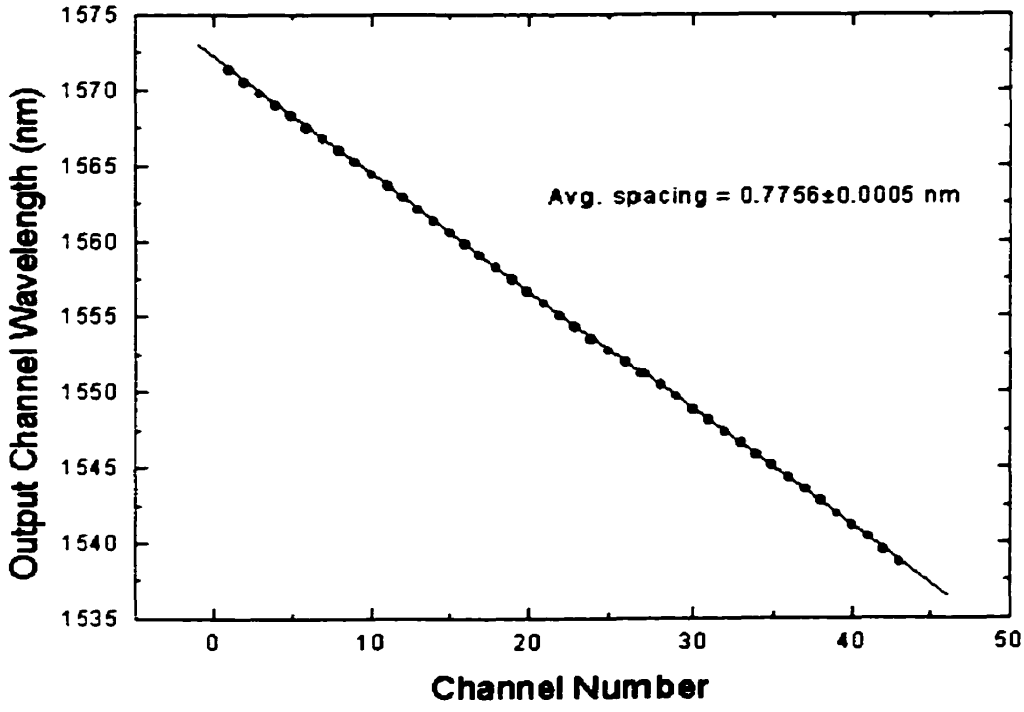

Figure 5.21 Output channel center wavelengths for a Design C spectrometer. The average channel spacing over all channels was 0.7756 ± 0.0005 nm.

a couple of the input waveguides were damaged. The center waveguide was not used therefore, some shift is expected in these measurements. The most obvious reason for the shift in the starting wavelength is that the center waveguide was not used. As discussed previously, using a different input waveguide from the designed center input waveguide will tend to shift the output spectrum by an amount roughly equal to twice the output channel spacing, $\Delta\lambda$. However, none of the devices show a shift equal to a multiple of $2\Delta\lambda$.

Spectrometer Design	A	B	C
Designed Channel Spacing (nm)	0.4	0.8	0.8
Average Measured Channel Spacing (nm)	0.4193 ± 0.009	0.791 ± 0.004	0.7756 ± 0.0005
Piecewise Average Channel Spacing (nm)	0.39 ± 0.01	0.756 ± 0.001	0.776 ± 0.001
First Channel Shift from Design	1.2 nm	12.3 nm	0.3 nm

Table 5.2 The average measured channel spacing compared to the designed spacing

Another possible effect on the absolute wavelength collected by a given output waveguide is the index of refraction of the slab. According to the grating equation (Equation 2.1) the diffraction angle depends upon the wavelength of the light in the core medium. If the index of refraction is increased, the wavelength in the medium decreases. Using the equation for the linear dispersion along the focal curve of the mirror and the grating equation (Equations 3.4 and 2.1 respectively), the linear dispersion can be expressed as a function of the index of the core layer.

$$\mu = \frac{(\sin\alpha + \sin\beta_{stig})f}{\lambda_{stig}\cos\theta\cos\beta_{stig}} \cdot n \qquad 5.6$$

The measured linear dispersion shows an average deviation of 3% from the designed dispersion. If the mask design was done correctly, all other parameters are fixed and therefore the changes in linear dispersion can come only from the index. A three percent difference in the core index corresponds to a change of 0.04. This is a very significant

change in index therefore this is likely not the only contribution to the unexpected deviation in the channel spacing.

5.9 COMPARISON WITH OTHER GRATING DEMULTIPLEXERS

In the literature, there are many versions of the integrated grating demultiplexers. The majority of the work has been based on the Rowland circle [26] and recursively defined concave gratings [8,11]. One of the motivations of this work was to see how a linear grating (with independent focusing elements) would perform compared to the more popular concave grating. In this section, the planar grating designed in this work will be compared to some of the most recent results found for concave gratings.

The six papers that have the most relevant results for grating spectrometers are written by Z. Sun et al [12,15], J.-J. He et al. [25], P.C. Clemens et al [10], C. Cremer et al [13], and K. Liu et al [14]. These results are a good representative group for this technology. Table 5.3 shows some of the benchmarks that are used to compare demultiplexers and how these six similar designs compare to those in this work. All of the devices in this group are integrated concave gratings (with the exception of the spectrometer designed in this thesis).

The first five spectrometers listed in Table 5.3 have the retro-reflecting grating facets while the remainder of the gratings in the list have flat facets. In He [25], it is quoted that the use of the retro-reflecting facets increases the grating efficiency by 4 dB from the conventional flat grating facets. It is clear that the on-chip loss is high compared

Author	Channel Spacing (nm)	Layer Materials	Total On-Chip Loss (dB)	Cross-Talk (dB)	PDL (dB)	PDD (nm)
Design A	0.4	$SiON/SiO_2$	30-40	-10	3.2	0.9
Design B	0.8	$SiON/SiO_2$	30-40	-12	3.2	0.9
Z. Sun	0.144	$SiON/SiO_2$	18-30	-9	NA	NA
Z. Sun	0.29	$SiON/SiO_2$	20-40	-20	~ 1	1.2
J.-J. He	2.0	InGaAsP/InP	10	-25	~ 0.5	0.3-0.4
P.C. Clemens	2.0	SiO_2/Si	5-15	-20	1-3	0.25
K. Liu	0.78	SiO_2/Si	22	-15	5	0.3
C. Cremer	3.7	InGaAsP/InP	18	-25	NA	0.5

Note: PDL – polarization dependent loss, PDD – polarization dependent dispersion

Table 5.3 A comparison of the performance of the linear grating spectrometers designed in this work to other similar designs.

absorption. The slab waveguide loss for the devices in this work needs to be reduced. It is possible to reduce the on-chip loss by 15 – 20 dB by improving on the propagation loss in the slab and ridge waveguides. The polarization dependent loss (PDL) is high in comparison with the other designs. This is a problem with the slab waveguide composition. Devices fabricated in InGaAsP/InP seem to show better polarization dependent dispersion (PDD) and PDL figures. The PDD measured for the devices in this work was found to be typical of devices fabricated in $SiON/SiO_2$ (and can be reduced or eliminated). It may be instructive to consider changing the slab material to the InGaAsP/InP formulation.

5.10 CONCLUSIONS

The linear grating spectrometers designed in this work performed comparably to other devices in the literature with the exception of total on-chip loss. The output channel spacing was found to be constant on any given chip (linear channel spacing) and the design was proven to have merit as a demultiplexer or a spectrometer. The linear grating spectrometers did not perform as well as expected relative to the benchmarks for a DWDM demultiplexer. The high on-chip loss and significant polarization dependent performance were not satisfactory. The on-chip loss and much of the polarization dependence, as has been previously discussed, can be significantly reduced by using a different layer structure or material fabrication process. The resolution of the diffraction grating was shown to be excellent and the spectrometer performance on the whole should improve dramatically if the ridge waveguide failings were improved. Cross-talk was not reduced compared to concave grating designs; however the performance of the grating (without the output waveguides in place) was found to have minimal cross talk between adjacent channels. This shows that the integrated linear grating design could produce good cross-talk figures if the ridge waveguide performance was improved.

CHAPTER SIX

FINITE DIFFERENCE TIME DOMAIN MODELING

6.1 BACKGROUND

The diffraction effects of the retro-reflecting grating facets in the near-field region are complicated due to the many reflections of the incident wave on the three available interfaces. The loss due to these diffraction effects as well as the loss due to transmission at the guide-air interface are properties that need to be understood for optimal spectrometer performance. A numerical simulation of the propagation of incident and scattered light can give a good indication of the behaviour of fabricated spectrometers. These numerical simulations may be able to aid in the design of future spectrometer devices.

The most applicable algorithm to this particular problem is the finite difference time domain (FDTD) algorithm. In this algorithm, a set of partial differential equations are satisfied in space and time by solving them in discrete space and time steps. The application of the FDTD algorithm used in this work specifically satisfies Maxwell's time dependent electromagnetic equations everywhere in a three-dimensional space for a given incident electromagnetic pulse.

The application of FDTD to electromagnetic field analysis was initially conceived by Yee in 1966 [27]. Many variations of this original method have been developed but the most commonly referenced FDTD algorithm is Yee's algorithm. Yee published a series of discrete equations that calculated the electric and magnetic field in a preset grid in two-dimensional space. The key to this method lay in the spatial mesh chosen to create an order in the incremental change of the co-dependent fields. Maxwell's equations in three dimensions result in a system of six coupled partial differential equations which can be solved in only a few cases analytically. Numerical solutions may be found, however, for any number of situations. The Yee algorithm is accurate to second order in the spatial and time derivatives. An excellent explanation of the development of the Yee algorithm in three dimensions is given by Taflove [28] and will be followed in this description.

6.2 YEE FINITE DIFFERENCE ALGORITHM

The Yee algorithm was designed to solve Maxwell's time dependent electromagnetic equations in a region of space where there are no sources. In this case, Maxwell's equations become

$$\frac{\partial \vec{H}}{\partial t} = -\frac{1}{\mu}\nabla \times \vec{E} - \frac{\rho}{\mu}\vec{H}$$
$$\frac{\partial \vec{E}}{\partial t} = \frac{1}{\varepsilon}\nabla \times \vec{H} - \frac{\sigma}{\varepsilon}\vec{E} \qquad 6.1$$
$$\nabla \cdot \vec{H} = 0$$
$$\nabla \cdot \vec{E} = 0$$

where ρ is the magnetic resistivity (Ω/m) and σ is the electric conductivity (Siemens/m). Yee's original algorithm restricted the testing to materials that have $\rho = \sigma = 0$ however it is easily extended to cases where the resistivity and conductivity are non-zero. In this work, materials with zero resistivity and optional non-zero conductivity may be studied. By defining a non-zero conductivity, it is possible to model lossy dielectrics without increasing the number of calculations in the code. If there are no sources in the region of interest, Maxwell's divergence equations offer no interesting information about the interaction of the electric and magnetic fields and therefore will be ignored. The curl equations result in a set of six coupled partial differential equations that must be solved to determine the evolution of the electric and magnetic fields in the region of interest.

In order to define the finite difference equations, a simple notation must be defined to make the equations clear and concise. Any point in space-time is defined by a spatial 3-vector as well as a designation of the time at which this spatial vector is valid. In the finite difference scheme, both space and time are defined by discrete grids of step sizes (Δx, Δy, Δz, Δt). Any point in this grid may be identified by the corresponding integer indices (i, j, k, n). A quantity may be evaluated at any point in space defined by the Yee notation

$$A(i\Delta x, j\Delta y, k\Delta z, n\Delta t) = A^{n}_{i,j,k} \qquad 6.2$$

Using this notation, the centered finite difference definition of the derivative of A with respect to the spatial coordinate x is

$$\frac{\partial A}{\partial x}(i\Delta x, j\Delta y, k\Delta z, n\Delta t) = \frac{A^n_{i+1/2,j,k} - A^n_{i-1/2,j,k}}{\Delta x} + O\left[(\Delta x)^2\right] \qquad 6.3$$

and similarly the time derivative is given by

$$\frac{\partial A}{\partial t}(i\Delta x, j\Delta y, k\Delta z, n\Delta t) = \frac{A^{n+1/2}_{i,j,k} - A^{n-1/2}_{i,j,k}}{\Delta t} + O\left[(\Delta t)^2\right] \qquad 6.4$$

The increment of the indices (i, j, k, n) by ½ is slightly counter-intuitive; however, in the Yee algorithm the electric and magnetic fields are determined at spatially separated points within the grid cell as well as calculated ½ Δt apart. The relative positions of the electric and magnetic fields are shown in Figure 6.1. The significance and usefulness of this unusual notation will become clear when it is applied to Maxwell's equations.

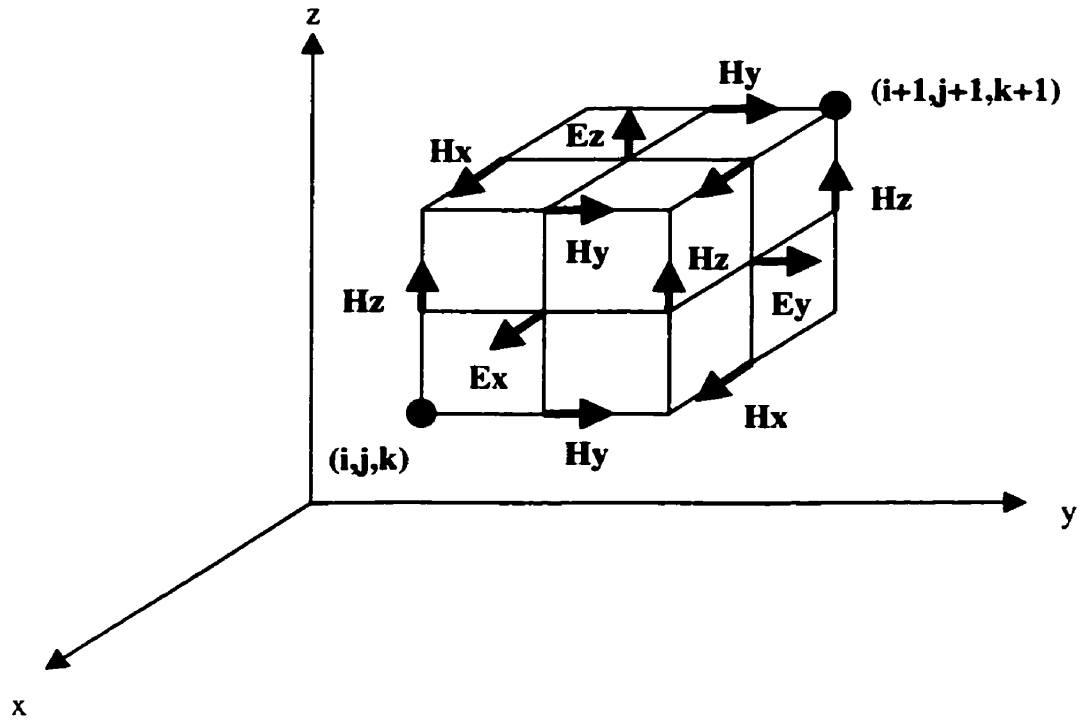

Figure 6.1 The Yee cell. Electric (**E**) and magnetic (**H**) fields are defined at positions displaced by ½ a spatial unit (Δx, Δy, Δz).

Consider the x-component of the electric field;

$$\frac{\partial E_x}{\partial t} = \frac{1}{\varepsilon}\left(\frac{\partial H_z}{\partial y} - \frac{\partial H_y}{\partial z} - \sigma E_x\right) \tag{6.5}$$

In finite difference notation, Equation 6.5 becomes

$$\frac{E_x\big|_{i,j,k}^{n+1/2} - E_x\big|_{i,j,k}^{n-1/2}}{\Delta t} = \frac{1}{\varepsilon_{i,j,k}}\left(\begin{array}{l}\dfrac{H_z\big|_{i,j+1/2,k}^{n} - H_z\big|_{i,j-1/2,k}^{n}}{\Delta y} \\ -\dfrac{H_y\big|_{i,j,k+1/2}^{n} - H_y\big|_{i,j,k-1/2}^{n}}{\Delta z} - \sigma_{i,j,k} E_x\big|_{i,j,k}^{n}\end{array}\right) \tag{6.6}$$

Using an approximation for the value of $E_x\big|_{i,j,k}^{n}$ in terms of the values at adjacent time steps,

$$E_x\big|_{i,j,k}^{n} = \frac{E_x\big|_{i,j,k}^{n+1/2} + E_x\big|_{i,j,k}^{n-1/2}}{2} \tag{6.7}$$

and collecting like terms, an expression for the time updated x-component of the electric field can be shown to be

$$\begin{aligned} E_x\big|_{i,j,k}^{n+1} = & \left(\frac{1 - \dfrac{\sigma_{i,j,k}\Delta t}{2\varepsilon_{i,j,k}}}{1 + \dfrac{\sigma_{i,j,k}\Delta t}{2\varepsilon_{i,j,k}}}\right) E_x\big|_{i,j,k}^{n} \\ & + \left(\frac{\dfrac{\Delta t}{\varepsilon_{i,j,k}}}{1 + \dfrac{\sigma_{i,j,k}\Delta t}{2\varepsilon_{i,j,k}}}\right)\left(\frac{H_z\big|_{i,j+1/2,k}^{n+1/2} - H_z\big|_{i,j-1/2,k}^{n+1/2}}{\Delta y} - \frac{H_y\big|_{i,j,k+1/2}^{n+1/2} - H_y\big|_{i,j,k-1/2}^{n+1/2}}{\Delta z}\right) \end{aligned} \tag{6.8}$$

Similar equations can be found for the remaining electric and magnetic field components. A more complete derivation may be found in Taflove [28]. It should be noted that the notation has worked out such that for updating the electric field at time step n+1, the most recent calculation of the electric field is at time step n while the most recent magnetic

field calculation occurred at time t = (n + ½)Δt. The implementation of the finite difference algorithm is simplified by defining separate indices for the electric and magnetic field for the spatial indices, thereby effectively keeping them separated by ½ grid steps (integrated into the equations) but making the algorithm easy to understand.

6.2.1 ALGORITHM STABILITY

The stability of the Yee algorithm, as with any numerical algorithm, depends heavily on the size of the steps between calculations (spatial or temporal). If the step is too large, the assumption of the continuity between points becomes untenable and invalid. Conversely, if the step is too small, computation in the given region becomes very slow. The ideal situation is one where the step is as large as possible before the calculations become unstable.

For solutions of partial differential wave equations the criterion used is the Courant-Friedrichs-Lewy stability criterion, more often called the Courant condition [29]. This condition, in one dimension, requires that the square of the distance the wave (or particle) being modeled can travel within a time Δt at it's maximum speed must be smaller than or equal to the square of the spatial grid step. In the case of the Yee algorithm, this condition requires that the propagating wave cannot outrun the electric field updating that can only be done one grid step at a time. For a wave in three dimensions the Courant condition is

$$\left(\frac{v_x \Delta t}{\Delta x}\right)^2 + \left(\frac{v_y \Delta t}{\Delta y}\right)^2 + \left(\frac{v_z \Delta t}{\Delta z}\right)^2 \leq 1 \qquad 6.9$$

where (v_x, v_y, v_z) and (Δx, Δy, Δz) are the velocities and grid steps of the wave in the x, y and z directions respectively. As an approximation for the Courant condition for the Yee algorithm, choose the maximum of (v_x, v_y, v_z) and set all velocities to be this value. This decreases the time step allowed, thereby making the algorithm more stable during computations. For the applications studied here, the maximum speed of the electromagnetic waves is the speed of light in vacuum. The condition reduces, under these conditions, to

$$\Delta t \le \frac{1}{c_o\sqrt{\left(\frac{1}{\Delta x}\right)^2+\left(\frac{1}{\Delta y}\right)^2+\left(\frac{1}{\Delta z}\right)^2}} \qquad 6.10$$

This equation was used to ensure mathematical stability of the Yee algorithm.

6.2.2 TOTAL FIELD FORMULATION

In the total field formulation, the scattered field as well as the incident field is included in the field update equations. In the simplest case, a one-dimensional computational domain, the total field at any point in the FDTD grid is given by

$$E_{z,tot}\Big|_i^{n+1} = E_{z,tot}\Big|_i^{n} + \frac{\Delta t}{\varepsilon_o \Delta x}\left(H_{y,tot}\Big|_{i+1/2}^{n+1/2} - H_{y,tot}\Big|_{i-1/2}^{n+1/2}\right) \qquad 6.11$$

and the total magnetic field is described as

$$H_{y,tot}\Big|_{i+1/2}^{n+1/2} = H_{y,scattered}\Big|_{i+1/2}^{n+1/2} + H_{y,incident}\Big|_{i+1/2}^{n+1/2} \qquad 6.12$$

In this work, the total field was calculated at every point in the computational domain using the total field formulation. This was a straightforward implementation as the incident pulse was only applied at the left edge of the domain. At all other points in the

grid, the total field was exactly the scattered field. For more information about implementation of the total field formulation in cases where the source is more complex, refer to Taflove [28].

6.3 MUR ABSORBING BOUNDARY CONDITIONS

The calculation of the fields at any point in the computational domain depends on the fields in the surrounding grid points. On the edge of the calculation space, the field depends on grid points outside the region of interest therefore another method must be used to determine these field points. Artificial reflections occur at the boundaries causing the true propagating field to be distorted if no precautions are taken. The blanket term used to describe the many special boundary calculations that exist is absorbing boundary conditions (ABC). Much research has been done to find suitable absorbing boundary conditions but a simple and widely used ABC is that described by Mur [30]. This ABC formulation gives second order absorption over most of the boundary.

The field components satisfy the three dimensional scalar wave equation,

$$\frac{\partial^2 A}{\partial x^2}+\frac{\partial^2 A}{\partial y^2}+\frac{\partial^2 A}{\partial z^2}-\frac{1}{c^2}\frac{\partial^2 A}{\partial t^2}=0 \tag{6.13}$$

A general solution to this equation for a wave travelling toward the x = 0 boundary is given by

$$A=\mathrm{Re}\left\{\psi\left[t+\left(x\sqrt{\frac{1}{c_o^2}+\frac{1}{v_y^2}+\frac{1}{v_z^2}}+\frac{y}{v_y^2}+\frac{z}{v_z^2}\right)\right]\right\} \tag{6.14}$$

The first order boundary condition for this wave becomes

$$\frac{\partial A}{\partial x} - \left(\frac{\sqrt{1-(c_o/v_y)^2-(c_o/v_z)^2}}{c_o} \right) \frac{\partial A}{\partial t}\bigg|_{x=0} = 0 \qquad 6.15$$

This equation requires some knowledge of the incident angle of the wave (which is not always known), therefore a first order approximation of the Taylor series expansion of the square root term is used and the first order boundary condition becomes

$$\frac{\partial A}{\partial x} - \frac{1}{c_o}\frac{\partial A}{\partial t}\bigg|_{x=0} = 0 \qquad 6.16$$

Using the second order term in the square root expansion, the second order boundary condition is

$$\frac{1}{c_o}\frac{\partial^2 A}{\partial x \partial t} - \frac{1}{c_o^2}\frac{\partial^2 A}{\partial t^2} + \frac{1}{2}\left(\frac{\partial^2 A}{\partial y^2} + \frac{\partial^2 A}{\partial z^2} \right)\bigg|_{x=0} = 0 \qquad 6.17$$

In an analogous manner to that used by Yee in the finite difference field updating equations, Mur applied the centered difference scheme to the partial differential equation in Equations 6.3 and 6.4. The discrete finite difference equation for the second order Mur ABC in Equation 6.17 is

$$\begin{aligned} A|_{0,j,k}^{n+1} = & -A|_{1,j,k}^{n-1} + \frac{c\Delta t - \Delta x}{c\Delta t + \Delta x}\left(A|_{1,j,k}^{n+1} + A|_{0,j,k}^{n-1} \right) + \frac{2\Delta x}{c\Delta t + \Delta x}\left(A|_{0,j,k}^{n} + A|_{1,j,k}^{n} \right) \\ & + \frac{(c\Delta t)^2 \Delta x}{2\Delta y^2 (c\Delta t + \Delta x)}\left(A|_{0,j+1,k}^{n} - 2A|_{0,j,k}^{n} + A|_{0,j-1,k}^{n} + A|_{1,j+1,k}^{n} - 2A|_{1,j,k}^{n} + A|_{1,j-1,k}^{n} \right) \\ & + \frac{(c\Delta t)^2 \Delta x}{2\Delta z^2 (c\Delta t + \Delta x)}\left(A|_{0,j,k+1}^{n} - 2A|_{0,j,k}^{n} + A|_{0,j,k-1}^{n} + A|_{1,j,k+1}^{n} - 2A|_{1,j,k}^{n} + A|_{1,j,k-1}^{n} \right) \end{aligned} \qquad 6.18$$

These boundary conditions are applied to the field components that are tangential to and at the edge of the computational domain.

6.4 BERENGER PERFECTLY MATCHED LAYER

The Mur absorbing boundary conditions are sufficient in many cases to absorb the reflected power from a scatterer. In some cases, however, Mur boundary conditions are not powerful enough to absorb intense reflections or reflections incident at oblique angles. A new formulation for boundary conditions was derived by Jean-Pierre Berenger in 1994 in two dimensions [31]. His formulation was shown to be orders of magnitude more absorptive than the traditional Mur boundary conditions. This new technique became very popular and was specifically applied to waveguide simulations because of its ability to absorb fields incident from any direction (not just normally incident fields). The technique was extended to three dimensions by Katz et al. later that year [32].

Berenger's derivation of the perfectly matched layer (PML) suggested that the computational domain could be surrounded by a material that had increasing conductivity towards the edge of the computational domain. The increasing conductivity created a lossy layer which quickly absorbed the incident field in a layer only a few FDTD cells thick (5-10 cells typically). By making the conductivity increase as a function of position, the perfectly matched layer maintains the usual scattering boundary conditions (tangential field components must be continuous across the boundary) while efficiently absorbing the incident field. It can be shown that the PML conditions satisfy the continuity conditions for an arbitrary plane wave incident on the boundary [33] regardless of its polarization or incident angle.

The Berenger PML formulation involved the creation of an imaginary split field which added a degree of freedom to Maxwell's equations so that even waves at oblique

incidence may be attenuated. The transverse fields are split into two orthogonal components so that the PML can be dispersionless and highly absorbing for all frequencies and angles of incidence. This formulation is somewhat difficult to visualize since the system is artificially complicated by the orthogonal split field components. Another formulation was suggested that used the same conductivity matching idea as Berenger's PML but with a slightly simpler format.

The stretched-coordinate formulation was derived by Chew and Weedon [34] and independently by Rappaport [35] which replaces the split field components by a representation (mapping) in complex space. The mapping results in a simple and compact way of describing the action of the PML. In complex space, the spatial coordinates become

$$\tilde{x} \rightarrow \int_0^x s_x(x')dx' \tag{6.19}$$

with similar relations for the y and z components. The partial derivative becomes

$$\frac{\partial}{\partial \tilde{x}} \rightarrow \frac{1}{s_x}\frac{\partial}{\partial x} \tag{6.20}$$

where s_x is a continuous function. Maxwell's equations, under this transformation, become

$$\begin{aligned} j\omega\varepsilon\vec{E} &= \vec{\nabla}\times\vec{H} \\ &= \hat{x}\left[\frac{1}{s_y}\frac{\partial H_z}{\partial y} - \frac{1}{s_z}\frac{\partial H_y}{\partial z}\right] + \hat{y}\left[\frac{1}{s_z}\frac{\partial H_x}{\partial z} - \frac{1}{s_x}\frac{\partial H_z}{\partial x}\right] + \hat{z}\left[\frac{1}{s_x}\frac{\partial H_y}{\partial x} - \frac{1}{s_y}\frac{\partial H_x}{\partial y}\right] \end{aligned} \tag{6.21}$$

$$\begin{aligned} -j\omega\mu\vec{H} &= \vec{\nabla}\times\vec{E} \\ &= \hat{x}\left[\frac{1}{s_y}\frac{\partial E_z}{\partial y} - \frac{1}{s_z}\frac{\partial E_y}{\partial z}\right] + \hat{y}\left[\frac{1}{s_z}\frac{\partial E_x}{\partial z} - \frac{1}{s_x}\frac{\partial E_z}{\partial x}\right] + \hat{z}\left[\frac{1}{s_x}\frac{\partial E_y}{\partial x} - \frac{1}{s_y}\frac{\partial E_x}{\partial y}\right] \end{aligned} \tag{6.22}$$

In order for the fields to be absorbed appropriately, the PML material must be anisotropic. It can be shown that continuity can be maintained as long as the conductivity is scaled along the normal axis (Berenger 1994). The anisotropy is modeled by defining different conductivities to the x-, y- and z-directions. A possible formula for the factor s_i is

$$s_i = 1 + \frac{\sigma_i}{j\omega\varepsilon} \tag{6.23}$$

and even greater attenuation can be achieved by the use of an extra factor κ such that for situations where high attenuation is required;

$$s_i = \kappa_i + \frac{\sigma_i}{j\omega\varepsilon} \tag{6.24}$$

The conductivity is scaled along the direction perpendicular to the boundary of interest. The wave impinging on a given boundary is absorbed by the monotonically increasing conductivity it encounters on its path toward the boundary.

Finding the optimal combination of the attenuation parameters κ and σ is a tedious task that has been performed by other researchers (Berenger 1996, 1997 [36,37] and others as below) and the results of these experiments were used in this work. Polynomial scaling of both κ and σ are suggested by Berenger [36] where

$$\begin{aligned} \sigma(x) &= \left(\frac{x}{g}\right)^q \sigma_{\max} \\ \kappa(x) &= 1 + (\kappa_{\max} - 1)\left(\frac{x}{g}\right)^q \end{aligned} \tag{6.25}$$

where q is an integer and g is the thickness of the PML layer. The conductivity σ ranges from zero at the PML/material boundary to σ_{max} at the computational domain boundary. The value of κ ranges from one at the PML/material boundary to κ_{max} at the

computational domain boundary. The choice of $\kappa_{max} \geq 1$ may be determined on a case-by-case basis, depending on the required attenuation. In these simulations, κ_{max} was set to a value of 2.0. The entire computational domain is surrounded by a perfect electrical conductor that will reflect any fields that transmit through the PML layer but also gives an easy way of calculating the field at the boundary of the computational domain. Other material choices along the boundary require the knowledge of fields outside the computational domain due to FDTD equation formulations.

The theoretical reflection of a field incident from an angle θ from the perfect electrical conductor is given by

$$R(\theta) = \exp\left(-2\eta\varepsilon_r\sigma_{\max} g \cos\theta/(q+1)\right) \qquad 6.26$$

for polynomial-scaled conductivity (as in Equation 6.25). Generally, values for the allowable reflection R, the scaling factor q, the PML layer thickness g and material relative permittivity ε_r are chosen for a given modeling situation and a value for the maximum conductivity of the layer, σ_{max}, is calculated using Equation 6.26. It has been found (Gedney [38] and He [39]) that the optimal choice for the maximum conductivity of a 5-cell thick PML layer (with an allowed reflection of $R \sim e^{-8}$) is

$$\sigma_{opt} = \frac{q+1}{150\pi\Delta x\sqrt{\varepsilon_r}} \qquad 6.27$$

The best results are found using a value of q of between 3 and 4 [38,41,42]. In this work, a 10-cell thick PML layer was used with a polynomial scaling factor, q, of 2. The value of maximum conductivity used in this work was empirically adjusted from the value calculated using Equation 6.27 to arrive at the lowest reflection from the computational boundary.

6.4.1 PML FDTD IMPLEMENTATION

Using Equations 6.21 and 6.22, Maxwell's equations are transformed into FDTD equations for the PML regions. For a three-dimensional space that allows for conductivity scaling in the x-, y-, and z-directions, Equation 6.21 becomes

$$\begin{bmatrix} \frac{\partial H_z}{\partial y} - \frac{\partial H_y}{\partial z} \\ \frac{\partial H_x}{\partial z} - \frac{\partial H_z}{\partial x} \\ \frac{\partial H_y}{\partial x} - \frac{\partial H_x}{\partial y} \end{bmatrix} = j\omega\varepsilon_o\varepsilon_r \begin{bmatrix} \frac{s_y s_z}{s_x} & 0 & 0 \\ 0 & \frac{s_x s_z}{s_y} & 0 \\ 0 & 0 & \frac{s_x s_y}{s_z} \end{bmatrix} \begin{bmatrix} E_x \\ E_y \\ E_z \end{bmatrix} \tag{6.28}$$

where s_i are given by Equation 6.24 for the most general case. The electric field can be determined using the electric displacement, D,

$$D_x = \varepsilon_o\varepsilon_r \frac{s_z}{s_x} E_x \qquad D_y = \varepsilon_o\varepsilon_r \frac{s_x}{s_y} E_y \qquad D_z = \varepsilon_o\varepsilon_r \frac{s_y}{s_z} E_z \tag{6.29}$$

Transformation of Equation 6.28 into a set of equations in FDTD format can be achieved by changing from the frequency domain into the time domain and by substituting expressions for the variables s_i. As an example of this transformation, consider the x-component of the electric field. The electric displacement (from Equation 6.29) gives

$$j\omega\left(\kappa_x + \frac{\sigma_x}{j\omega\varepsilon_o}\right) D_x = j\omega\varepsilon_o\varepsilon_r\left(\kappa_z + \frac{\sigma_z}{j\omega\varepsilon_o}\right) E_x \tag{6.30}$$

Transformation into the time domain creates

$$\frac{\partial}{\partial t}(\kappa_x D_x) + \frac{\sigma_x}{\varepsilon_o} D_x = \varepsilon_o\varepsilon_r\left[\frac{\partial}{\partial t}(\kappa_z E_x) + \frac{\sigma_z}{\varepsilon_o} E_x\right] \tag{6.31}$$

This equation can be transformed into an FDTD equation by using Equations 6.4 and 6.7 to replace the time derivative terms with centered difference expressions and by expressing the other two terms as averages of the previous and present values of E and D.

Perfectly matched layer boundary conditions are very powerful for absorbing all types of reflected fields in many applications. It is especially useful in this work as the reflected power is quite large and tends to over-power the Mur absorbing boundary conditions. Sufficient attenuation of the reflected fields can be achieved with the PML formulation, regardless of the incident direction.

6.5 NEAR TO FAR FIELD TRANSFORMATION

The calculations involved in FDTD simulations are very computationally intensive therefore it is instructive to limit the size of the computational domain as much as possible. In many applications, researchers are interested in finding the EM fields far from the scatterer. It is possible to extend the computational domain into the far field limit however this is both computationally expensive and susceptible to cumulative errors in the numerical field calculations. A better approach to finding the fields in the far field is using the fields calculated in the near field regime and transforming that information into the far field.

The approach used in this work utilized the time domain near-to-far field transformation. At the heart of the transformation is the surface equivalence theorem. This theorem states that the fields outside any arbitrary imaginary closed surface may be obtained by applying magnetic and electric current densities on that closed surface that

satisfy the boundary conditions and that are equivalent to the effect of the sources inside the closed surface [28]. The system is therefore changed from a source enclosed by an arbitrary surface to a source-free region bounded by the same arbitrary surface with electric and magnetic current densities found on the surface. The total field at any point in the far field is calculated by considering the summed effect of these current densities at that far field observation point.

The most straightforward approach to calculating the electric and magnetic current densities is to choose the arbitrary, closed, imaginary surface to be a box that encloses the scatterer of interest. Along each of the faces of the box, the components of the electric and magnetic field densities, J_i and M_i respectively, are determined by

$$\begin{aligned} \vec{J} &= \hat{n} \times \vec{H} \\ \vec{M} &= -\hat{n} \times \vec{E} \end{aligned} \tag{6.32}$$

where $\hat{n}$ is the unit vector normal to one of the surfaces and $\vec{H}$ and $\vec{E}$ are the magnetic and electric fields found along that boundary. The radiation vectors (see Luebbers [43] and Yee [44]) are defined as

$$\begin{aligned} \vec{N} &= \int_S \vec{J}_s \exp(jk\vec{r}' \cdot \hat{r}) ds \\ \vec{L} &= \int_S \vec{M}_s \exp(jk\vec{r}' \cdot \hat{r}) ds \end{aligned} \tag{6.33}$$

where k is the wavenumber, $\hat{r}$ is the unit vector from the origin to the far field observation point and $\vec{r}'$ is the vector from the origin to the source point on the surface S. The far field frequency domain electric field is then given by

$$e_\theta = \frac{-j\exp(-jkR)(\eta N_\theta + L_\phi)}{2\lambda R}$$
$$e_\phi = \frac{j\exp(-jkR)(-\eta N_\phi + L_\theta)}{2\lambda R} \qquad 6.34$$

where η is the impedance of free space, R is the distance from the origin to the far field observation point and λ is the wavelength of interest. It is necessary to take the inverse Fourier transform of the formulae in Equation 6.34 to revert to the time domain regime. The inverse Fourier transform for the electric field components gives

$$E_\theta = -\eta W_\theta - U_\phi$$
$$E_\phi = -\eta W_\phi + U_\theta \qquad 6.35$$

where $\vec{W}$ and $\vec{U}$ are defined by

$$\vec{W}(t) = \frac{1}{4\pi Rc}\frac{\partial}{\partial t}\left[\int_S \vec{J}_s(t-\tau_d)ds\right]$$
$$\vec{U}(t) = \frac{1}{4\pi Rc}\frac{\partial}{\partial t}\left[\int_S \vec{M}_s(t-\tau_d)ds\right] \qquad 6.36$$

The factor τ_d is the time delay for the electromagnetic pulse to travel from the source point to the far field observation point and is given by

$$\tau_d = \frac{R - \vec{r}'\cdot\hat{r}}{c} = \frac{R - r'\cos\psi}{c} \qquad 6.37$$

To calculate the electric field components in an FDTD algorithm, the integral in Equation 6.36 is approximated by a sum of the contribution from each FDTD cell on the face of the surface S and the time derivative may be approximated by using the FDTD formulation in Equation 6.4. Full details of the FDTD implementation can be found in Taflove [28]. The orientation of the geometry used in this work is shown in Figure 6.2. The final result of the far field calculations is a vector of the electric field values at chosen point in space

as a function of time. The above derivation is for calculations done in three dimensions but there is an easy extrapolation to two dimensional cases (as given by Luebbers [43]).

6.6 CODE DEVELOPMENT

In this work, the FDTD code was originally translated into C (by the author) from original FORTRAN code written at Penn State University by Dr. Raymond Luebbers and associates [45]. The FORTRAN code formed the loose basis of final C code versions. Four unique codes have been developed. The first code is essentially the same as the Luebbers code with some modifications to the data saving techniques and a couple of changes to make the code somewhat faster. The second code evolved from the Luebbers code but there have been significant changes. The Yee algorithm and the Mur boundary conditions have remained as part of the code but many changes were made to make it applicable to waveguide devices. In particular, the electromagnetic source was changed from a wave travelling through the region of interest to a hard source at the $z = 0$ boundary. The third version of the FDTD code is a pared down, 2D version of the 3D hard source code. The 2D code is significantly faster and is the testing ground for possible changes to the 3D code. The 2D code is also useful for quick analysis of reflections from dielectric structures. Though the results may not be strictly accurate for waveguide devices, it is able to produce a reasonable approximation to the 3D waveguide situation. The fourth version of the code implemented the Berenger PML method as well as the near to far field transformation while maintaining the hard source Yee FDTD

algorithm. This code was left as a 2D implementation because of the added complexity of the boundary conditions and the far field transformation.

The original Luebbers code used a purely scattered field approach to the Yee algorithm. The incident field is propagated through the computational domain at which point scattered field is created due to the incident field interacting with the dielectric material. This code is useful for seeing the reflected field intensity however it does not accurately depict the action of the electromagnetic field at the dielectric boundaries (i.e. the grating facets). This formulation forces a calculation of the field at every point in the grid due to this incident travelling wave. The resulting reflected field is correct (obeys Maxwell's equations) but the transmitted field is unphysical at any boundary. The equations that calculated the field in the transmitted space force the addition of the user-defined incident field to the field created due to the interaction with the material at that point. This formulation is applicable to situations where only the reflected field is of interest. In the case of waveguide structures, transmitted fields at boundaries are the main concern therefore this formulation is not ideal for the work done in this thesis. Though the code is not ideal, it does give a very good visual representation of the reflected field with no dispersion of the incident field. The code was modified to account for dielectric media and easy refractive index mapping (as described below).

In the second 3D code, the formulation was changed from the purely scattered field to total field formulation. This required some fundamental changes to the Yee algorithm. The theory behind the total field formulation is given in Section 6.2.2. In addition to these fundamental changes, the Yee algorithm and ABC's were changed slightly to account for the fact the wave was not travelling in free space but within a lossy

dielectric. As well, the new code allows for easy mapping of the refractive index across the computational domain by reading in a text file that contains numbers corresponding to the material type at a given location in the calculation space. A three dimensional space is created by extrapolating the two dimensional map. While the program is running, values of the electric and magnetic fields are periodically written to files in a two dimensional slice of the space. A MATLAB script was written to create a movie of the 2D TE or TM field (a switch determined by the user) intensity as a function of time in the calculation space. This gives a good visual representation of the propagation of light through the system.

The code begins by building the refractive index map in the 3D space. Hard coded into the program is the creation of a slab waveguide with a user-defined core thickness. All parameters that are changed on a regular basis are contained within a separate "common" file and included upon compilation. Constants used by the Yee and ABC algorithms are calculated before any of the propagation begins to make the code faster. An incident EM pulse is created that emulates a plane wave (of a defined wavelength) in one direction and follows the single guided mode in the other direction perpendicular to the direction of propagation. According to the Yee algorithm, the scattered electric field components are calculated at time t = 0.0 in the x, y, and z directions for all grid points (except the edges) in the calculation region. The ABC's are applied at the boundaries of the calculation space to define the value of the scattered electric field at the edges of the calculation space. Once the boundary values of the electric field are determined, time is advanced by one half of a time step and the magnetic field components (H) are calculated in the x, y, and z directions for all grid points. Time

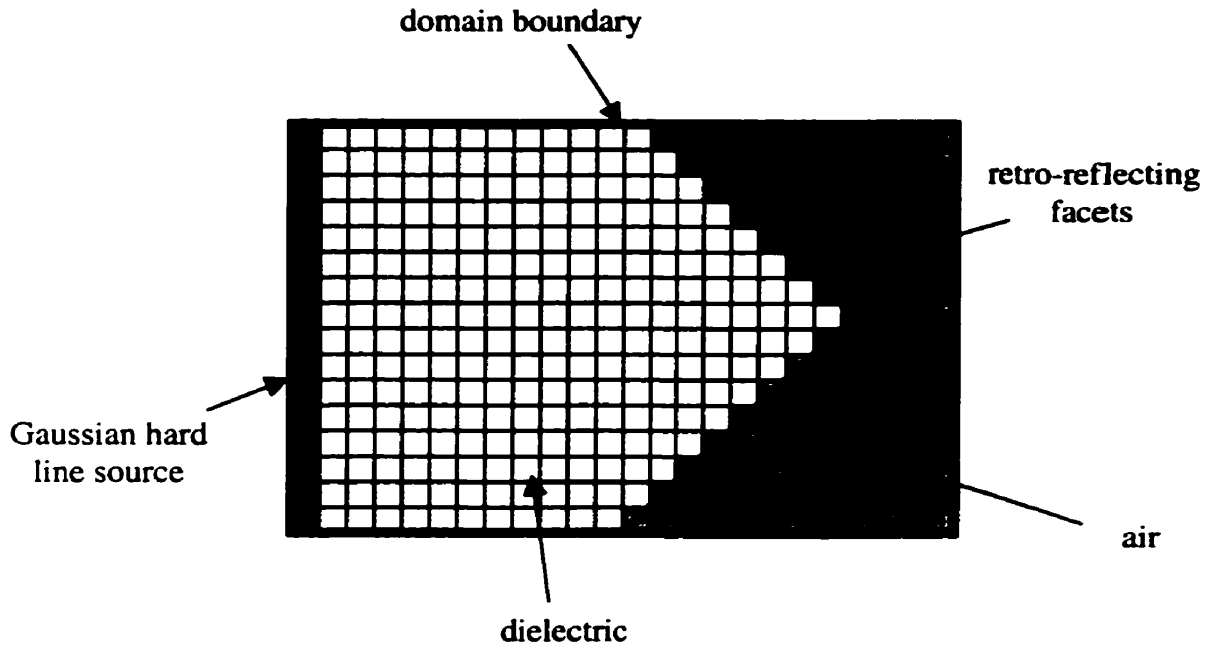

Figure 6.2 The basic geometry of the FDTD refractive index map used in this work.

is advanced a further one half time step and the user-defined field components of interest are saved at five time step intervals. The five-step interval was chosen because it reduces the amount of data saved to file to create the MATLAB movie without losing a great deal of the propagation details. This process is repeated for a user-defined number of time steps.

The three dimensional total field code was pared down to a two dimensional case to be used as a testing ground for new index maps. This code runs considerably faster than its three-dimensional counterpart and therefore it lends itself easily to be used repeatedly with different index maps. It has most of the same features as the three-dimensional code (the Yee algorithm and the Gaussian hard source) but the Mur boundary conditions were replaced with perfectly matched layer absorbing boundaries. This 2D code was used for all of the data shown in this chapter.

6.6.1 THE HARD SOURCE

The original FORTRAN code used a plane wave travelling through the calculation space in both directions perpendicular to the direction of propagation. This method produced a good representation of the field reflected by the grating facets but it gave no information on the fields transmitted through the grating. The propagation of the plane wave forced calculation of the field at points beyond the grating facets and therefore this was not a good method to use for loss determination (the main driving force behind doing this modeling). The most feasible approach was to apply a user-defined field at one edge of the calculation region. The source was defined to be a plane wave in the x direction, a Gaussian in the y direction (to simulate the slab waveguide mode) and have a temporal Gaussian pulse profile. These conditions were applied instead of the usual Mur boundary conditions for the duration of the pulse.

The change of source changed the Yee algorithm slightly and made it faster. In the purely scattered field formulation, calculation of the electric field required calculation of the applied incident field and it's derivative at every point in the space for every time step. The incident field calculations increased the calculation time significantly for larger grids

6.7 GRATING FACET MODELING RESULTS

Modeling of the entire diffraction grating through FDTD brute force simulations was considered not to be a feasible option with the computational power available to this

project and with the current FDTD algorithm. The goal of this work was not to create software for making fiber-to-fiber spectrometer performance calculations but rather to achieve a simulation of the physical phenomena occurring at the grating interface. A refractive index map was created that described a single retro-reflecting facet of the diffraction grating. The core material was assumed to be lossless with a refractive index of 1.501 (the specified index of the core used in the spectrometers). The reflective grating facet was defined by a structure created by a series of Yee cells with a refractive index of 1.00. The exact grating facet geometry of the spectrometers was used, including exact spatial angles and dimensions. The incident pulse had a wavelength of 1550 nm and various pulse durations were investigated. The pulse was generated using

$$E_{inc} = A\exp\left(\frac{t/\Delta t - n_o\beta}{\beta^2}\right)\sin\left(\frac{2\pi ct}{\lambda}\right) \qquad 6.38$$

where A is a constant, n_o defines the number of decay constants, β, that occur in the

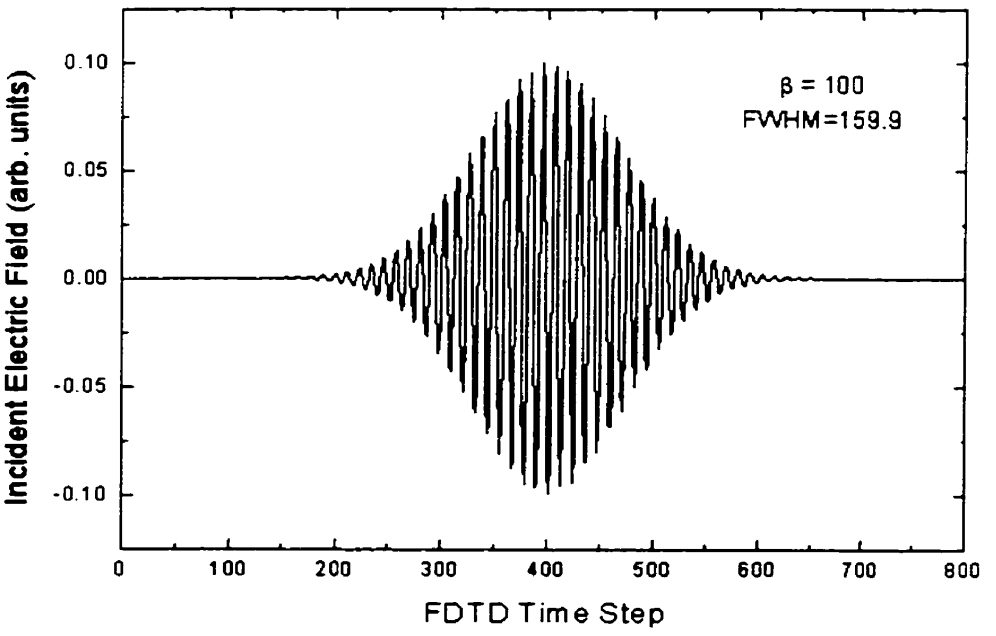

Figure 6.3 The applied electric field pulse shape used in this work (here β = 100).

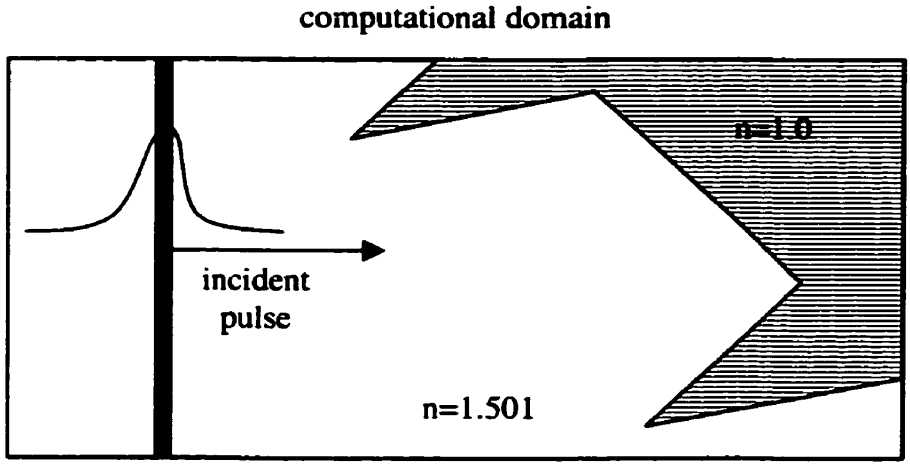

Figure 6.4 The grating facet index map used for the FDTD simulations.

pulsed duration of the sinusoidal oscillation of wavelength λ. The decay constant β was adjusted to create pulses of different durations. An example of the input pulse is shown in Figure 6.3. The parameters used in these simulations are shown in Table 6.1.

A	0.1	κ_{opt}	2.0
n_o	4.0	q	2.0
β	50, 100, 200	***PML layer thickness, g***	10

Table 6.1 Parameters used for FDTD simulations.

The far-field observation point was defined to be 100 or 1000 Yee cells from the center of the facet. The computational domain was 109 cells in the x-direction and 240 cells in the z-direction (the direction of propagation). Each Yee cell was defined to be 0.1 μm by 0.1 μm in real spatial dimensions. This corresponds to 6% of the wavelength of light used. To ensure the accuracy of the calculations, it is necessary to keep the Yee cell

dimensions at least one-tenth of the wavelength of the incident pulse for algorithm stability and for accurate results.

6.7.1 SCATTERED INTENSITY

The scattered electric field was calculated as a function of time at the far-field observation point. The reflected pulse shape (in time) and the angular distribution of reflected power were monitored. The reflected pulse shape as a function of input pulse duration will be discussed in Section 6.7.4. The scattered intensity (EE^*) was determined by computing a sum (running the length of simulation's duration) of the electric field intensity reaching a user-defined far-field point to give the total scattered intensity at a scattered angle, θ, defined from the negative z-axis. The total scattered intensity was measured for all possible scattering angles (including the transmitted field)

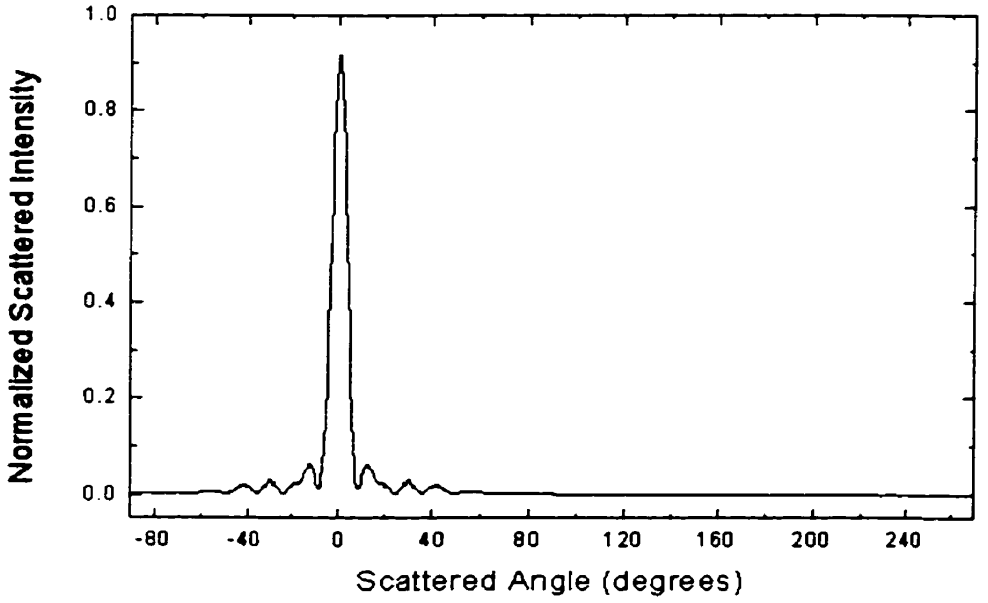

Figure 6.5 Total reflected and transmitted intensity as a function of angle (β= 100, r=100).

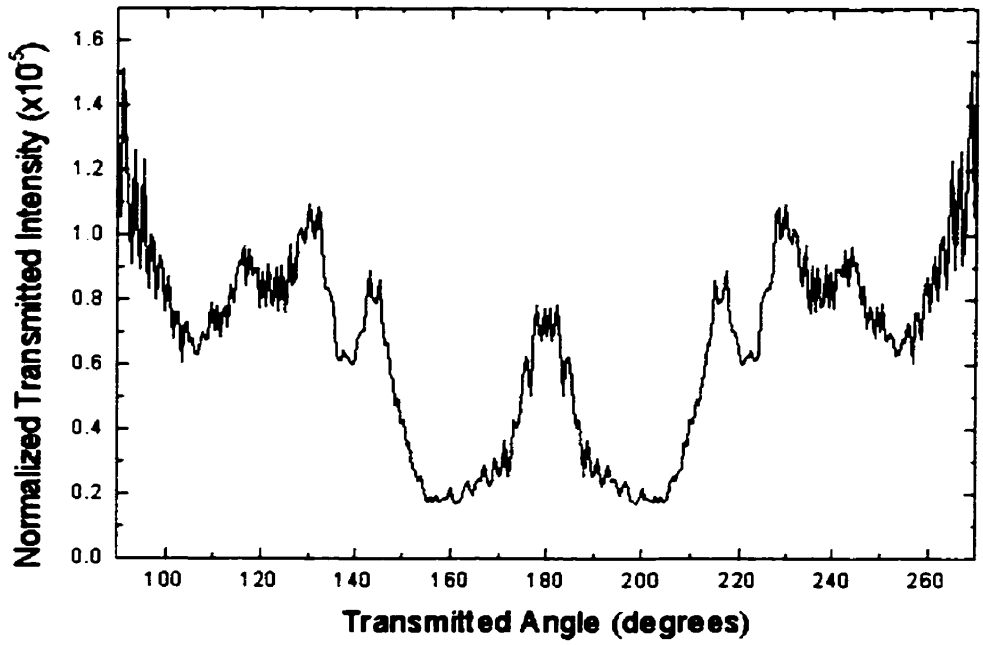

Figure 6.6 Total transmitted intensity as a function of angle (β= 100, r=100).

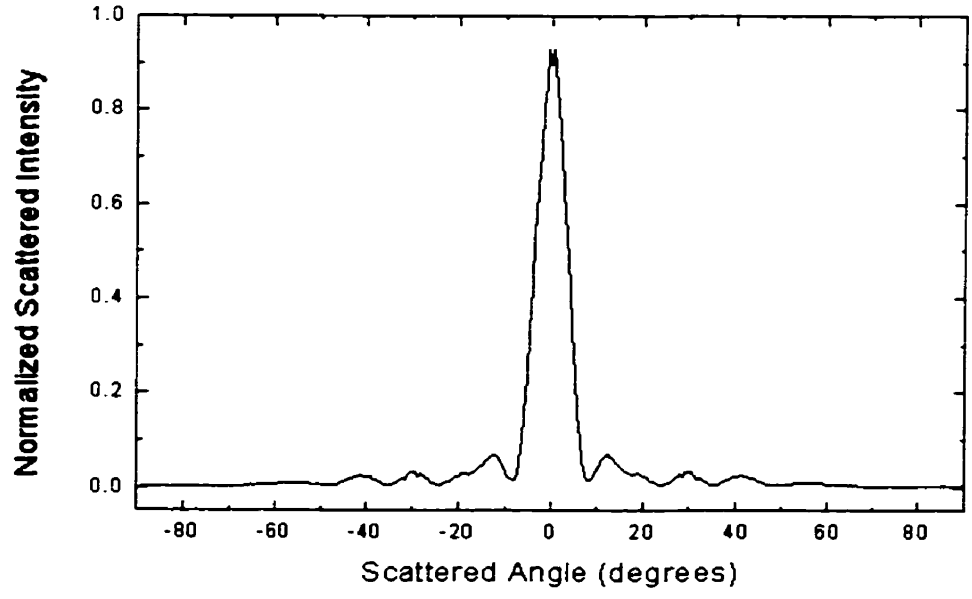

Figure 6.7 Total reflected intensity as a function of angle (β= 50, r=100).

and these results are shown in Figures 6.5 through 6.8 for different pulse lengths. The intensity has been normalized with the total incident intensity in all of these figures. The far-field intensity was measured at two different positions in the far-field domain. The majority of the figures shown were collected at a point $r = 100$ Yee cells from the center of the grating facet. For comparison, some calculations were made at a position $r = 1000$ Yee cells from the center of the grating facet. These conditions have been noted in each of the figure captions for clarity.

Figures 6.5 through 6.7 show the scattered and transmitted intensity for the modeled grating facet for an incident pulse with $\beta = 100$. The retro-reflected angle is 0°, and this coincides with the peak intensity for all incident pulse durations. The normalized transmitted intensity (for scattering angles greater than 90°) is two orders of magnitude

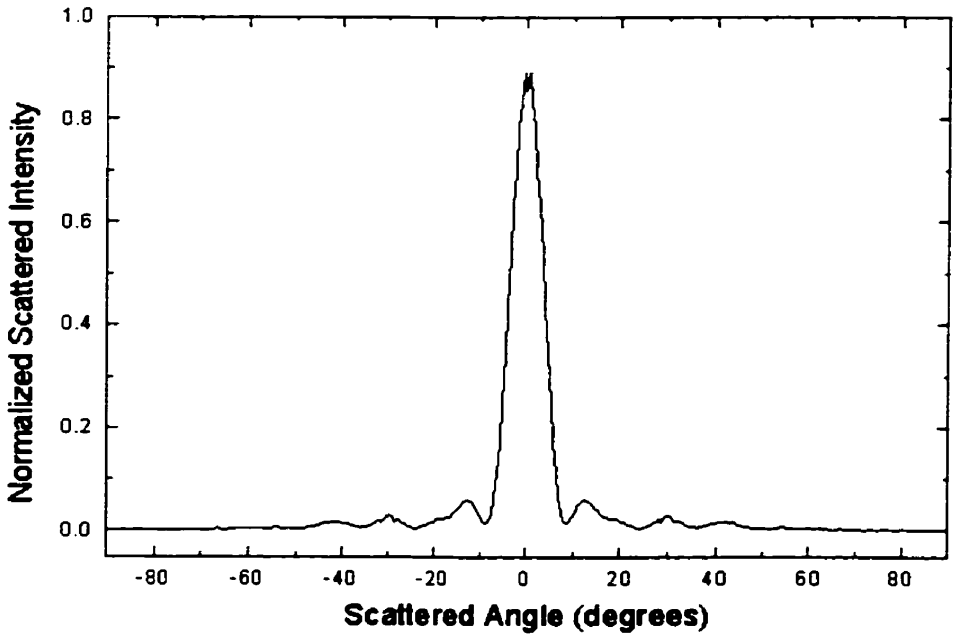

Figure 6.8 Total reflected intensity as a function of angle ($\beta = 200$, $r = 100$).

lower than the lowest reflected intensity and is shown in Figure 6.6 for β = 100. This implies that reflection from the grating facet (due to total internal reflection) is expected to be highly efficient. For the far-field observation point r = 100, the intensity pattern changes only in peak height and the shape remains the same (as can be seen in Figures 6.5 through 6.8) for changing pulse durations. The normalized central maxima height changes by 20% from the β = 50 to the β = 200 incident pulse cases. The secondary maxima heights increase by 11% between the β = 50 to the β = 200 incident pulse cases. This suggests that the reflection from the grating-air interface becomes more efficient as the pulse length increases.

One parameter that was not varied in the results discussed above was the far-field observation point, r. Figure 6.9 shows the reflected intensity at r = 1000 Yee cells for an incident pulse with β = 200. In comparison with the reflected intensity (for β = 200) measured at r = 100 Yee cells shown in Figure 6.8, the overall shape of the reflected

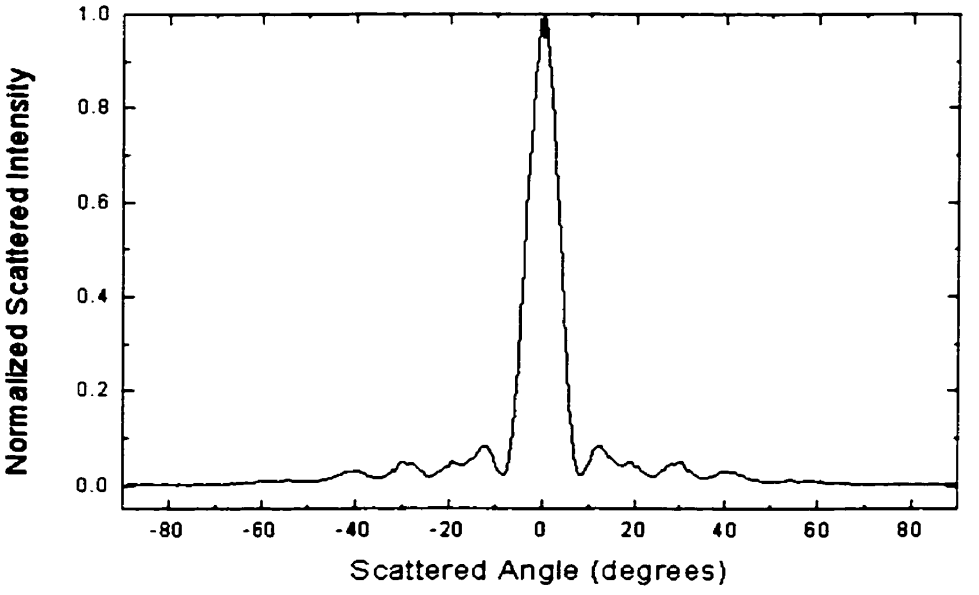

Figure 6.9 Total reflected intensity as a function of angle (β = 200, r = 1000).

intensity as a function of angle is identical with the exception of the height of the central peak. At the observation point r = 1000 Yee cells, 6% more of the incident light is scattered into the central maximum and 28% more light is scattered into the secondary maximum than at r = 100 Yee cells. This implies that more light converges on the retro-reflected angle at larger distances.

6.7.2 SCATTERED INTENSITY PROFILE

The shape of the scattered intensity shown in Figures 6.5 through 6.8 is reminiscent of the sinc function associated with diffracted intensity from a rectangular aperture. Some diffraction effects are expected due to reflection from these grating facets (due to the finite aperture of the grating facet) therefore the sinc^2 function intensity profile is expected according to the similarity of the geometry to a rectangular aperture. The data

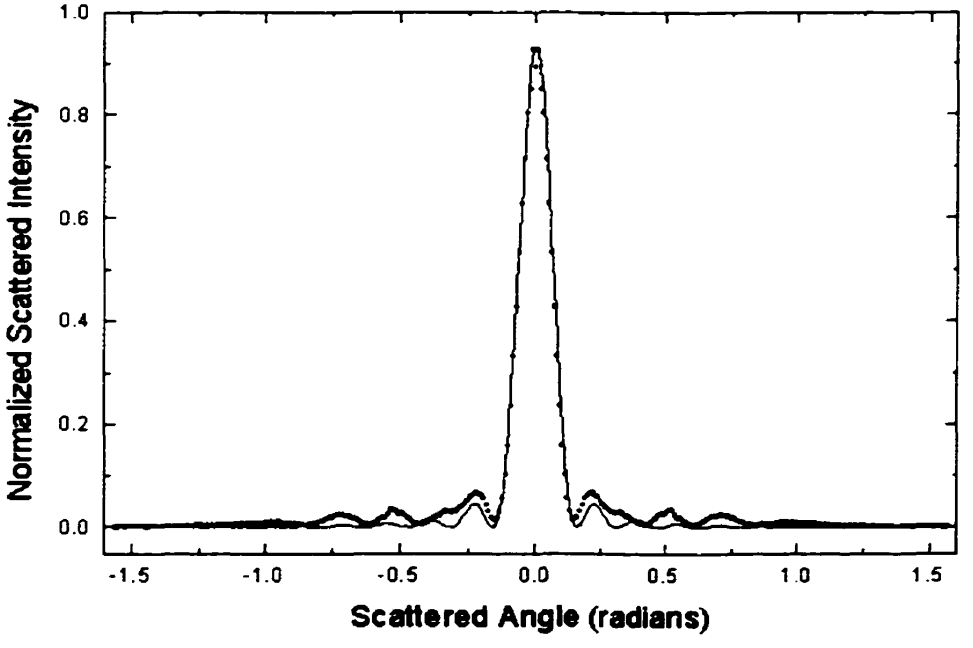

Figure 6.10 Total reflected intensity as a function of angle (β = 200, r = 100) for FDTD simulations (•) and sinc^2 function (-).

calculated for an incident pulse with β = 50, 100 and 200 and the far-field observation point r = 100 was used in the following sinc^2 curve fitting procedure. In Figures 6.10 through 6.12, the data calculated by the FDTD code is superimposed with a sinc^2 function. The sinc^2 function used to create the data set had the form

$$I = A\frac{\sin^2(B\theta)}{(B\theta)^2} \qquad 6.39$$

where A and B are variables and θ is the scattered angle in radians (for small angles θ). The curve shown in Figure 6.10 uses the numerical values A = 0.94 and B = 20.0. The value of B is the same for all three figures while A varies only slightly (0.92 to 0.94). Single slit diffraction theory determines that the intensity in the far-field follows this equation where the variable B relates to the physical parameters of the slit (and system) by

$$B = \frac{n_g \pi D}{\lambda_o} \qquad 6.40$$

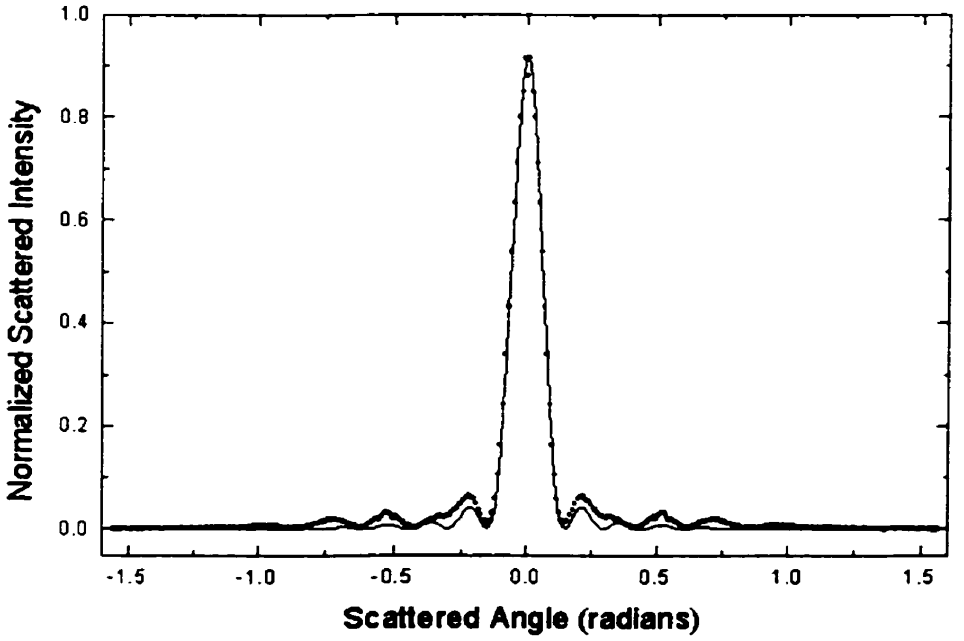

Figure 6.11 Total reflected intensity as a function of angle (β = 100, r = 100) for FDTD simulations (•) and sinc^2 function (-).

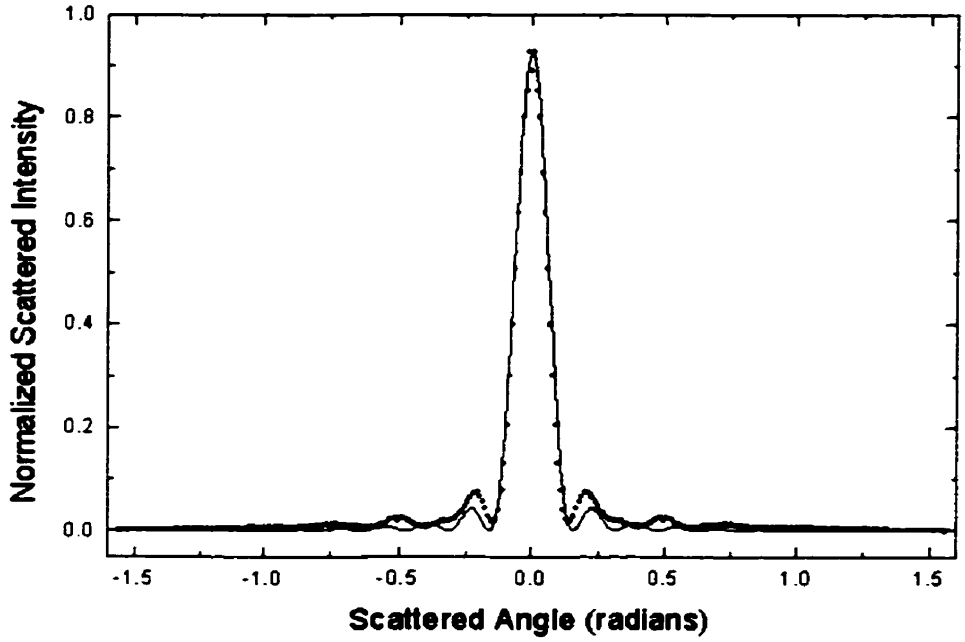

Figure 6.12 Total reflected intensity as a function of angle ($\beta = 50$, $r = 100$) for FDTD simulations (•) and sinc^2 function (-).

where n_g is the index of the propagation medium (1.501), λ_o (1.55 μm) is the free space wavelength of the light and D is the width of the grating facet (8.6 μm). Using the parameters of the physical system and the modeled value of the parameter B, the diffraction pattern predicts a facet opening of 6.6 μm. This differs from the actual facet opening by 23%. All of the pulse durations predict the same diffraction pattern parameter B. This is expected since it is a function of the diffracting facet geometry.

6.7.3 GRATING FACET REFLECTION EFFICIENCY

The efficiency of a diffraction grating is defined by the proportion of the total reflected power that is reflected into the retro-reflected order as compared to the power reflected into the adjacent orders. Although this work has not modeled the performance of the entire grating, knowledge may be gained about the spectrometer performance from the

performance of each grating facet. The far-field transformation done on the FDTD data produced information about the intensity of the light reflected in all directions. The efficiency of the grating facet is defined as the ratio of the total reflected power at the retro-reflected angle as compared to the total power reflected at all angles corresponding to orders of the grating.

The diffraction orders of the grating response occur at angles β given by

$$\sin\beta = \frac{m'\lambda_o}{n_g d} - \sin\alpha \qquad 6.41$$

where n_g is the effective index of the propagation medium, d is the period of the grating, α is the incident angle of the light, λ_o is the free space wavelength of the light used to define the spectrometer components, and m' is the order of the grating. The period of the grating is 11.6 μm and the order of the grating was defined to be 16 in this work. For the FDTD simulations, the free space wavelength of the light used was 1.55 μm; however the retro-reflected light of the grating was designed to be 1.526 μm therefore the second value was used in determining the angular positions of the adjacent grating orders. The relevant grating orders angular positions (ranging from m' = 1 to 19) were calculated. The (normalized) scattered intensity for each of these positions was summed using the data found in Figures 6.5 and 6.6 and the total was found to be 1.201. This shows that the normalization factor for the intensity of the light was too small. The height of the central diffraction peak was measured to be 0.915 (in normalized units). This makes the efficiency of the grating facet 76.2% for retro-reflection into the sixteenth order. Sadov and McGreer [47] calculated the efficiency of total internal reflection gratings with retro-

reflecting facets (for the TE mode) to be 4.5 dB. This does not concur with the results found with the FDTD calculations in this work (1.2 dB).

The efficiency calculated here does not necessarily relate to the overall performance of the spectrometer in any obvious way. The effects from each individual facet may interfere at the output focal plane of the spectrometer causing overall more efficient performance. It is also possible that the interference may cause less efficient performance. The conclusion that may be drawn from these results is that there is significant diffraction due to the size of the grating facet opening and this will inevitably contribute to cross-talk in the spectrometer though this cannot be quantified with these results. Full modeling of the grating would have to be done in order to determine the effect of the grating facet diffraction on the performance of the spectrometer. A paper by M. Smith and McGreer [46] give results about the efficiency of retro-reflecting facets. Using the full theory of electromagnetic radiation, Smith found that for a guiding layer with index 1.45 (glass), retro-reflecting facets should exhibit efficiency near –4 dB in the 20^{th} order. In this thesis, the efficiency was calculated to be 1.2 dB for 16^{th} order for a guiding layer with an index of 1.501. These two sets of results do not concur. Smith and McGreer also found, as a matter of interest here, that the retro-reflecting facets were 11 dB more efficient than a blazed grating with no metallization. (in fifteenth order with guiding layer index 1.45).

6.7.4 REFLECTED PULSE SHAPE – TIME DOMAIN

The reflected pulse at the far-field observation point was elongated compared to the incident pulse. The elongation is due to the shape of the retro-reflecting facet. At the 90° turning facets, the pulse strikes the facets at different times along the wavefront. This is illustrated in Figure 6.13. As a result of the depth of the retro-reflecting facets, the section of the wavefront that strikes the center of the facet travels further than the sections of the wavefront that strike the outer edges. The resultant effect on the pulse is a broadening (in time) of the reflected pulse with respect to the incident pulse. For shorter incident pulses the difference in pulse widths is more obvious though it appears for all pulse durations. Figure 6.3 shows the incident pulse and the reflected pulses, in the time domain, are shown in Figures 6.14 through 6.16. Figure 6.14 depicts the electric field at the far-field observation point as a function of FDTD time steps for the $\beta = 50$ pulse. The full-width half maximum (FWHM) of the incident pulse is 81 time steps while the reflected pulse has a FWHM of 317 time steps. The difference in the two widths is 236

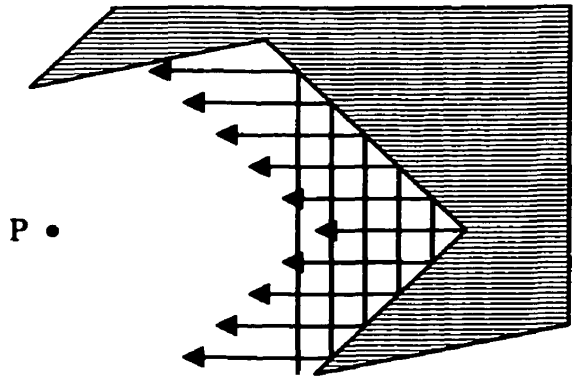

Figure 6.13 The parallel wavefronts (thick lines) strike the retro-reflecting facets at different times. The reflected wavefronts reach the observation point P at different times, resulting in a time-domain elongated pulse.

time steps. The center of the pulse travels an extra distance equal to twice the depth of the retro-reflecting facet. The depth of the facet is 56 Yee cells which corresponds to a physical distance of 5.6 μm. The center of the pulse therefore travels an extra 11.2 μm compared to the edges of the pulse. The time difference due to the extra propagation length is

$$\delta t = \frac{nd}{c_o} \qquad 6.42$$

where d is the extra propagation distance, n_{core} is the refractive index of the core layer (1.501), and c_o is the speed of light in vacuum. The pulse broadening is expected to be δt = 5.60x10^{-14} s. In the FDTD simulation, the incident pulse is propagated in time steps of 2.24x10^{-16} s therefore the pulse broadening is expected to be 250 FDTD time steps. The theoretical broadening differs by 6% from the measured broadening.

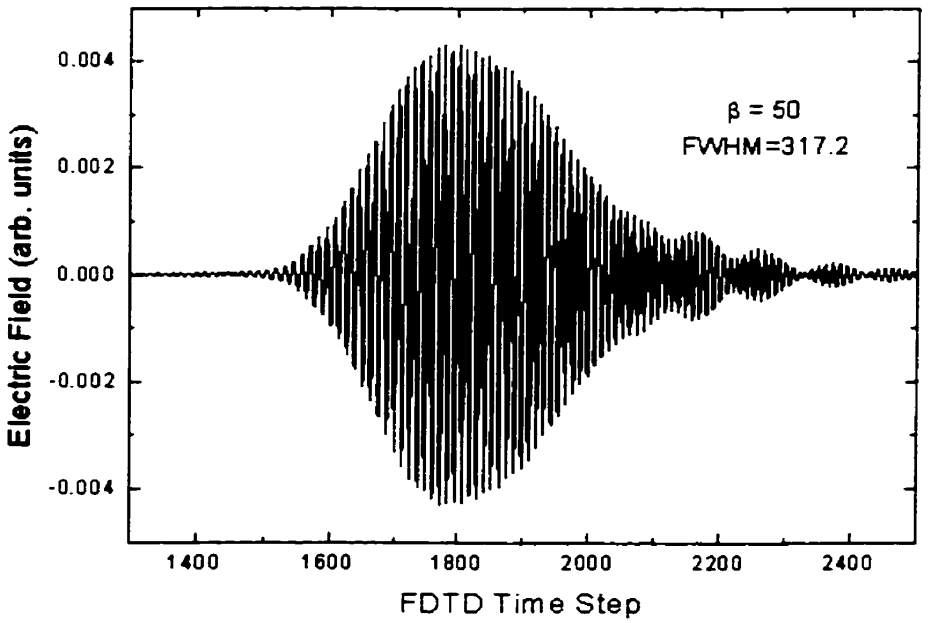

Figure 6.14 The reflected pulse shape for an incident pulse length of β=50. The full width half maximum (FWHM) is 317.2 time steps (δt=2.2x10^{-16}s). The input pulse had FWHM=81.3. The minor pulses in the tail of the reflected pulse are due to diffraction effects from the shaded regions of the grating facet.

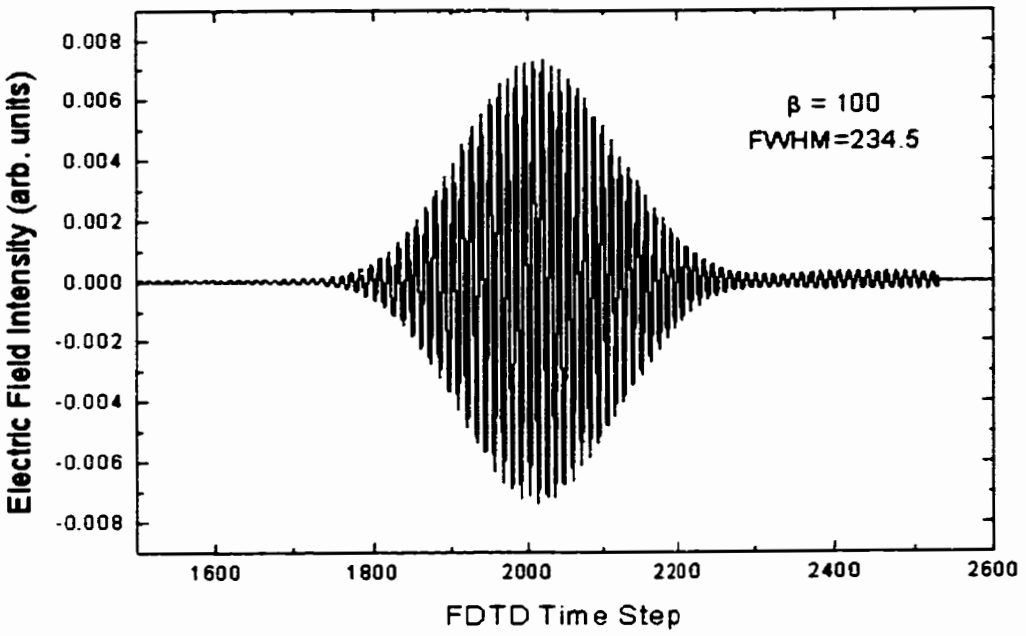

Figure 6.15 The reflected pulse shape for an incident pulse length of β=100. The full width half maximum (FWHM) is 234.5 time steps ($\delta t=2.2x10^{-16}s$). The input pulse had a FWHM=159.9. The minor pulses in the tail of the reflected pulse have been reduced.

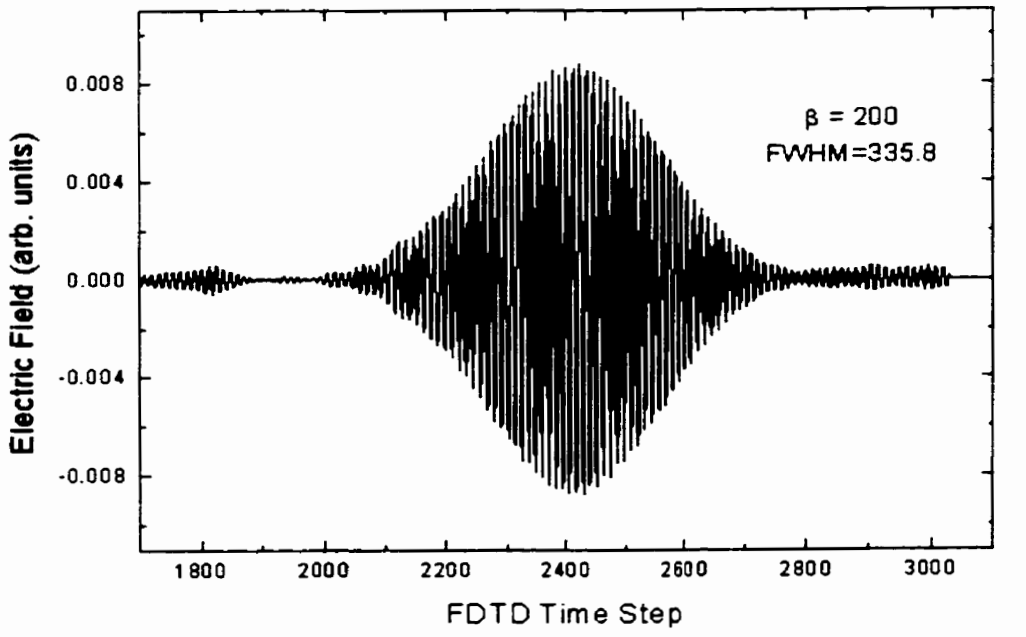

Figure 6.16 The reflected pulse shape for an incident pulse length of β=200. The full width half maximum (FWHM) is 335.8 time steps ($\delta t=2.2x10^{-16}s$). The input pulse had a FWHM=319.8. The minor pulses in the tail of the reflected pulse remain small.

For longer pulses, the broadening effect becomes smaller. For a pulse with β = 100, the difference in the FWHM between reflected and incident pulses is 74 time steps while for a β = 200 pulse, the broadening is further reduced to 16 time steps. This result is expected as it is analogous to the dependence of diffraction effects on the wavelength of the incident light. For diffraction effects to be distinguishable, the object or feature creating the diffraction effect (as in the width of a slit) must be on the order of the wavelength of the light. Analogously, as the duration of the pulse lengthens, the spatial extent of the pulse increases and becomes larger than the depth of the retro-reflecting facet. Once the pulse is significantly larger than the depth of the facet, the elongation effect is reduced, just as diffraction effects become blurred.

6.8 PULSE PROPAGATION MOVIE

One of the most significant tools for debugging the code and understanding the nature of the diffraction gratings was the MATLAB movie that was created using plots of the electric field as a function of time in the computational domain. In these movies instabilities due to errors in the code and losses at sharp corners could be seen as well as a beautiful demonstration the wave nature of the electromagnetic pulse. While this movie is impossible to include in the paper version of this work, several frames of the movie are shown here to give a feeling for the pulse propagation movie.

The MATLAB plots are colour contours representing the intensity of the electric field within the computational domain. The red areas in the plot are the regions of

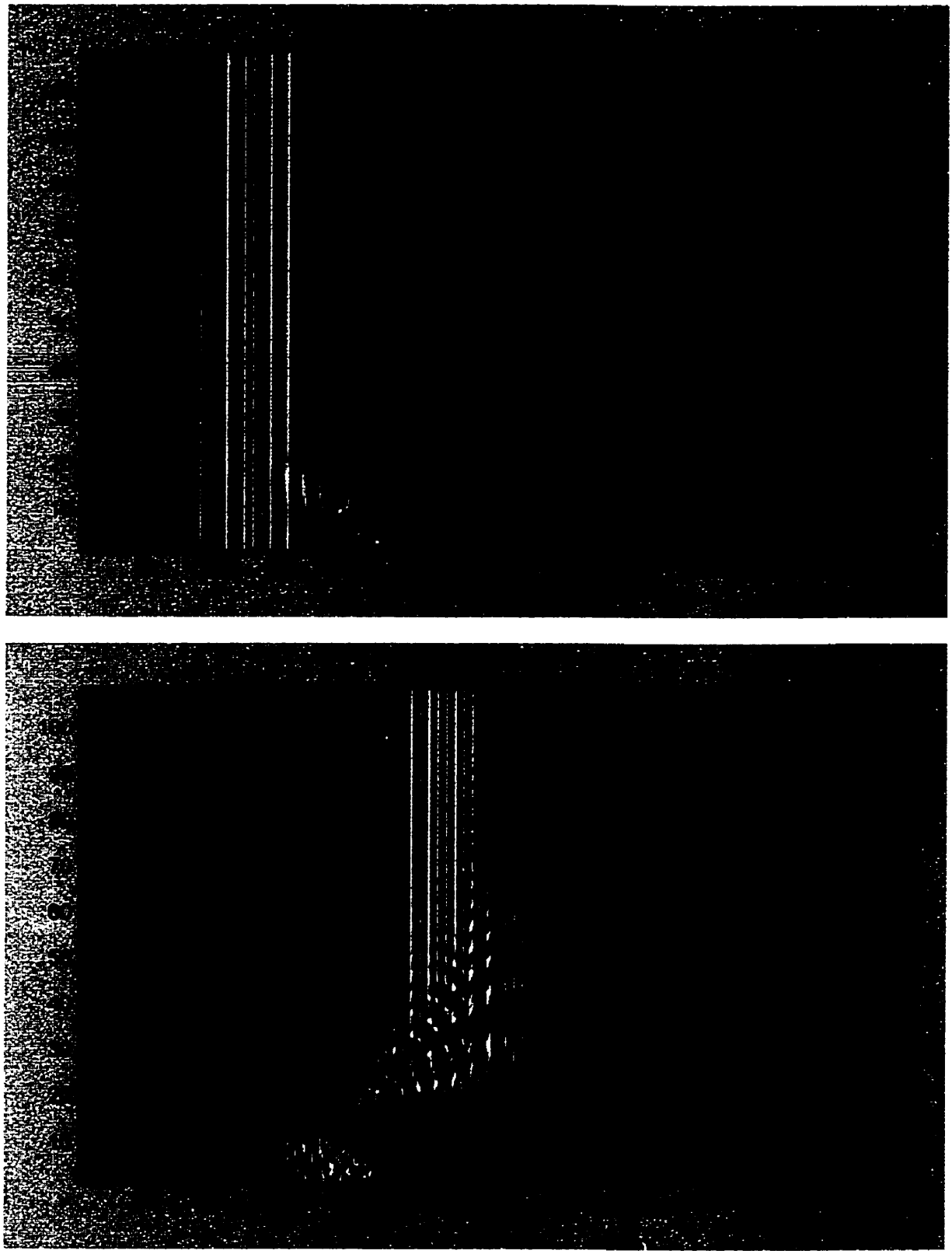

Figure 6.17 These sequential plots show the time-domain propagation of the user-defined incident pulse reflecting at the grating facet.

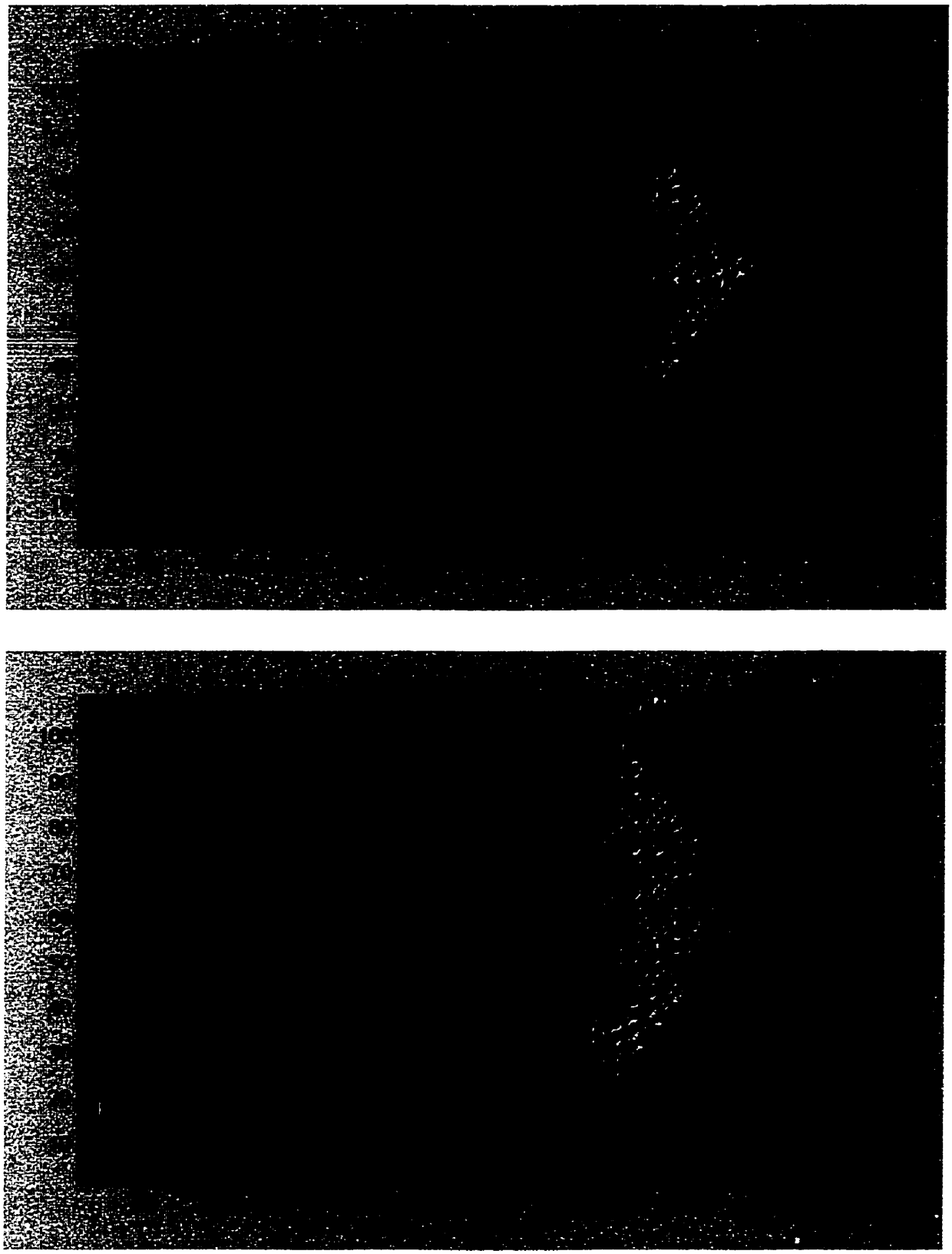

Figure 6.17 continued

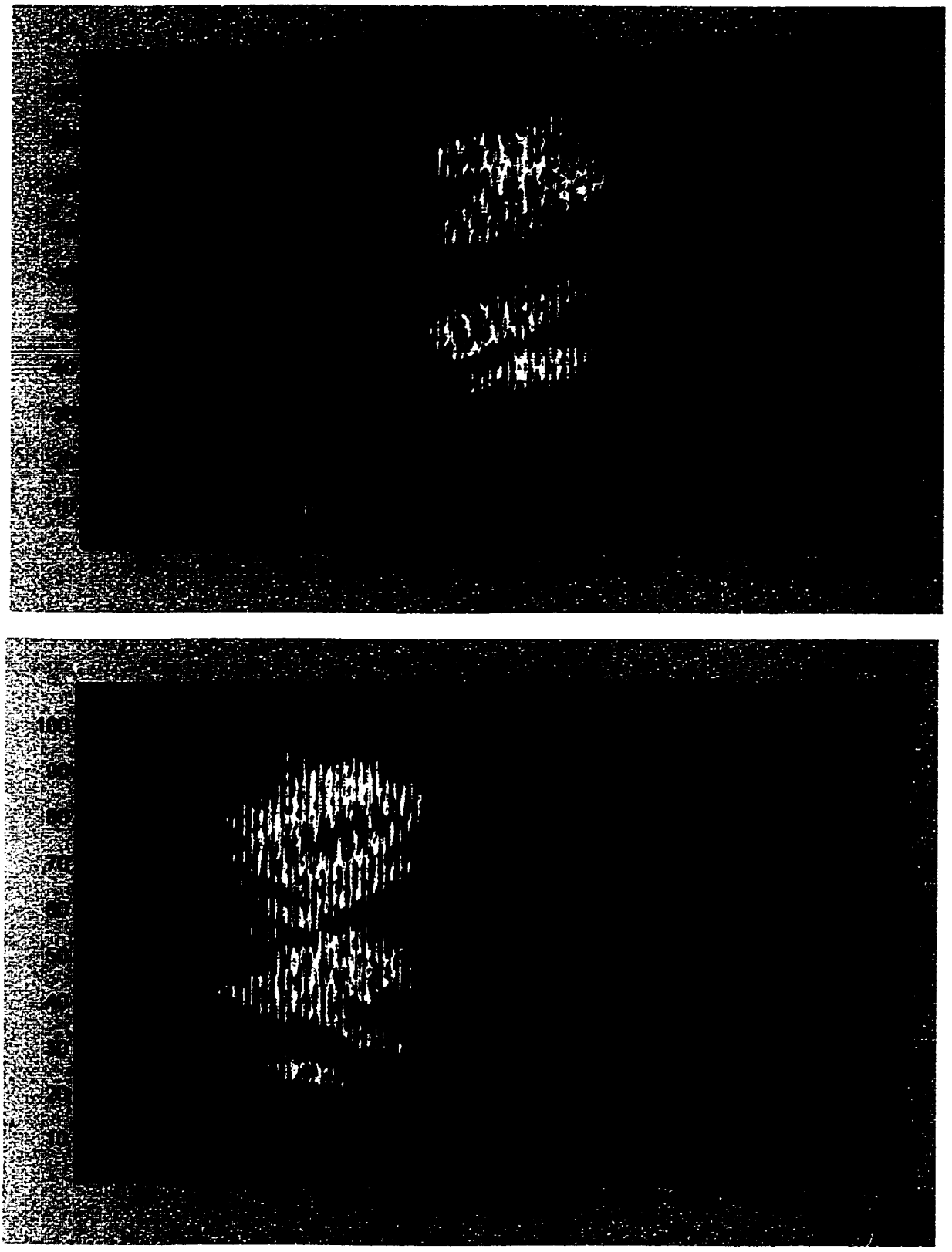

Figure 6.17 continued

highest intensity while the dark blue regions have the smallest electric field intensity. The frames shown in Figure 6.17 show the electromagnetic pulse used in this work propagating through the computational domain and reflecting at the air-waveguide interface that is the grating facet.

6.9 CONCLUSIONS

The results presented in this chapter show that FDTD modeling of the retro-reflecting facets alone can give some insight into the performance of the spectrometer without having to model the entire grating (which is computationally intensive). It has been shown that FDTD is appropriate to this application and is recommended for any waveguide application where reflections are incurred. The modeling results showed that some diffraction effects are expected due to the shape of the grating facet. It is likely that the diffraction from the size of the grating facet will degrade the performance of the spectrometer (by increasing the cross-talk in adjacent channels). The magnitude of the diffraction from the complicated grating facet structure was shown to be of the order expected using diffraction theory derived for a slit aperture.

CHAPTER SEVEN

CONCLUSIONS

7.1 SUMMARY

In this work there were three main objectives: to design, characterize and numerically model an integrated diffraction grating spectrometer. Similar spectrometers have been described previously in the literature and this design was intended to improve on the performance of these retro-reflecting designs. The spectrometer design in this work was also intended to satisfy restrictions placed on dense wavelength division multiplexing (DWDM) demultiplexers used in telecommunications systems. This includes channel spacing that conforms to telecommunications standards, low insertion loss, low polarization dependence, low polarization dependent dispersion and physical robustness.

The channel spacing was designed to be 0.4 nm (50 GHz) and 0.8 nm (100 GHz) which are the current standards for telecommunications DWDM. To achieve low insertion loss, all integrated reflection components were designed to use total internal reflection for efficient reflection without the need for metallization of reflection components. Physical robustness was achieved by the use of integrated optics technology. The integrated structure ensured that the optical alignment of the system was precise and remained constant for the duration of the testing and beyond.

Characterization of the spectrometer designs was carried out to determine the performance of the physical realizations of the designs. The spectrometers were tested to determine the insertion loss, polarization dependent performance and the wavelength dependent performance.

Numerical modeling of the spectrometer was performed at low level due to the complexity of the total design. Finite-difference time-domain (FDTD) modeling was done using Maxwell's equations to represent an electromagnetic pulse propagating through a waveguide layer. Yee's algorithm was used to adapt the differential form of Maxwell's equations into FDTD code. The EM pulse was reflected by a structure that identically matched the structure of a single grating facet. The facet interface was simulated by a refractive index map that defined the air-waveguide interface of the grating facet.

7.2 RESULTS

7.2.1 SPECTROMETER PERFORMANCE

The integrated grating spectrometers showed reasonably good performance. It was demonstrated that the channel wavelength spacing was uniform across the wavelength window of 1530 nm to 1570 nm. The channel spacing was found to be as designed at 0.4 nm and 0.8 nm. The insertion loss was found to be high compared to telecommunications standards though much of this insertion loss was due to the propagation loss in the slab waveguide. The insertion loss ranged from 30-40 dB where between 14 dB to 21 dB is due to propagation loss in the slab waveguide. Other contributions to the insertion loss are fiber/ridge waveguide mode mismatch, ridge waveguide propagation loss (due to sidewall roughness) and losses incurred at the reflective interfaces. The loss profile was found to be wavelength dependent with higher loss at the ends of the telecommunications window (near 1530 nm and 1570 nm) for both designs. The wavelength dependent absorption of the slab waveguide contributed significantly to this variation while other factors (such as defocusing along the output waveguide array) also contributed to the roughly 10 dB excess loss at the extremes of the wavelength range.

The polarization dependent performance of these spectrometers was slightly higher than that of other spectrometers found in the literature. The polarization dependent loss was 3.2 dB while the polarization dependent dispersion was 0.9 nm.

7.2.2 FDTD FACET MODELING

The FDTD modeling of a single grating facet was a success in that it achieved modeling of the physical system as it exists at the grating facet. The code used to do this modeling used Yee's algorithm to implement Maxwell's equations as finite difference equations and Berenger perfectly matched layer (PML) absorbing boundary conditions in two dimensions. The grating facet was shown to effectively reflect an incident collimated pulse of light at 1550 nm. The modeling concluded that the finite size of the retro-reflecting facet caused diffraction on the order of that predicted by diffraction by a rectangular aperture. The diffraction pattern in the far-field of the system suggested that the grating facet behaved similar to a rectangular aperture of width 6.6 μm. The physical opening of the grating facet to the incident light is designed to be 8.6 μm. The efficiency of the grating facet in retro-reflecting the incident light was found to be 76.2%.

7.3 FUTURE WORK

The recommended future work for this project revolves primarily around improving the fabrication technique and taking the numerical modeling one step further. In the fabrication of the spectrometers no particular effort was made to reduce the birefringence of the waveguide layers. It has been shown in the literature that a special layer structure may be constructed to reduce the waveguide birefringence thereby reducing the polarization dependent loss and dispersion of the spectrometers. An implementation of this technique is advisable. The high propagation loss in the slab waveguide is a problem

that also can be remedied by slightly different fabrication. Waveguide absorption of light near 1530 nm can be reduced by proper annealing of the waveguides before etching. It is advisable that this annealing technique be implemented on any SiON/SiO_2 layers. To decrease insertion loss further, the ridge waveguides should be designed such that the mode overlap between single mode fibers and the input/output waveguides is reduced.

The numerical FDTD modeling of the grating facets may be taken one step further by implementing a technique that allows a periodic structure to be modeled without the need for large repetitious arrays within the computational domain. This technique could likely give an idea of the far-field response of the grating. The modeling could be improved further by investigating the difference between reflection of the TE and TM modes in three dimensions. This may shed more light on the magnitude of the polarization dependent loss and dispersion.

REFERENCES

[1] J. Wilson, J.F.B. Hawkes, Optoelectronics, Prentice Hall, University Press, Cambridge (1989).

[2] Kevin M. Able, "Optical Fiber Designs Evolve", Lightwave, February 1998.

[3] Thomas Fuerst, "Today's Optical Amplifiers Enable Tomorrow's Optical Layer", Lightwave, July 1997.

[4] Bruce Nyman, D. R. Zimmerman, J. R. Costelloe, "Advanced Fiber Amplifier Designs Improve WDM System Performance", Lightwave, March 1997.

[5] Steve Turley, "Passive and Active Components", Lightwave, February 1998.

[6] S. Suzuki, Y. Inoue, Y. Ohmori, "Polarization-insensitive Arrayed Waveguide Grating Multiplexer with SiO_2-on- SiO_2 Structure", Electron. Lett., **30**, 642 (1994).

[7] H. Takahashi, S. Suzuki, I. Nishi, "Wavelength Multiplexer Based on SiO_2-Ta_2O_5 Arrayed-Waveguide Grating", J. Lightwave Technol., **12**, 989 (1994).

[8] Ken A. McGreer, "A Flat-Field Broadband Spectrograph Design", IEEE Photon. Technol. Lett., **7**, 397 (1995).

[9] Heather J. Hnatiuk, K.A. McGreer, J.N. Broughton, "An Integrated Optical Spectrometer for WDM", Applications of Photonic Technology 2, editors G.A. Lampropoulos and R.A. Lessard, Plenum Press (1997).

[10] P.C. Clemens, G. Heise, R. Marz, H. Michel, A. Reichelt, H.W. Schneider, "8-Channel Optical Demultiplexer Realized as SiO_2/Si Flat-Field Spectrograph", IEEE Photon. Technol. Lett., **6**, 1109 (1994).

[11] Ken A. McGreer, "Tunable Planar Concave Grating Demultiplexer", IEEE Photon. Technol.Lett., **8**, 551 (1996).

[12] Z. J. Sun, K.A. McGreer, J.N. Broughton, "Demultiplexer with 120 Channels and 0.29 nm Channel Spacing", IEEE Photon. Technol. Lett., **10**, 90 (1998).

[13] C.Cremer, G. Ebbinghaus, G. Heise, R. Muller-Nawrath, M. Schienle, L. Stoll, "Grating Spectrograph in InGaAsP/InP for Dense Wavelength Division Multiplexing", Appl. Phys. Lett., **59**, 627 (1991).

[14] Karen Liu, F. Tong, S.W. Bond, "Planar Grating Wavelength Demultiplexer", SPIE Multigigabit Fiber Communications, **2024**, 278 (1993).

[15] Z. J. Sun, K.A. McGreer, and J.N. Broughton, "Integrated Concave Grating WDM demultiplexer with 0.144 nm Channel Spacing", Electron. Lett., **33**, 1140 (1997).

[16] Miles Klein, and Thomas Furtak, Optics 2nd edition, John Wiley & Sons, Inc., Toronto, ON (1986).

[17] Richard Syms, and John Cozens, Optical Guided Waves and Devices, London, McGraw-Hill Book Company (1992).

[18] B.E.A. Saleh, and M.C. Teich, Fundamentals of Photonics, John Wiley & Sons, N.Y. (1991).

[19] H. Nishihara et. al, Optical Integrated Circuits, McGraw-Hill Book Company, N.Y. (1989).

[20] Zhijian Sun, "Demultiplexer Based on Integrated Concave Grating", Ph.D. thesis, 1998.

[21] D. Marcuse, "Bending Losses of Asymmetric Slab Waveguides", Bell Syst. Tech. J., **50**, 2551 (1971).

[22] E.A.J. Marcatili, "Bends in Optical Dielectric Guides", Bell Syst. Tech. J., **48**, 2103 (1969).

[23] D. W. D Jackson, as yet unpublished (1998).

[24] J. Aarnio, P. Heimala, M. Del Giudice, and F. Bruno, "Birefringence Control and Dispersion Characteristics of Silicon Oxynitride Optical Waveguides", Electron. Lett., **27**, 2317 (1991).

[25] J.-J. He, B. Lamontagne, A. Delage, and L. Erickson, "Monolithic Integrated Wavelength Demultiplexer Based on a Waveguide Rowland Circle Grating in InGaAsP/InP", J. Lightwave Tech., **16**, 631 (1998).

[26] Henry A. Rowland, "On Concave Gratings for Optical Purposes", Phil. Mag., **16**, 197 (1883).

[27] Kane Yee, "Numerical Solution of Initial Boundary Value Problems Involving Maxwell's Equations in Isotropic Media", IEEE Trans. Antennas Propagat., **14**, 302 (1966).

[28] Allen Taflove, Computational Electrodynamics: The Finite-Difference Time-Domain Method, Norwood, MA, Artech House Inc. (1995).

[29] William H. Press et al. editors, Numerical Recipes in C: 2nd Edition, Cambridge University Press, NY (1995).

[30] Gerrit Mur, "Absorbing Boundary Conditions for the Finite Difference Approximation of the Time-Domain Electromagnetic Field Equations", IEEE Trans. Electromagn. Compat., **23**, 377 (1981).

[31] Jean-Pierre Berenger, "A Perfectly Matched Layer for the Absorption of Electromagnetic Waves", J. Computational Phys., **114**, 200 (1994).

[32] Daniel Katz, Eric Thiele, and Allen Taflove, "Validation and Extension to Three Dimensions of the Berenger PML Absorbing Boundary Condition for FD-TD Meshes", IEEE Microwave and Guided Wave Lett., **4**, 268 (1994).

[33] Allen Taflove, Advances in Computational Electrodynamics: The Finite-Difference Time-Domain Method, Norwood, MA, Artech House Inc. (1998).

[34] W.C. Chew and W.H. Weedon, "A 3D Perfectly Matched Medium from Modified Maxwell's Equations with Stretched Coordinates", IEEE Microwave and Guided Wave Lett., **4**, 599 (1994).

[35] C.M. Rappaport, "Perfectly Matched Absorbing Boundary Conditions Based on Anisotropic Lossy Mapping of Space", IEEE Microwave and Guided Wave Lett. **5**, 90 (1995).

[36] Jean-Pierre Berenger, "Three-dimensional Perfectly Matched Layer for the Absorption of Electromagnetic Waves", J. Computational Phys., **127**, 363 (1996).

[37] Jean-Pierre Berenger, "Improved PML for the FDTD Solution of Wave-structure Interaction Problems", IEEE Trans. Antennas and Propag., **45**, 466 (1997).

[38] S. Gedney, "An Anisotropic Perfectly Matched Layer Absorbing Media for the Truncation of FDTD Lattices", IEEE Trans. Antennas and Propag., **44**, 1630 (1996).

[39] L. He, "FDTD – Advances in sub-sampling methods, UPML, and higher order boundary conditions", M.Sc. thesis, University of Kentucky (1997).

[40] Raymond Luebbers, K. Kunz, M. Schneider, and F. Hunsberger, "A Finite Difference Time-Domain Near Zone to Far Zone Transformation", IEEE Trans. Antennas and Propag., **39**, 429 (1991).

[41] Jean-Pierre Berenger, "Perfectly Matched Layer for the FDTD Solution of Wave-Structure Interaction Problems", IEEE Trans. Antennas and Propag., **44**, 110 (1996).

[42] Jean-Pierre Berenger, "Improved PML for the FDTD Solution of Wave-Structure Interaction Problems", IEEE Trans. Antennas and Propag., **45**, 466 (1997).

[43] Raymond Luebbers, D. Ryan, and J. Beggs, "A Two-Dimensional Time-Domain Near-Zone to Far-Zone Transformation", IEEE Trans. Antennas and Propag., **40**, 848 (1992).

[44] Kane Yee, D. Ingham, and K. Schlager, "Time-Domain Extrapolation to the Far Field Based on FDTD Calculations", IEEE Trans. Antennas and Propag., **39**, 410 (1991).

[45] Karl S. Kunz and Raymond J. Luebbers, The Finite Difference Time Domain Method for Electromagnetics, CRC Press, FL (1993).

[46] M.S.D. Smith, and K.A. McGreer, "Diffraction Gratings Utilizing Total Internal Reflection Facets in Littrow Configuration", IEEE Photon. Technol. Lett., **11**, 84 (1999).

[47] S. Sadov, and K.A. McGreer, "Polarization Dependence of Diffraction Grating Utilizing Total Internal Reflection Facets", submitted to IEEE Photon. Technol. Lett. April 1999.

[48] G.E. Forsythe, M.A. Malcolm and C.B. Moler, Computer Methods for Mathematical Computations, Prentice Hall, 1977.

[49] Eugene Hecht, Optics Second Edition, Addison-Wesley Publishing Co., Mass., 1990.